MICROPLASMA DISCHARGES IN HIGH PRESSURE GASES

SCALING TOWARDS THE SUB-MICRON REGIME

A Thesis

by

ADITYA RAJEEV CHITRE

Submitted to the Office of Graduate Studies of
Texas A&M University
in partial fulfillment of the requirements for the degree of

MASTER OF SCIENCE

December 2010

Subject: Mechanical Engineering

Microplasma Discharges in High Pressure Gases

Scaling Towards the Sub-micron Regime

MICROPLASMA DISCHARGES IN HIGH PRESSURE GASES

SCALING TOWARDS THE SUB-MICRON REGIME

A Thesis

by

ADITYA RAJEEV CHITRE

Submitted to the Office of Graduate Studies of
Texas A&M University
in partial fulfillment of the requirements for the degree of

MASTER OF SCIENCE

Approved by:

Co-Chairs of Committee,	David Staack
	Sy-Bor Wen
Committee Member,	Lewis Ntaimo
Head of Department,	Dennis O'Neal

December 2010

Major Subject: Mechanical Engineering

ABSTRACT

Microplasma Discharges in High Pressure Gases

Scaling Towards the Sub-micron Regime. (December 2010)

Aditya Rajeev Chitre, B.Tech., University of Pune

Co-Chairs of Advisory Committee: Dr. David Staack
                                   Dr. Sy-Bor Wen

Atmospheric pressure microplasmas are uniquely characterized by their very high energy densities and also by their small discharge sizes. These properties allow for unique applications in plasma processing technologies. We have investigated the operational characteristics of microplasmas at higher energy densities and smaller sizes by operating microplasma configurations at high pressure conditions.

We studied the discharge and analyzed its variation with changes in current and pressure. The discharge was analyzed by microscopic visualization and data from the images and was processed to measure the current density and estimate charged particle density. By increasing the pressure beyond 200 psi and by minimizing the discharge current required for sustaining the plasma, we have been able to achieve discharge sizes of 7 μm in nitrogen and as small as 20 μm in helium. Optical emission spectroscopic studies were carried out to measure gas temperature and vibrational temperature using the nitrogen 2nd positive system. With increase in pressure, the transition from non-equilibrium plasma to equilibrium plasma was also studied using the OES temperature measurements.

Temperature measurements are also used to estimate normalized current densities. Normalized current density results obtained after introducing the corrected effective pressure based on the increased gas temperature are close to the value of 400 µA /cm^2*Torr^2 obtained for low pressure normal glow discharges in nitrogen.

This research presents further validation of the general operational characteristics of microplasmas being pressure scaled versions of normal glow discharges. Attained energy densities are ten to twenty times higher than in atmospheric pressure microplasmas. Discharge sizes are also significantly smaller, decreasing with increasing pressure, but the scaling is with density 'nd' rather than pressure 'Pd' due to the increase in gas temperature with pressure, indicating a dependence on collisional processes. We can infer that at higher pressures, the operational characteristics of more complex plasma discharges like dielectric barrier discharges, RF plasmas, etc. follow scaling patterns, transitions and limits similar to the microplasma discharge studied in this thesis.

DEDICATION

To my loving and ever supporting parents, sweet sister and friends for their support and

encouragement

ACKNOWLEDGEMENTS

TABLE OF CONTENTS

Page

LIST OF FIGURES

Page

LIST OF TABLES

1. INTRODUCTION

1.1.   Introduction and motivation

1.1.1. Plasmas

Plasmas are partially ionized gases consisting of free electrons, ions and neutral gas species. These electrons and ions are free to move and hence respond to the presence of an external electric or magnetic field. The presence of these electrons gives the plasma its unique properties as compared to the other three states of matter [1].

The plasma may be thermal or non-thermal in its nature. A thermal plasma is one in which the ions, neutral gas species and the electrons are all at the same temperature. Typical temperatures are in the range of 6000 K to 10000 K. The thermal plasma is hence in a state of equilibrium.

Non-thermal plasmas on the other hand are non-equilibrium plasmas. The gas temperature and electron temperature in non-thermal plasmas are different from each other [1, 2]. In these "cold plasmas", the ions and neutral species are at much lower temperatures than the electrons [1]. Typical gas temperatures range from 300 K up to 2000 K while electron temperatures span from approximately 11000 K to 22000 K [2].

This thesis follows the style of *Plasma Sources Science & Technology.*

1.1.2. Plasma processing

Plasma processing can be defined as the modification in the chemical or physical properties of a material in the presence of plasma. The modifications can be achieved due to the presence of active species like ions, electrons and radicals in the plasma. The active species are able to provide the energy required to modify the involved chemical processes or facilitate physical material removal or deposition [3].

Plasma enhanced chemical vapor deposition, plasma etching, surface cleaning and modification, plasma polymerization etc. are among the numerous applications that are included under plasma processing [1].

Different types of plasmas have been investigated at varying conditions of pressure [4]. Glow discharge plasmas are used for microelectronics fabrication in silicon at low pressures [3, 4]. On the other hand, atmospheric pressure radio frequency plasma jets are used in thin film deposition applications [5].

Many atmospheric pressure plasma processing technologies are also being commercially used in the industry. Non-thermal dielectric barrier discharges are being used in ozone generation, pollution control and surface treatment. Thermal plasmas like electric arcs and plasma torches are used in metal spraying, hazardous waste destruction and electrical discharge machining [4].

1.1.3. Direct write plasma processing

Direct write techniques based on lasers, thermal sprays and ion beam implanting have been used in material deposition, microelectronics and manufacturing electronic sensors [6, 7, 8, 9]. In contrast to lithography techniques which use a mask and are suited for large scale large area processing, direct write techniques are more suitable for patterning more intricate, complex features on smaller processing areas.

Direct write plasma processing refers to the use of a plasma source to modify the physical or chemical properties of a material by directly controlling the plasma discharge from a pre-programmed computer. One application of such a direct write process would be the removal of material from the target surface to generate a pattern of features on the surface of the material. The target surface itself could serve as one of the electrodes in the system. This is termed as direct write surface patterning [10].

Micron sized or sub-micron features developed by such a direct write surface patterning technique can find application in the manufacturing industry, the semiconductor industry and even in medical fields. The key element here would be to scale down the plasma discharge size to generate as small a feature size as possible without damaging the material surface [5, 11]. The size of the features would be limited by the size of the plasma. The size of the plasma is governed by collisions subject to scaling laws such as 'Pd' scaling [12, 13] discussed in section 2.3.2.

1.2.   Thesis statement

Atmospheric pressure microplasmas are uniquely characterized by their very high energy densities and also by their small discharge sizes [3]. This thesis will aim to investigate the operational characteristics and the temperature of the microplasmas by operating the microplasma discharge configuration at high pressure conditions.

The thesis will aim to achieve small microplasma discharge sizes (< 10 μm) in an industrially workable gas with high energy densities making the discharge suitable for plasma processing applications [1, 3, 4].

More fundamentally, the discharge size scaling laws will be simultaneously investigated at high pressure conditions. These physical scaling relationships are also important to all high pressure discharges. We can infer that at high pressures, the operational characteristics of more complex discharges like dielectric barrier discharge, RF plasmas etc. would demonstrate scaling relationships, limits and transitions similar to the microplasma or normal glow discharge analyzed in this thesis.

Applications of this study of non-thermal microplasmas are related to potential functions in the semiconductor manufacturing industry as well as diverse uses in other areas of research [4].

1.3.   Research objectives

a) The thesis will focus on the parameters of microplasma discharge size and the energy density or particle density of the plasma. These features are important from the perspective of using the microplasma for plasma processing and direct write surface patterning applications. The variation of these parameters with pressure will be studied in depth with the goal of achieving minimum discharge sizes and maximum energy densities.

b) The thesis will also include optical emission spectroscopy as its plasma temperature diagnostic tool. The rotational and vibrational temperatures of the microplasma discharge will be estimated using a customized temperature model compared with experimentally acquired spectra from the microplasma system.

c) Through these temperature measurements, the thesis will attempt to study the mode transition of the microplasma from a non-equilibrium operation regime to an equilibrium operation regime. The temperature measurement results should provide more clarity with regards to the scaling laws at higher than atmospheric pressures and seek to investigate the limits of the scaling.

1.4. Thesis document overview

Section 1 introduces the field of plasma processing and outlines the thesis statement and the research objectives.

Section 2 describes the microplasma discharge and its suitability for the study. The applications of the microplasma discharge along with a brief review of the microplasma discharge sizes achieved by other researchers are presented in this section.

Section 3 explains the diagnostic techniques and procedures used to make measurements for the microplasma discharge size and the modified SPECAIR model for estimating the temperatures from the experimentally acquired spectra.

Section 4 focuses on the design of the experiment and the pressure chamber. It also explains the initial experiments and the inferences drawn from them.

Section 5 focuses on the final experiments carried out to study the parameters of interest. The results of the study are analyzed in this section.

Section 6 summarizes the results along with presenting the final conclusions of the study.

2. BACKGROUND AND LITERATURE MATERIAL

2.1. Normal glow discharge at atmospheric pressure

A normal glow discharge [14] at atmospheric pressure in its basic form consists of two electrodes separated from each other by a gap across which a high potential difference is applied [1].

2.1.1. Electrode configuration and electrical excitation

The electrodes may be exposed to air or enclosed in a gas filled chamber. Gases like air, nitrogen, argon, helium etc. may be used. The spacing in between the two electrodes determines the voltage required to initiate the electrical breakdown of the medium between them. The applied voltage and the electrode spacing determine the electric field in units of V /cm required to breakdown the gas depending on its ionization potential [1].

2.1.2. Mechanism of operation

When electrical excitation is applied across the electrodes, a small percentage of the gas atoms are initially ionized by random collision processes. Positively charged ions move towards the cathode while the negatively charge electrons rush towards the anode. During this travel, electrons gain energy and collide with atoms and further ionization takes place. These excited species can decay to lower energy levels by the emission of light. Secondly, the ions accelerating towards the cathode cause secondary electrons to be released from the cathode. These secondary electrons provide further ionization collisions. The cathode atoms also get excited due to collisions with the other particles in

the discharge gap after being drawn into the gap due to drift motion. However they quickly return back to their ground states by radiating energy in the form of photons or light. Thus in the presence of a strong enough electric field, secondary electron emission from the cathode and ionization of the gas can produce a self-sustaining plasma discharge [14].

2.1.3. Discharge structure

Figure 1 shows the anode glow, positive column, the Faraday dark space and the negative glow which are the primary regions in the glow discharge structure [1, 14].
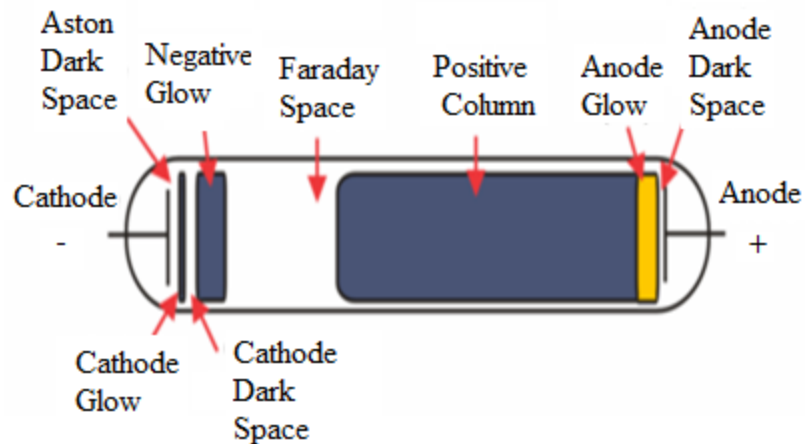
Figure 1. Glow discharge structure and regions

The bright region near the anode representing the boundary of the anode sheath is called the anode glow.

The positive column extends from the anode towards the cathode. The electric field in the positive column is large enough to maintain a constant degree of ionization enough to reach the anode.

The negative cathode glow is the brightest region of the discharge space having the highest charged particle density. All the current in this region is supplied by the electron current due to the high mobility of the electrons. Most of the ionizing and collision processes occur in the negative glow region contributing to the analytical information this area can provide.

The dark region in the plasma between the positive column and the negative glow with extremely low luminosity is called the dark space. This dark space is observed as the electric field in this region is extremely low and hence a negligible number of collisions take place in resulting in an extremely negligible population of excited species and consequent light emission.

At the end of the negative cathode glow region, the electrons lose their energy and hence the ionizing and collision processes cease resulting in the dark space region of the glow discharge [14]. In short, the boundary conditions at the negative glow are drastically different than the positive column resulting in a large degree of variation in the energy levels as well as particle density in the two regions. The transition between the two zones is facilitated by the low electric field in the dark space between them.

The Aston dark space, the cathode glow, cathode dark space and the anode dark space are dark or luminous regions seen in low pressure discharges typically in the range of 0.1 to 10 Torr.

2.1.4. Operation regime

Figure 2 shows the regimes of operation for a DC plasma discharge [14].
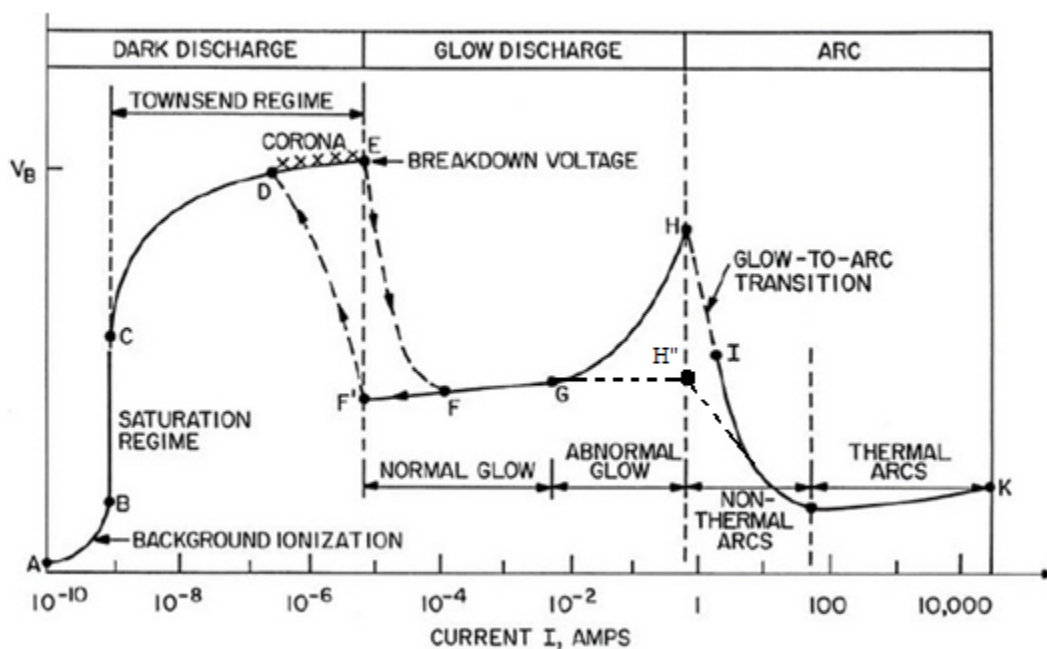
Figure 2. Electrical discharge regimes

In the background ionization stage A-B, ions and electrons migrate to the electrodes producing weak electric currents. In the B-C saturation region, the current saturates with increase in voltage. Beyond point C the current rises exponentially with increase in voltage. The electric field becomes high enough for gas ionization and secondary electron emission leading to avalanche of electron and ion production. This region of

exponential current increase is called the Townsend discharge. In the D-E region, corona discharge which is a sort of glow discharge at the end of sharp wires and tips occurs. Beyond point E, electrical breakdown occurs, current increases by factor of 10^4 to 10^8 and is limited only by the internal resistance in the power supply circuit. A lower voltage is then required to sustain the discharge after breakdown.

In the normal glow discharge regime F-G, the voltage remains almost constant with respect to the increasing current over several orders of magnitude. The current density is independent of the total current [1, 14]. The current density remains constant with the discharge growing larger in size with increase in current [15].

A sudden increase in voltage in region G-H would correspond to a transition to abnormal mode or an arc discharge [1, 14]. This only occurs if the plasma is geometrically limited in terms of cathode space. This transition can be avoided by keeping the discharge gap small and not spatially confining the plasma [15]. This would result in the discharge size continuing to increase in a normal glow mode with further increase in current shown in region G-H" resulting in the increasing cathode area being occupied by the discharge glow but never being geometrically limited.

Both G-H and G-H" regions will be followed by a glow to arc transition with further increase in current accompanied by a drop in the discharge voltage.

2.1.5. Suitability for our study

The normal glow discharge is a non-thermal plasma with gas temperature T_{gas} lower than the electronic temperature T_e [1, 14, 15]. The normal glow discharge is also a high energy density plasma [14]. These properties make it suitable for plasma processing applications related to both physical and chemical properties [4]. The normal glow discharge regime with its lower power requirement of a few watts [15] is hence suitable for generating the microplasma discharge that is used in the experiments in this thesis. The microplasma is essentially a normal glow discharge of small dimensions ranging from micrometers to a few millimeters [1, 15, 16].

The microplasma is thus chosen as the discharge to be used to study the properties as outlined in the thesis objectives in section 1.

2.2.   Microplasmas

2.2.1. Definition

Microplasmas are small scale glow discharges in gases. These discharges are characterized by sizes ranging from micrometers to a few millimeters [1, 15, 16]. These discharges can be maintained stable with low power consumption at higher than atmospheric pressures [2, 3]. They can be operated by both DC as well as AC supply [3, 4, 5]. DC microplasma discharges are studied in this thesis. However the RF based microplasma discharge is also being widely studied [5, 17]. The small sizes of the

microplasmas make them suitable for a variety of ultrafine processing technologies [5, 17, 18, 19, 20].

2.2.2. Microplasma applications

Microplasmas are generated in conditions favorable for the production of transient molecular species and chemically reactive species which can lead to novel applications in plasma processing technologies [3]. Advantages such as low power consumption, high power density, high electron densities and the non-thermal nature of the plasma make it suitable for a variety of applications [15].

Microplasmas are used in applications like surface cleaning, etching, surface modification, printing and deposition [21, 22, 23, 24, 25, 26]. The small size of the microplasma makes it suitable for use as an on-chip chemical analysis tool or even a miniaturized total analytical system [27, 28, 29]. Microplasmas are also being investigated for being used as micro reactors for gas phase chemistry and in micro fluidic devices for functional group detection [30]. They are being used for ozone generation as well as for generation of Si nano particles [31]. Arrays of microplasmas are being investigated for applications in inactivating microorganisms [32, 33] as well as for pollution control [34]. The microplasma discharge also presents an avenue for studying the possible breakdown of 'Pd' scaling discussed in section 2.3.2 with increase in pressure [2, 3, 13, 15].

2.2.3. Reviewed literature material

Microplasmas have immense potential in plasma processing technologies with a variety of applications as mentioned above. With the discharge size of the microplasma being a critical factor, research on the microplasma is important for establishing small scale processing [5]. Research has previously been carried out with respect to restricting the microplasma discharge size to dimensions lower than a few hundred microns [35]. Most of this research has been motivated by practical applications like plasma display panels, UV light sources and local etching or deposition.

Microplasma arrays operating at below atmospheric pressure in an abnormal glow mode have been fabricated by Eden and co-workers [36]. These systems powered by either AC or DC sources have been tested with applications for plasma lighting sources. Further research has resulted in large microplasma arrays being fabricated and tested in silicon with dimensions of 50 x 50 μm^2 with complex inverted pyramid geometries [37]. Smaller dimensions of 10 x 10 μm^2 have also been reported [37].

Stabilization and control of direct current glow discharges with characteristic dimensions of 100 μm have been investigated by Schoenbach and co-workers [38, 39, 40]. Cathode boundary layer microplasma discharges less than 100 μm in size have been studied for their use as intense excimers [41].

Patterned micro discharge arrays have been fabricated in flexible copper-polyamide structures by Sankaran [21, 22, 23]. These etched microcavity arrays have characteristic

dimensions of 200 μm. A stencil mask was used for patterning the array and the discharge was struck in a CF_4 and argon mixture [21].

Tan and co-workers are investigating micro machining in silicon using a microplasma jet. They have successfully developed a 3 dimensional machining system to produce features in silicon. Features of up to 50 to 100 μm in size can be machined [41].

Microplasma modeling research has been performed by Kushner [13]. His works state that microplasmas are scaled models of macroscopic discharges and share several of their properties. 'Pd' scaling is one of the properties. His works mentions the possible breakdown of the 'Pd' scaling law as we approach sub-micron regimes.

2.3.   Current density and scaling laws

2.3.1.   Current density for normal glow discharge

Equation 1 gives the current density defined as electric current per unit cross sectional area [1]. Equation 2 gives the current density in terms of electron number density.

$$\text{Current density } j = \frac{\text{Current}}{\text{Area}}$$

(1)

Equation 1. Current density

$$j = n \, e \, V_{drift}$$

(2)

Equation 2. Current density in terms of number density

where, j = Current density (A/m^2)

n = electron density (#/m^3)

e = electron charge (C)

V_{drift} = drift velocity of the electron (m/s)

Electron density and current density are important parameters for the plasma [1, 15]. The plasma is inherently an ionized gas with free a high density of free charge carriers which makes the plasma electrically conductive [1]. The electron density or the current density values indicate how electrically conductive a plasma is and conversely how efficiently it would suit a particular plasma processing application through the creation of active species [3, 4]. High energy density plasmas like microplasmas have been demonstrated to have significant applications in plasma processing technologies with higher processing rates as mentioned in sections 2.2.2 and 2.2.3.

Current density is often normalized with respect to the operating pressure conditions to obtain a normalized current density j/P^2 in units of μA /cm^2*Torr^2 [1]. This normalization enables us to compare the density of plasmas operated at varying pressure conditions most notably below atmospheric pressure of 1 bar or 760 Torr.

Normalized current densities for various electrode materials in a variety of gases have been calculated and are available in literature. The reference value of 400 μA /cm^2*Torr^2 for stainless steel in nitrogen is of particular importance to us with regards to the work in this thesis [1].

Electron density calculations require an assumption to be made for the electron thermal drift velocity V_{drift}. The thermal drift velocity calculation can be made by assuming that the plasma is quasi neutral throughout the region between the electrodes and hence the electron and ion densities are equal to each other and hence using the ion temperature for the calculation to get V_{drift} = 300 m/s [1]. If we consider the sheath region close to the electrodes where the ion density is greater than the electron density and the ion velocity is dependent on the electron temperature [1], the drift velocity value changes to 1800 m/s. Electron density calculations in this thesis are done with the electron thermal drift velocity V_{drift} = 300 m/s. Using V_{drift} = 1800 m/s will yield lower estimates for the electron density.

2.3.2. Scaling laws

The breakdown characteristics of a glow discharge are described by the Paschen curve. The Paschen law states that the breakdown voltage is a function of the product 'Pd', where P is the operating pressure and d is the distance between the two electrodes [1].

The 'Pd' scaling law states that the characteristic length of the plasma must go on decreasing with increase in pressure or medium density [1, 13, 15].

The plasma parameter 'Pd' can be represented as a dimensionless constant multiplied by the Knudsen number. The derivation is summarized below:

$$K_n = \lambda / d \qquad P = n\,K\,T \qquad n = 1 / (\sigma\,\lambda)$$

$$P\,d = n\,K\,T\,d \qquad P\,d = (K\,T / \sigma)\,(d / \lambda) \qquad P\,d = constant \times K_n$$

where, K_n = Knudsen number λ = molecular mean free path

   d = physical discharge gap length   P = Pressure

   n = electron density   K = Boltzmann's constant

   T = Temperature σ = cross sectional area

The 'Pd' parameter thus can be related to the Knudsen number which is a dimensionless number representing the ratio of molecular mean free path to the physical length scale [2, 3].

The 'Pd' scaling law can thus be expressed as a constant as follows:

$$P_{ref}\,d_{ref} = C_1$$

With P = n K T, we can express the scaling law based upon the collisional mean free path using reference ($_{ref}$) and experimental ($_{exp}$) subscripts:

$$n_{ref}\,d_{ref} = n_{exp}\,d_{exp} = C_1 / K\,T_{ref}$$

This scaling is referred to as nd scaling.

Expressing the experimental electron density n_{exp} in terms of pressure, cancelling K and re-arranging we get,

$$(P_{exp}\,T_{ref}/T_{exp})\,d_{exp} = C_1$$

The bracketed term is called the effective pressure term.

$$P_{eff} = P_{exp}\,T_{ref}/T_{exp}$$

The effective pressure is taken into consideration when the experimental temperature is different than the reference temperature due to heating of the gas.

With a decrease in the characteristic length of the plasma, the current density of the plasma goes on increasing with increase in medium density. This is due to the decrease in the cross sectional area while the current remains unchanged [15]. With increase in pressure, discharge size scaling occurs but the discharge power remains constant. However due to the reduction in the characteristic length, the area through which cooling occurs scales by $1/P^2$ [2, 13].

The 'j/P^2' scaling law states that the normalized current density must remain constant for a particular gas and electrode material combination [1, 13, 15].

Another important parameter is the electric field scaling given as the ratio of electric field and number density.

As per the electric field scaling law, the E/n ratio remains constant with increase in pressure.

With this background, the diagnostic techniques used for measuring the microplasma discharge size and the temperature by OES are discussed in the next section. The pressure chamber design, the microplasma generation and the allied instrumentation are discussed in detail in section 4. Section 3 discusses the diagnostics considering the system is in place.

3. DIAGNOSTIC TECHNIQUES

3.1. Microscopic visualization discharge size measurement

Microscopic visualization was used to capture the plasma discharge inside the chamber. Figure 3 shows an image of the microplasma discharge in the pressure chamber captured using a Micrometrics camera module [42] mounted on a MEC-2 microscope [43]. The microscope is at its full 4.5X magnification providing a resolution of 1.4 μm / pixel focusing on 2.2 mm × 1.8 mm area.

3.1.1. Capturing the microplasma discharge

The Micrometrics SE premium software provided a live visual of the microplasma discharge area after the microscope was suitably focused on the discharge area. The camera software was also able to capture images at varied settings of exposure time with additional features like averaging and digital gain control.
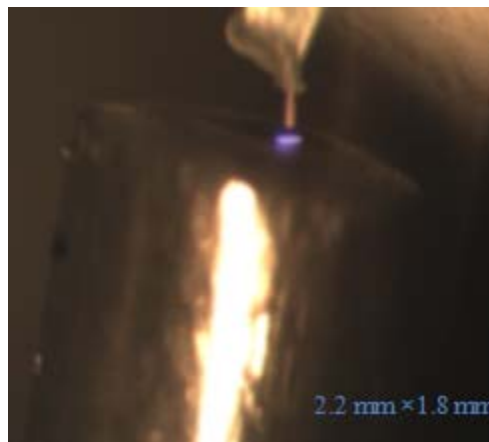
Figure 3. Microplasma discharge imaging

3.2. Discharge size measurement

A software package called 'Image J' [44] was used to determine the discharge size of the microplasma from the captured images. Using the known diameter of the $1/16^{th}$ inch stainless steel electrode, the µm /pixel resolution was calculated. The $1/16^{th}$ inch stainless steel electrode corresponded to a length of 1587 µm and constituted 1135 pixels on screen. This gave a resolution of 1.4 µm /pixel at the maximum 4.5X magnification to all images when viewed on the computer screen via the Micrometrics camera without the introduction of any digital zoom.

The Image J software came with an inbuilt calibration tool in which the length /pixel could be set. As all the images of the microplasma were taken under conditions of the maximum 4.5X magnification of the microscope, the resolution of 1.4 µm /pixel was maintained constant for all the captured images. The length measurement tool in the software could then be used to measure the size of the cathode glow by dragging along the appropriate area in the image. The size of the cathode glow represents the size of the microplasma discharge [15]. The Image J software displays the discharge size in units of µm depending on the µm /pixel resolution preset in the calibration tool.

Discharge size measurements were thus initially performed manually in Image J. However the process was tedious and subject to human error in exactly defining the size of the cathode glow which represented the size of the microplasma discharge.

3.2.1.   Discharge size measurement using MATLAB

To streamline the discharge size measurement process and eliminate measurement inconsistencies, a MATLAB code was designed to analyze the images and extract discharge size data from them.

3.2.1.1.   'Analyze image size' code algorithm

The Analyze image size code can be found in Appendix A.

1. All the images were captured at maximum zoom on the microscope and stored in a one directory and named according to a set format. The light source used initially for illuminating the electrodes was switched off so that only light from the microplasma discharge is captured. Figure 4 shows a captured image after zooming in on the area of interest.
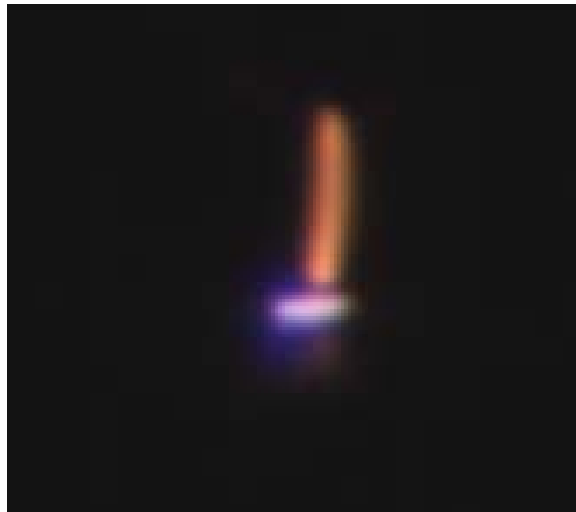
Figure 4. Microplasma discharge as captured by microscopic visualization

2. The image files in the directory were opened in MATLAB in an image format.

3. An area of interest was selected such that the microplasma lies within the selected region in all the images that are being analyzed in the current directory. This feature in the code significantly reduced the processing time for the program.

4. The image was then plotted with the region of interest divided into areas of varying light intensity.

5. The region of interest was expressed as a matrix array with each element representing a pixel in the interest area.

6. The matrix was normalized with respect to the captured light intensity at every pixel location by comparing it with the maximum captured light intensity in the interest area.

7. The pixels in the region of the cathode glow that defines the discharge size were at a higher intensity level than the other parts of the microplasma image. A threshold value set at 70% of the maximum intensity was defined to find out the indices corresponding to the cathode glow which were above the specified threshold.

8. The minimum and maximum indices of the pixels in the x direction that are above the intensity threshold were determined. The difference between the pixel indices gave the discharge size of the microplasma represented by the size of the cathode glow.

9. The discharge size in pixels was multiplied by the preset imaging resolution of 1.4 μm /pixel to attain the microplasma discharge size in microns. Figure 5 shows a false color image with the measured indices. The difference between the first and last red index of the cathode glow gives discharge size with the conversion 39 pixels = 55 μm.

39 pixels = 55 μm
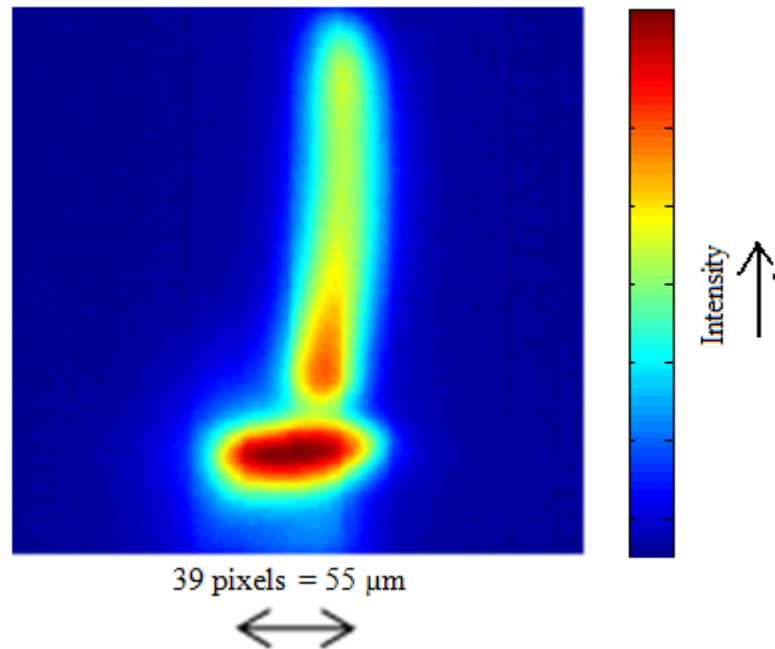
Figure 5. Discharge size measurements using false color image

10. The discharge area was calculated by approximating it to be a circle of diameter equal to the discharge size. Current density calculations were made by dividing the discharge current with the discharge area to get the current density 'j' in units of A /cm^2 or μA /cm^2.

3.3. Temperature measurement

This section explains the principle of optical emission spectroscopy and the OES instrumentation components used to get the experimental spectra and then the comparison model developed to get the temperatures associated with the rotational and vibrational levels [45] of the nitrogen molecule.

3.3.1. Optical emission spectroscopy (OES)

When any element or compound is excited either electrically or thermally, it emits light or electromagnetic radiation depending on its constituent atoms and molecules. This emission is the result of the transition of the atoms or molecules from a higher excited energy state to a lower energy state. Depending on the energy difference between the two energy states, the photons emitted have a certain characteristic energy or wavelength [46]. Equation 3 gives the energy of the photon.

$$E = h\ (v\text{-}v_0)\ m = h\ c\ /\lambda$$

(3)

Equation 3. Energy of a photon

Spectroscopy is a diagnostic technique based on the principle of dispersion of light as it travels through a dispersing element like a diffraction grating as used in a spectrometer. The spectrometer is able to split the incident light into its constituent wavelengths with a very high resolution so that the photon detector at the exit slit of the spectrometer can generate a plot of light intensity versus wavelength called a spectrum. Optical emission

spectroscopy is hence a technique that studies the light emitted by the excited atoms and molecules when they transition to the lower energy states at different wavelengths [46].

The OES spectrum gives information about the electronic structure of the molecule [46]. Hence by using OES for the linear diatomic nitrogen molecule, we can extract information about the rotational and vibrational bands approximated by the rigid rotor and harmonic oscillator models [45]. The solutions for the Schrodinger equations of these models give us the energies associated with the respective rotational and vibrational energy levels [45].

3.3.1.1. OES instrumentation overview

Figure 6 shows the internal diagram of the Spex 1000M spectrometer [47].
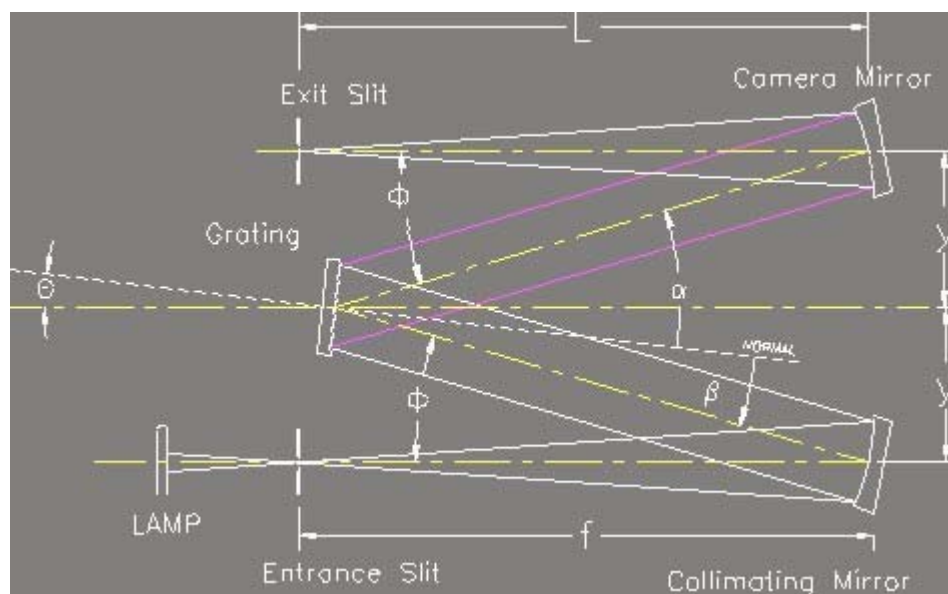
Figure 6. Spectrometer and internal components

A focusing lens is in place to focus the light emission being studied onto the entrance slit. The light enters the spectrometer through the entrance slit which is exactly at the **focal length** of **1 m** of the collimating mirror. The entrance slit is set to an opening of **100 μm** for all the acquired spectra. This value of the entrance slit was experimentally found to provide the enough spectral resolution for resolving the rotational levels and ensuring adequate incident light intensity. The Collimating mirror reflects the incident light onto the diffraction grating.

The grating serves as the dispersing element to split up the light into its constituent wavelengths over a range of **190 - 750 nm** being discontinuous over 0 - 190 nm. It has a set of precisely ruled grooves at equal intervals and is characterized by the number of grooves per mm. The fineness of the grating is one the factors that determines the minimum resolution with which two wavelengths of light can be separated from each other by the spectrometer. The diffraction grating in the spectrometer has **2400 grooves /mm** giving a resolution of **0.5 nm /rotation** of the spectrometer motor which turns the grating thus focusing different wavelengths onto the optical center of the camera mirror.

The Camera mirror transfers the separated wavelengths onto the focus at the exit. The exit port at the focus of the camera mirror serves as a mount for the photo detector. A Hamamatsu Photo multiplier tube (PMT) [48] and the 4 Picos digital ICCD camera [49] serve as the photo detectors used in our system.

3.3.1.2. GPIB interface for spectrometer control

A Labview based virtual instrument (VI) module was developed to communicate with the Spex 1000M. The communication was established through GPIB via the MSD controller hardware that communicates with the spectrometer. Figure 7 shows the customized dashboard designed in the spectrometer driver VI at a level above the internal Labview based VI's developed by the spectrometer manufacturer, HORIBA Jobin Yvon [47]. The driver VI controlled which VI function from the manufacturers VI's had to be called to send commands to the spectrometer as well as receive status messages from it.
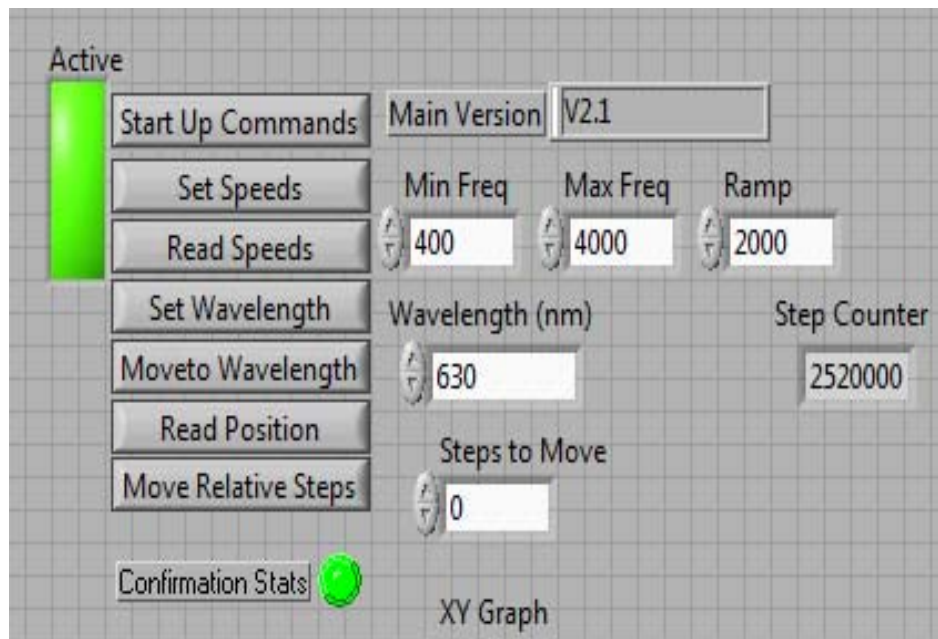
Figure 7. Labview virtual instrument to communicate with spectrometer

3.3.1.3. Spectrometer calibration

A mercury vapor lamp was used as the light source for calibrating the spectrometer motor. 5 visible known wavelengths at 404.65 nm, 435.83 nm, 546.07 nm, 578.96 nm and 579.06 nm emitted by the mercury vapor lamp [50] along with the white light at 0 nm were captured by mounting the Micrometrics camera at the exit slit to image the atomic lines. Figure 8 shows the atomic line imaged at 435.8 nm.
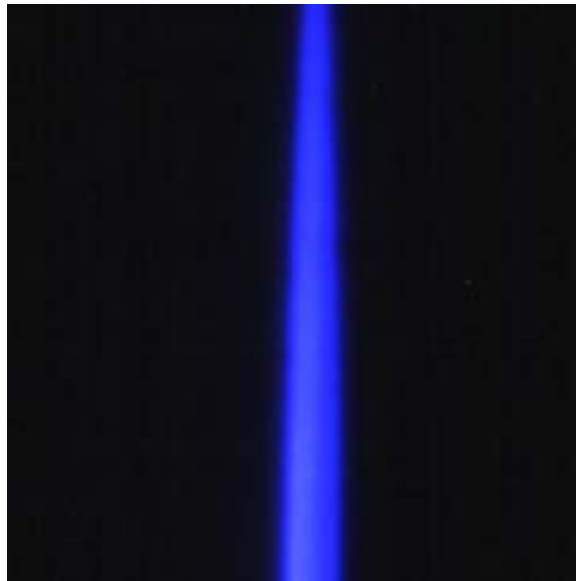
Figure 8. 435.8 nm line seen by the micrometrics camera on exit slit

With a known resolution of **4000 steps /rotation** corresponding to **0.5 nm /rotation or 0.000125 nm /step**, a steps counter was implemented to measure the steps the spectrometer moves through to the six known wavelengths having a relative intensity high enough to be seen by the Micrometrics camera over the 750 nm range. A third order fitting function was developed using MATLAB to fit the steps /nm data and inserted into

the spectrometer driver VI module. The procedure was extremely successful providing highly accurate control over the spectrometer positioning especially in the visible range where our experiments are concentrated.

3.3.1.4. Optical encoder

An optical encoder disc from US digital [51] was mounted on the shaft of the spectrometer motor to get an accurate readout of the spectrometer position. The encoder was specified at **1000 cycles per rotation** thus providing **4000 pulses per rotation** in the quadrature mode on the National Instruments (NI) counter input module [52]. The spectrometer position read through the encoder thus provided the wavelength input to the spectra plotting VI with a resolution of **0.000125 nm / step count**.

3.3.1.5. Photo multiplier tube (PMT)

The Hamamatsu PMT was one of the photo detectors used in the OES instrumentation set-up. The PMT consists of a series of plates each maintained at a higher voltage than the previous in an evacuated glass chamber. The photons strike the first plate through the thin inlet slit on the PMT module which is mounted on the exit port of the spectrometer. Each photon knocks off electrons from the electrode plate which further knock off secondary electrons from subsequent plates creating an avalanche effect. The resulting electrons serve as the output in the form of current proportional to incident number of photons [53]. The gain knob on the PMT controls the voltage of 0 - 1250 V with negative polarity applied to the plates and hence the corresponding output current [48].

The current output from the PMT was then converted into a proportional voltage and fed to the same spectra plotting VI through the analog input channel of the NI card [52]. Care was taken to prevent saturation of the voltage above 5 V to prevent damage to the NI cards as well loss of useful information in the intensity signal. Data was thus available for both intensity and the corresponding wavelength from the encoder and hence the spectra could be plotted. The spectra were stored in .csv format for further MATLAB processing for extracting temperature information about the rotational and vibrational levels for the nitrogen gas used for the microplasma experiments.

3.3.1.6. ICCD camera

The ICCD camera [49] served as the other photo detector used in the experiments. The ICCD provided a resolution of **0.004 nm /pixel**. In a single shot the camera could capture the light emitted over a **5.2 nm band** for our system. Exposure time and intensity gain could be set as per the intensity of the incident light. An exposure time of **100 microseconds** was used to prevent saturation of the pixels with the gain voltage and the digital CCD gain both maxed out at **1000** and **20 db** respectively. The 4 SpecE software package [49] for camera control provided features like the background subtracting, averaging over rows or columns in the image, taking the average of multiple shots etc. 300 shots were taken and averaged for the temperature measurements made later in section 5.

3.3.2. Modeled nitrogen spectra

This section explains the rotational and vibrational temperature estimation model for nitrogen for the microplasma experiments later in section 5.

3.3.2.1. Nitrogen 2nd positive system

The model tries to simulate the light emitted by excited nitrogen molecules in the wavelength band of 365 nm to 381 nm. A set of molecular transitions is observed in this wavelength band. These transitions represent the transition of the nitrogen molecule from excited electronic state 'C' to an electronic state 'B' of a lower energy. The rotational and vibrational transitions are coupled to the electronic transition but are much weaker than the 1 eV to 2 eV electronic transitions. The transitions for the vibrational levels having $\Delta = 2$ are seen in the 365 nm to 381 nm region along with their intermediate rotational levels [54]. The energies of these rotational transitions are extremely small at 0.01 eV and hence represented by a line feature as narrow at 0.05 nm. Vibrational transitions are stronger with energy levels of 0.1 eV providing 1 nm wide band heads.

A code was developed in MATALB using data from Herzberg [55], to determine the locations of the peaks for the C-B nitrogen molecule transition.

The code and the data are available in the Appendices B and C.

The 0-2, 1-3, 2-4, 3-5 vibrational transitions from the excited state to the lower energy state that lie in the 365 nm – 381 nm ranges that were modeled are highlighted in the

peak locations matrix. Figure 9 shows the peak locations matrix for the C-B 0-0 transition. 0-2, 1-3, 2-4, 3-5 transitions that is the 2nd Positive system is selected for modeling due to lack of overlap of other transitions in the wavelength range [56]. Two adjacent vibrational band heads and intermediate rotational levels are required to make temperature approximations in the model [54, 56].

Initial Vibrational Level

	0	1	2	3	4	5
0	337.0343	315.8108	297.5750	281.8569	268.2855	256.5666
1	357.5847	333.7855	313.4816	296.0872	281.1472	268.3046
2	380.3847	353.5677	330.8676	311.5498	295.0521	280.9396
3	405.8131	375.4341	349.9406	328.4039	310.1253	294.5721
4	434.3382	399.7204	370.9484	346.8373	326.5127	309.3179
5	466.5458	426.8383	394.1894	367.0728	344.3849	325.3113

Final vibrational level

Figure 9. Nitrogen peak locations for the C-B 0-0 transition at 337 nm.

Modeled transitions in the 365 nm – 381 nm band with $\Delta = 2$

3.3.2.2. Rotational, vibrational and electronic energies

All the energy components were expressed in units of wave number. The energies T_c and T_b of the electronic states C and B were directly available in Herzberg [55].

For a linear diatomic molecule like nitrogen, certain approximations can be made to estimate its rotation and vibration. The approximations for the rigid rotor with higher order terms and the harmonic oscillator with aharmonicity terms are used for getting

solutions to the Schrodinger equations for the rotational and vibrational energies for each specific rotational and vibrational level for the model [45].

Equation 4 gives the energy for any rotational energy level 'J' according to the solution of the rigid rotor approximation [45, 54].

$$F (J) = B_e J (J+1) - D_e J^2 (J+1)^2 \qquad J = 0, 1, 2, \ldots\ldots$$

(4)

Equation 4. Energy of rotational levels

Where, B_e is the rotational constant and D_e is the centrifugal distortion constant and is also a function of the Vibrational energy associated with the given rotational level.

Equation 5 gives the energy for any vibrational energy level 'v' according to the solution of the harmonic oscillator approximation [45, 54].

$$G (v) = w_e (v+1/2) - w_e x_e (v+1/2)^2 + w_e y_e (v+1/2)^3$$

(5)

Equation 5. Energy of vibrational levels

where, w_e is the vibration wave number of a classical oscillator with $w_e x_e$ and $w_e y_e$ representing the anharmonic constants

The total energy is thus calculated. Equation 6 gives the total energy of the rotational and vibrational levels and electronic states for the C and B states.

$$E_c = T_c + G (v) + F (J) \qquad E_b = T_b + G (v) + F (J)$$

(6)

Equation 6. Total energy for rotational and vibrational levels

Thus for the vibration transitions 0-2, 1-3, 2-4, 3-5 from the higher energy state to the lower state and by using an approximation of 50 rotational levels with J_{max} = 50 in the code, the energy associated with each rotational level along with the vibrational levels (J = 0) was calculated.

The difference between two energy levels was used to determine the wavelength at which each transition would occur along with the emission intensity depending on the population at that particular level [54]. Equation 7 gives the population at given level.

$$\mathbf{n\ (J,\ v) = (2J+1)\ exp\ (-h\ c\ (\ T\ /\ (k_b T_{elec}) + G\ (v)/\ (k_b T_{vib})\ + F\ (J)/\ (k_b T_{rot})\ )\ )}$$

(7)

Equation 7. Population at energy level

where, k_b = Boltzmann's constant

   h = Planck's constant

   c = velocity of light

Thus the equation for the ratio of the intensities I for atoms A and B with n, J, v and m, w, k as the electronic, rotational and vibrational levels respectively is given in Figure 10.

$$\frac{I_{A,n,J,v}}{I_{B,m,K,w}} = \frac{n_A}{n_B}\frac{k_{A,n,J,v}}{k_{B,m,K,w}} \frac{\dfrac{g_J e^{\frac{-\varepsilon_J}{T_{Rot}}} g_v e^{\frac{-\varepsilon_v}{T_{Vib}}} g_n e^{\frac{-\varepsilon_n}{T_{el}}}}{\displaystyle\sum_n\sum_v\sum_J g_J e^{\frac{-\varepsilon_J}{T_{Rot}}} g_v e^{\frac{-\varepsilon_v}{T_{Vib}}} g_n e^{\frac{-\varepsilon_n}{T_{el}}}}}{\dfrac{g_K e^{\frac{-\varepsilon_K}{T_{Rot}}} g_w e^{\frac{-\varepsilon_w}{T_{Vib}}} g_m e^{\frac{-\varepsilon_m}{T_{el}}}}{\displaystyle\sum_m\sum_w\sum_K g_K e^{\frac{-\varepsilon_K}{T_{Rot}}} g_w e^{\frac{-\varepsilon_w}{T_{Vib}}} g_m e^{\frac{-\varepsilon_m}{T_{el}}}}}$$

Figure 10. Ratio of intensities between energy levels

As in this experiment we are modeling the 0-0 transition and the species is nitrogen for both energy levels the electron temperature dependence and the number density dependence get eliminated. The vibrational and rotational temperatures, T_{vib} and T_{rot} alone determine the intensity of emission. Equation 8 gives the emission intensity.

$$\textbf{Emission intensity} = \textbf{f}(\textbf{T}_{\textbf{rot}}, \textbf{T}_{\textbf{vib}})$$

$$(8)$$

Equation 8. Simplified equation for the 0-0 transition in nitrogen

T_{rot} and T_{vib} are hence varied to obtain the best possible fit between the experimentally acquired spectra and the modeled version [56].

3.3.2.3. Additional modeling considerations

Three other factors were considered before convoluting the modeled spectra with the slit function.

These factors were the Honl-London factor, the Franck-Condon factor and the line alteration factor [54]. These factors are functions of the rotational level 'J' or vibrational level 'v' associated with each peak location and are multiplied with the calculated populations to get the final intensities for each location [54].

3.3.2.3.1. Honl-London factor

The Honl-London factor is a function of the rotational level J. The Honl-London factor represents the rotational line strength for spin allowed transitions. It indicates the distribution of the total intensity of a transition amongst the P-Q-R branches of a rotational level [54]. Formulae for calculating the same are given in Herzberg [55]. The Honl-London factors can be found tabulated [57] or can be calculated numerically as described in the literature [58].

3.3.2.3.2. Franck-Condon factor

The Franck-Condon factor is a function of the vibrational transition and is dependent on the vibrational levels in the higher and lower energy states between which the transition occurs. The Franck-Condon factor is a measure of the distribution of the intrinsic line strength of the electronic transition amongst the combination of vibrational bands [54]. The Franck-Condon factors for the C-B transition in the modeled 2nd positive system are found in literature [59].

3.3.2.3.3. Line alteration factor

The line alteration factor is a function of the rotational level 'J', the effective parity of the upper level of transition and the electronic state of the upper level. The line alteration factor represents the alteration in line intensities due to nuclear spin in diatomic molecules. The formulae for determining the line alteration factors are given in literature [54].

3.3.2.4. Full width half maximum and slit convolution

The convolution function is introduced to account for the features introduced due to the Spectrometer instrument. The slit convolution feature thus convolutes the transfer function of the light emission system with the slit function of the Spectroscopy instrumentation experimentally measured to be 0.1 nm. The net effect is that the model can incorporate the effect of the inlet slit into its estimation thus accounting for limitations of the instrumentation in acquiring data.

A Gaussian slit function was generated in MATLAB and convoluted with the intensity model in the 365 - 381 nm wavelength range. The full width half maximum [60] represents the width in nanometers of the Gaussian slit function at half the maximum intensity.

A variable called FWHM or the full width half maximum of the Gaussian function was used to generate the slit function and approximate the instrument slit function to obtain the best fit with experimental data.

3.3.2.5. Final modeled spectra
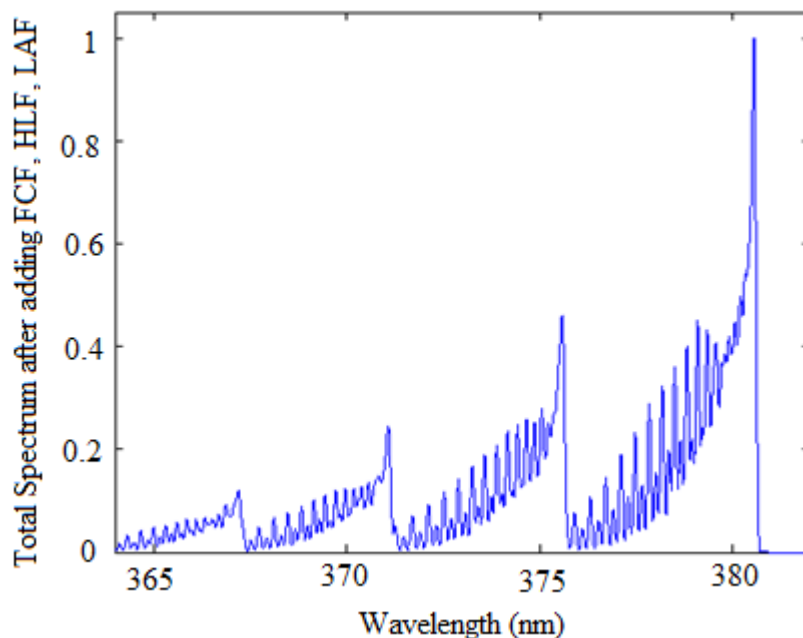
Figure 11. Modeled spectrum for the nitrogen 2nd positive system.

T_{rot} = 1200 K, T_{vib} = 4000 K, T_{elec} = 10000 K, FWHM = 0.1 nm

Figure 11 shows the C-B transitions for the nitrogen 2nd positive system thus modeled with the control variables being rotational temperature T_{rot}, vibrational temperature T_{vib}, electronic temperature T_{elec} and FWHM. The number of rotational levels modeled were set using J_{max} = 50. The model also generated the contributions of the P-Q-R branches for each rotational level. This was an additional feature of the generated model but was not used henceforth in determining the temperature fit for the experimental data acquired from the Spex 1000M spectrometer and its photo detector set-up. The code for the model is given in Appendix B.

3.3.3. Modified SPECAIR model

The nitrogen spectra model generated in the previous section is merged with the SPECAIR program [54] to get a modified SPECAIR [56, 61] MATLAB code. A 6 parameter fitting algorithm is designed to best fit the model with the acquired experimental spectra.

Three additional fitting parameters namely background intensity offset, wavelength offset and wavelength dispersion are introduced for fitting the model to the experimental data along with control over T_{rot}, T_{vib} and FWHM [56, 61]. The modeled spectrum is loaded from pre-stored data within the SPECAIR database and the experimental data is loaded in .csv format for comparison with the model.

The convolution range is set as per requirement in the 365 nm - 381 nm wavelength range. The 6 parameter fitting functions attempts to minimize the root mean square error (RMSE) between the model and the experimental data. The modified SPECAIR model thus attempts to reach a minimum RMSE through a process of successive guesses over a set interval for each parameter using the Nelder Mead simplex search method [62].

The MATLAB program is provided with a Batch function to fit multiple data sets on its own. The program goes through a long series of pre-selected iterations in its efforts to minimize the RMSE. Efforts are made to reduce the RMSE to a value as small as possible. A high RMSE gives a wide variation in the approximated temperatures when the 6 dimensional space of the fitting function is considered. Good temperature fits are

said to be attained for RMSE's between 0 - 3 % [56, 61]. Figure 12 shows an experimental result of the Modified SPECAIR Model.
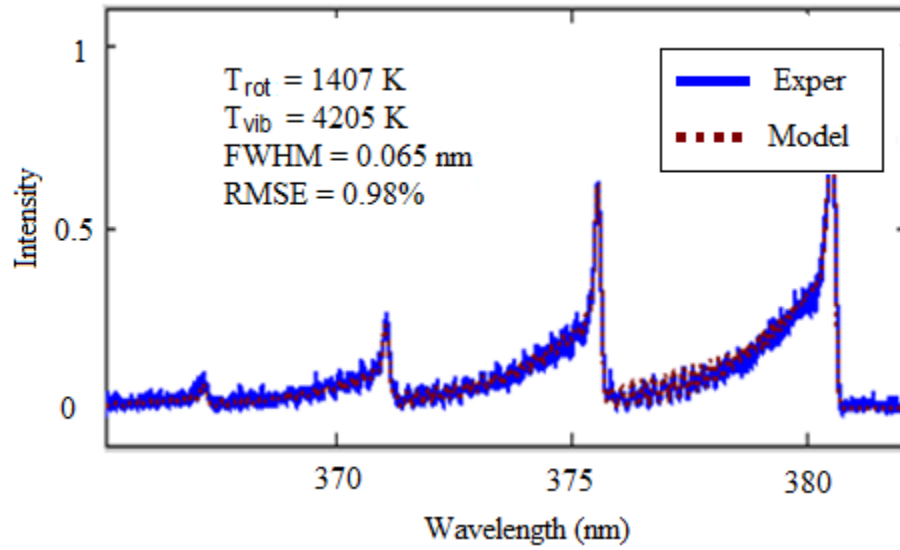
Figure 12. SPECAIR fits experimental data with the model to get temperatures

4. EXPERIMENTAL SETUP, PROCEDURES AND PRELIMINARY RUNS

4.1. Experimental set-up

The microplasma discharge configuration to be implemented was relatively simple with the microplasma to be generated between two electrodes in line with each other. The electrodes were to be mounted such that the distance between them was extremely small to the tune of a few hundred microns to start with.

4.1.1. Microplasma configuration requirements

A $1/16^{th}$ inch diameter stainless steel rod and a piece of nickel coated copper served as the cathode and the anode electrodes. Figure 13 shows the electrode configuration in place for the experiment.
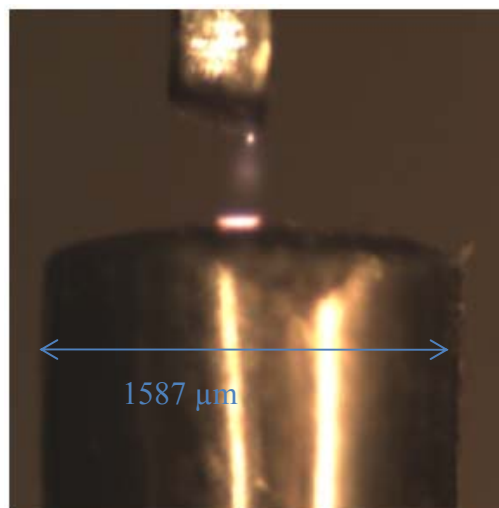
Figure 13. Microplasma configuration.

SS cathode (lower electrode) and Nickel coated copper anode (upper electrode)

A high voltage of around 2 - 5 KV was applied to create a breakdown between the electrodes [2, 15]. The experiment results were insensitive to the material of the anode.

4.1.2. Pressure chamber design

One important aspect of the study was to characterize the effect of pressure on the size of the discharge size of the microplasma. The microplasma discharge thus had to be studied at conditions of greater than atmospheric pressure. The important task was hence to design a pressure chamber that could be used to carry out the plasma discharge in high pressure conditions with controllable pressures.

The electrodes were also to be mounted inside the pressure chamber. The pressure chamber was required to have inlet and outlet ports for the high pressure gas flow. An important and tricky part was to have a high voltage feed through into the chamber in order to have one of the electrodes at the high voltage required to break down the medium between the two electrodes.

Another requirement at the time when the pressure chamber design was being contemplated was the requirement of a window to visualize the microplasma discharge from outside.

Taking the above into consideration the pressure chamber was designed with the following primary requirements:

a. Ability to create an environment where the pressure in the chamber can be controlled to a level as high as possible. The pressure chamber must also be leak-proof.

b. The pressure chamber must have a high pressure inlet port and a pressure exhaust port provided with a control valve at the outlet.

c. There must be a way to measure and control the pressure in the chamber.

d. The electrode setup must be mounted inside the chamber with the gap between the two electrodes set in the range of a few hundred μm.

e. A high voltage feed through must be provided to have one of the electrodes at the required high potential.

f. There must be an optical window provided to see the microplasma discharge taking place while the system is in operation at various high pressures.

g. The limit to which the pressure in the chamber could be increased would depend on the upper limit of the weakest element in the system.

Sanitary fittings rated up to 1500 psia inspired the general design concept of the plasma chamber. The sanitary fittings were procured from a Texas based company called St. Pat's of Texas [63]. These sanitary fittings in the form of stainless steel T sections, crosses and flanges and clamp locks to connect the parts served as an extremely efficient and economical way to build a pressure chamber with the above mentioned primary requirements. An added advantage of the sanitary fitting was that the pressure chamber configuration was extremely flexible and easy for modification.

Figures 14 and 15 show the pressure chamber constituted of a T section and a Cross section held together by a stainless steel sanitary clamp. 5 ports were available after one

port each on the T section and the cross section were used up in clamping the two together. Heavy duty bolted clamps rated up to 1500 psia were used for clamping.
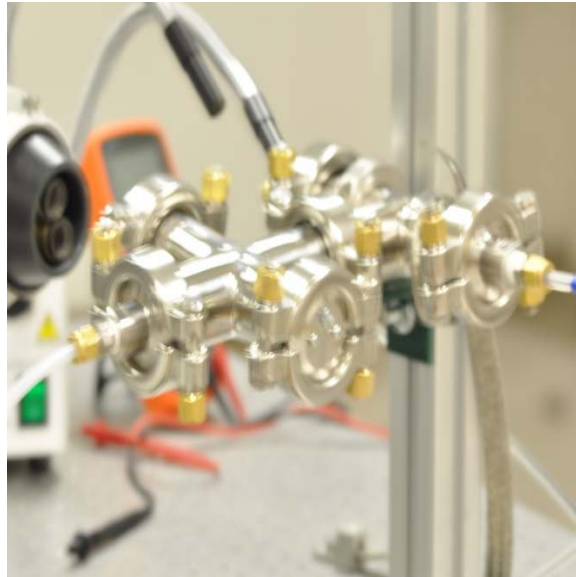

Figure 14. Installed microplasma pressure chamber

Inlet and outlet pressure connections were provided using $1/4^{th}$ inch compression fittings rated up to 1600 psia. The compression fittings were screwed into compatible threads of female pipe thread adapters. A needle valve rated up to 2000 psia was provided in the exhaust line.

The high voltage feed through required for having one of the electrodes at high potential up to 20 KV was manufactured by feeding the high voltage silicon wire through another modified $1/4^{th}$ inch compression fitting screwed into a similar female pipe thread adapter fitting at one of the ports. The inside of the compression fitting was drilled out using a quarter inch drill bill to allow the silicon wire to enter the vessel ensuring there is no

electrical break. The multi stranded core was replaced by a solid stainless steel rod. The compression fitting would seal the solid core silicon wire well enough for our operation at 240 psia. A high pressure glass window rated up to 250 psia was mounted on the sanitary fitting cross section. This provided a visual into the plasma chamber during operation but limited the chamber pressure to 250 psia. An acrylic window rated up to 150 psia was another option used to view into the chamber.
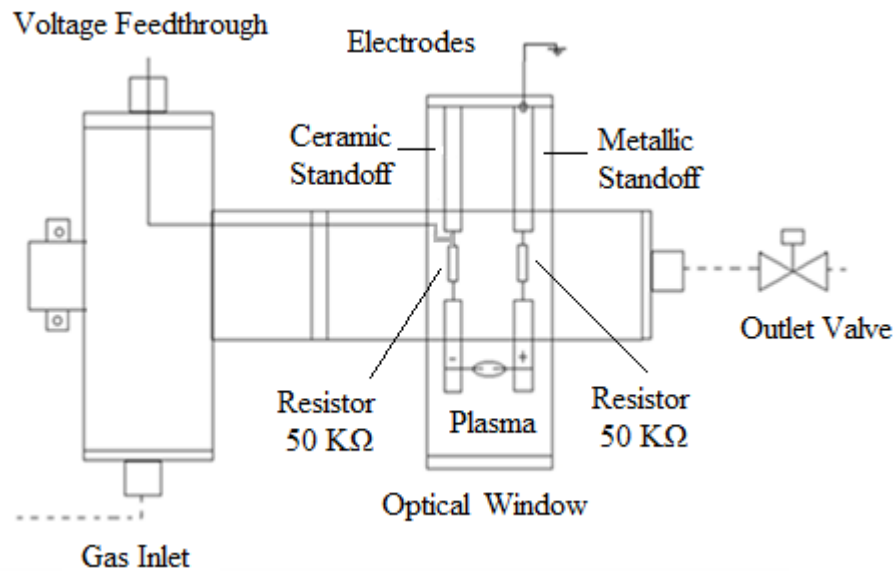

Figure 15. Microplasma pressure chamber with various ports

4.1.3. Complete experimental set-up

It was decided to have one of the electrodes as well as the whole metallic pressure chamber body at a ground potential to provide safety as well as ease of moving the chamber during the operation of the microplasma discharge. The pressure chamber is mounted on a bracket on the optics table and grounded through the connecting bracket as

well as by adding a grounding strap clamped to the pressure chamber body. The feedthroughs for the gas and high voltage are provided along with the optical window as discussed in the previous section. Figure 16 shows the chamber and instrumentation in place.
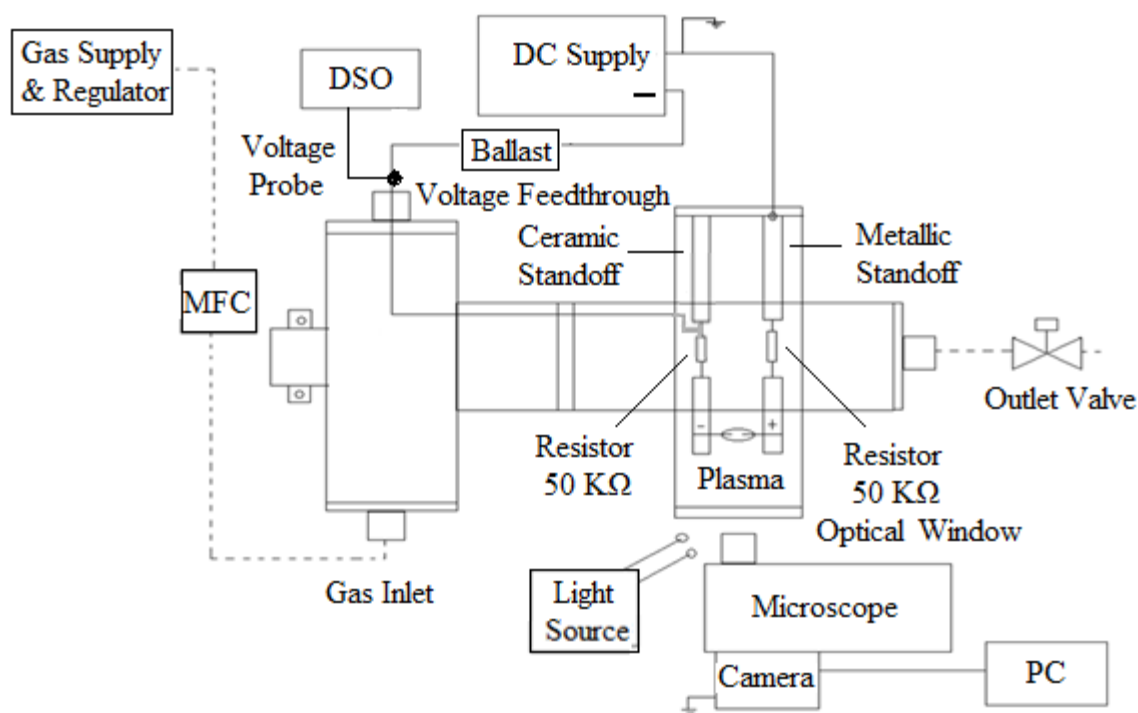
Figure 16. Complete instrumentation set-up overview

4.1.3.1. Pneumatic lines and ports

The pressure in the plasma chamber was controlled by inserting an Alicat Mass flow controller [64] in the inlet pressure line. The controller was set to loop on pressure as per the gas under study in the pressure chamber. The $1/4^{th}$ inch tubing was used to connect the pressure line from the gas cylinders to the chamber at the inlet port. The pressure

chamber was pressure tested for possible leakages. Seals at the inlet and outlet ports were provided using the heavy duty bolt clamps along with rubber gaskets. 1/4th inch compression fittings were used to make the pressure connections. The Alicat Mass flow controller was limited to a pressure of 150 psia. A Honeywell pressure transducer [65], Part# MLH500PSB01A, was hence added to the inlet line for pressure measurements greater than 150 psia.

4.1.3.2. Electric connections and electrode mounting

The microplasma discharge was to be initiated by high DC electric potential applied at one of the electrodes with the other electrode at ground potential [2]. A 100 W, 20 KV, 5 mA DC power supply series EH [66] from Glassman High Voltage Inc. was used for the experimentation.

The two electrodes were clamped, one on each of the two standoffs screwed into the tapping's in the stainless steel end disc used to seal the chamber at one of the ports as shown in Figure 15. The power supply provided a negative output potential up to -20 KV. Due to the negative voltage output supplied by the power supply the 1/16th inch diameter stainless steel it connected to, served as the cathode for the plasma reaction. The high voltage silicon wire connection was made using some heat shrink tubing at the ends. The entire pressure chamber was grounded via the ground strap.

4.1.3.3. Voltage and current measurements

A Digital storage oscilloscope from the Le Croy Wave Runner series [67] was used to measure the applied high voltage using a Le Croy PHV4, 1000:1 high voltage probe [67]. Discharge current was measured from the power supply front panel [66]. The resistor R_b (2 MΩ) placed in series with the power supply served as the ballast for dividing the power along with the 50 KΩ R_i resistors. Figure 17 shows the electrical circuit for the microplasma system. The 50 KΩ resistors are later replaced with a single 100 KΩ resistor after modifications in section 4.2.7. The resistors R_i inside the chamber are essential to minimize the stray capacitance and to stabilize the discharge [2].
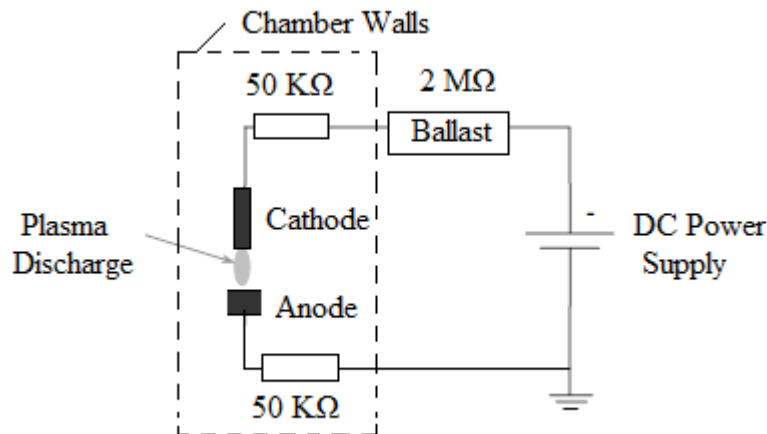
Figure 17. Electrical circuit for the microplasma glow discharge

4.1.3.4. Imaging

The high pressure glass window mounted on one of the pressure chamber ports provided a visual into the plasma discharge region during operation. The microscope was focused

onto the discharge in the plasma chamber through the optical window at the side of the chamber. The focusing and magnification of the microscope was adjusted such that discharge area in between the electrodes in concentrated upon at maximum 4.5X zoom.

The micrometrics camera module [42] was mounted onto the eyepiece of the microscope [43]. The instrumentation enabled microscopic visualization of the discharge area on the Micrometrics Premium SE software on the Computer. The imaging provided a resolution of 1.4 µm/ pixel on the computer screen at maximum magnification on the microscope, without any digital zoom. A light source was required for illuminating the discharge area and focus on the exact electrodes region.

An acrylic window was another option utilized for the imaging. As time wore on, the acrylic material was found to provide better focusing and when used with the microscope and camera setup. This may be attributed to the flatter finish of the surface of the acrylic window and changes in the surface shape of the glass window after being regularly exposed to pressure above 200 psia. The acrylic window rated at 150 psia, failed at a pressure of 165 psia and hence wasn't used for higher pressure imaging.

4.2.   Initial imaging results

The basic goal at this stage was to generate a normal glow discharge at atmospheric pressure and capture it with the camera mounted on the microscope. The gap was set to about a few hundred μm and the camera was focused on to the discharge area between the electrodes at maximum magnification. Figure 18 shows the imaged electrodes.

4.2.1. Basic microplasma imaging and resolution measurement

The 1/16th inch diameter stainless steel rod was used calculate the μm /pixel resolution for the images captured. This would allow us to find the discharge gap length as well as the size for the cathode glow of the microplasma.
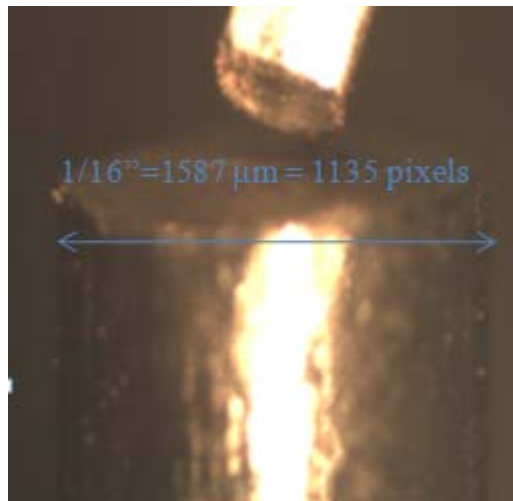

Figure 18. Electrode image at maximum 4.5X magnification

The stainless steel cathode diameter was converted to be 1587 µm. This corresponded to a length of 1135 pixels on the image at full magnification of the camera without any digital zoom giving an imaging resolution of 1.4 µm /pixel.

4.2.2. Imaging issues with camera malfunction

The discharge gap was set around 300 µm. The voltage was increased to around 5 KV with the current at 1.5 mA and the microplasma discharge was struck in nitrogen. Figure 19 is an image of the plasma just before it becomes unstable.

The discharge was however not stabilized and soon began dancing around the surface of the thicker 1/16th inch diameter stainless steel cathode electrode. This instability in the plasma creates an electromagnetic interference which can hamper the operation of nearby electrical systems.
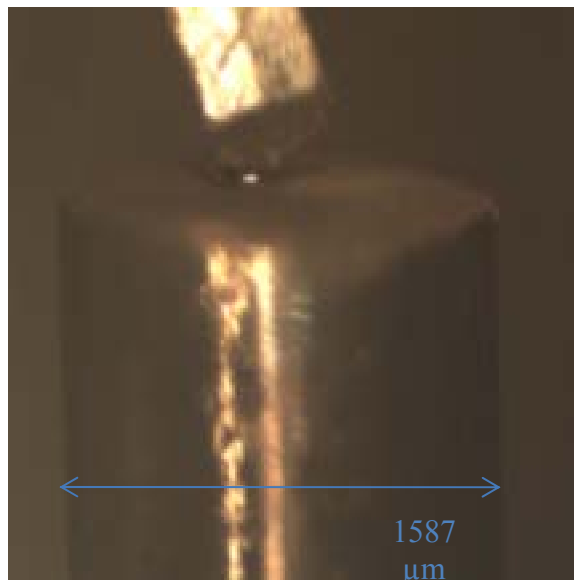
**Figure 19.** Microplasma imaging malfunction issue

The electromagnetic interference problem prevented the camera from capturing the microplasma discharge upon breakdown. Immediately the camera used to hang up when the plasma became unstable. The Micrometrics SE premium software used to malfunction and go into a "Not Responding" mode upon which the only option was to reboot the software.

In short the camera was not able to handle the microplasma unless it was stabilized. Any AC element in current due to the instability was creating an interference that was resulting in the camera's electronics to malfunction and for a safety shutdown to be triggered.

The problem was overcome with a very simple solution. The metal body of the camera was connected to ground using grounding strap. This turned out to be an excellent shield to filter out the AC component that was interfering with the camera's circuitry. After the issue was solved we went ahead with the preliminary work of capturing the discharge in helium and nitrogen at atmospheric pressure.

4.2.3. Captured images in helium and nitrogen

The initial experiments started off with the nitrogen and helium gas at atmospheric pressures. Figures 20 and 21 show the discharge zoomed in digitally in helium and nitrogen.
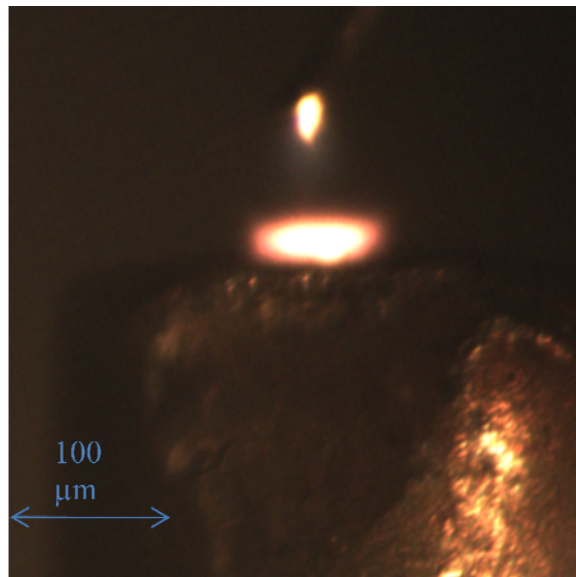
**Figure 20.** Microplasma discharge in helium
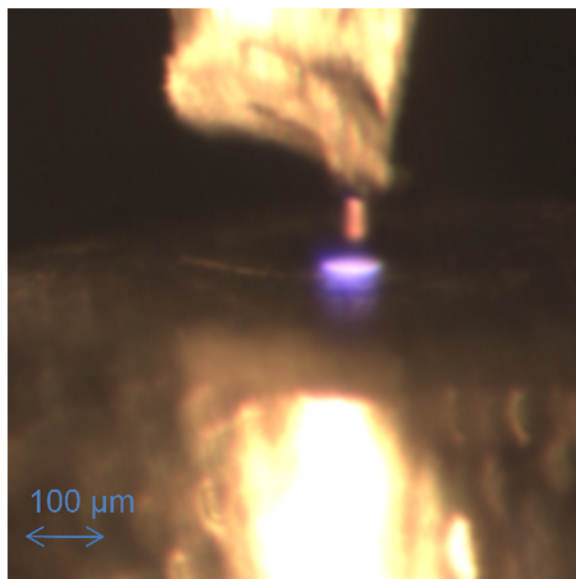
Figure 21. Microplasma discharge in nitrogen

4.2.4. Preliminary experiments

The variation in discharge size with variation in current and pressure were to be studied in helium and nitrogen.

4.2.4.1. Variation of discharge current

This preliminary experiment was carried out in helium to study the effect of current variation on the discharge size. The size of the cathode glow representing the discharge size was calculated from the images obtained. The MATLAB based Analyze Image Size code was used to automate the process of measuring the discharge. The discharge gap was set to 50 µm and the pressure held constant at 50 psi with the electrode set-up. Figure 22 shows the electrode set-up.
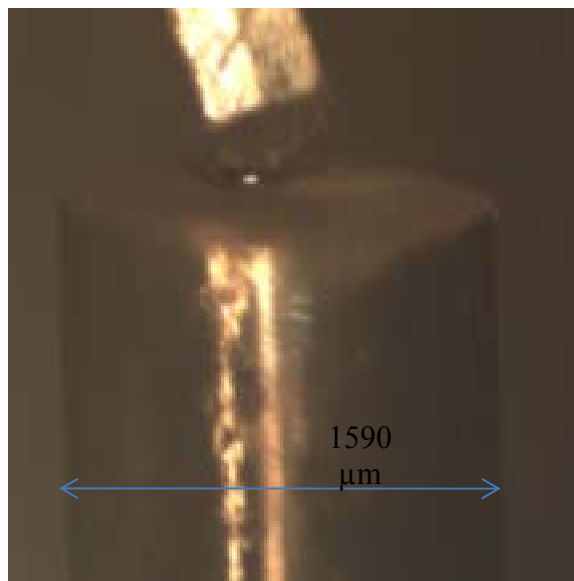
**Figure 22.** Experimental set-up for preliminary experiments in helium.

50 psia, 50 µm gap, R = 2.1 MΩ

Figure 23 shows the captured images with current varying from 1 mA to 0.4 mA with the pressure held constant at 50 psia. The images were digitally zoomed in to focus in on the region of interest. The light source was turned off to only visualize the plasma as required by the MATLAB Analyze image size code.
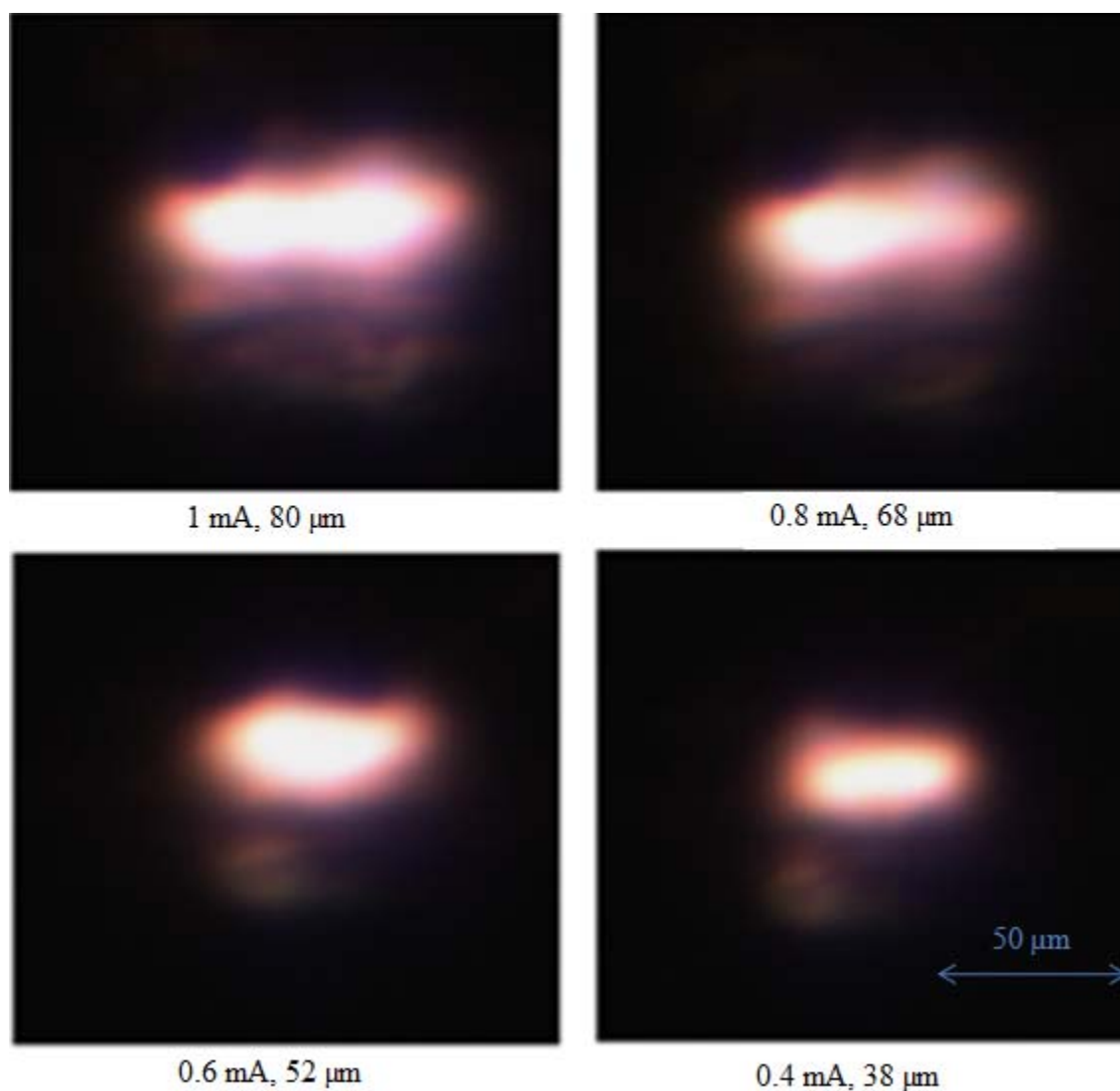

Figure 23. Variation of discharge size with current preliminary readings.

P = 50 psia, 50 μm gap, R = 2.1 MΩ

4.2.4.2. Variation of pressure

This preliminary experiment was carried out in nitrogen with the aim of studying the effect of pressure variation on discharge size. The discharge gap was set to 150 μm. Discharge current was fixed at 1 mA with the pressure in the chamber being varied between 15 psia and 90 psia. Figure 24 shows the variation in discharge size.
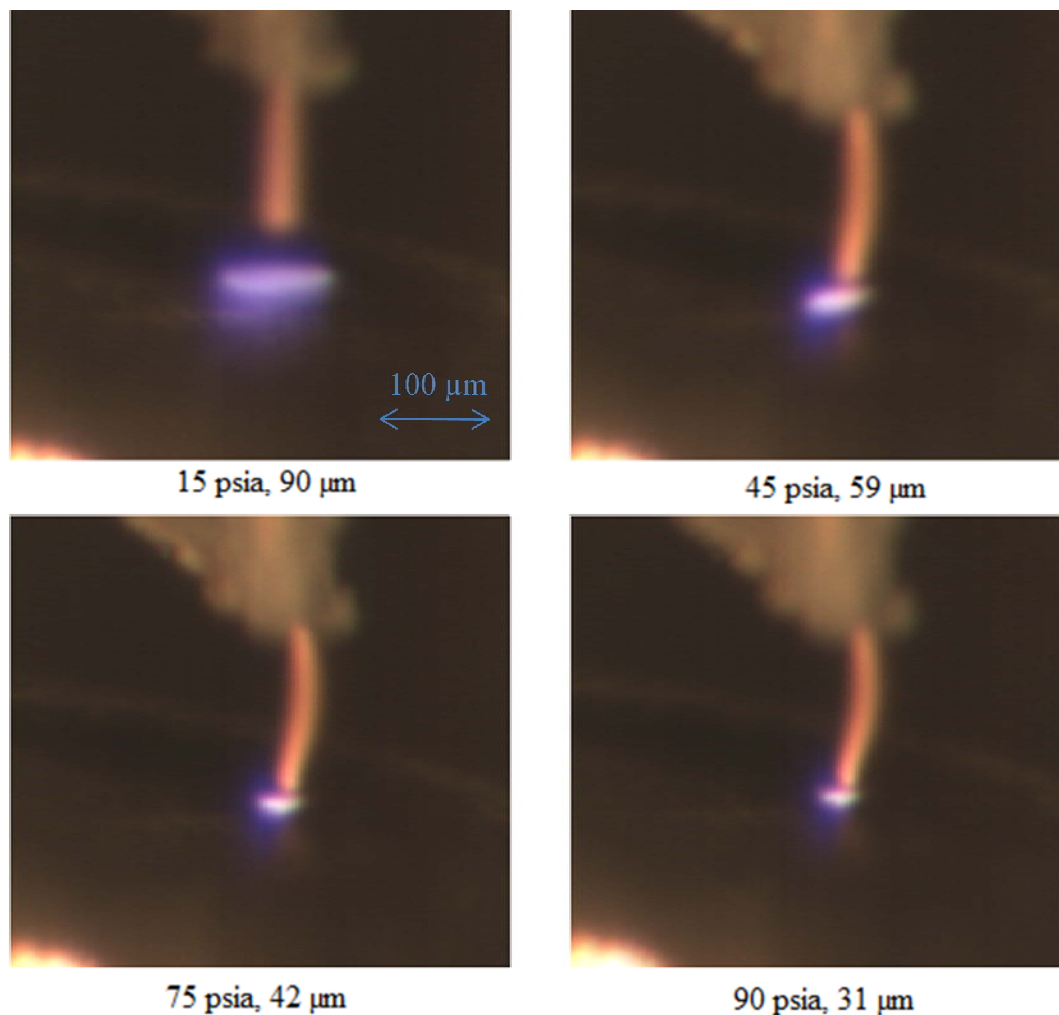
Figure 24. Variation with pressure preliminary readings in nitrogen.

Current = 1 mA, R = 2.1 MΩ, d = 150 μm

The discharge size was obtained from the images using the Analyze Image size code. The images and the calculated discharge sizes from the two experiments were studied to understand the effect of discharge current and pressure variation on the size of the microplasma to figure out the associated trends.

4.2.5. Results from preliminary experiments

Table 1 and Table 2 summarize the two preliminary experiments. Discharge voltage is calculated by as $V_d = V_a - (R_b + R_i) I$

4.2.5.1. Variation in discharge current

The discharge size was found to decrease with decrease in discharge current.

Table 1. Variation of discharge size with current preliminary readings.

Helium, 50 µm gap, R = 2.1 MΩ

Pressure (psia)	Discharge Current I (mA)	Applied Voltage V_{ap} (KV)	Discharge Voltage V_d (V)	Discharge Size (µm)
50	1.0	2.336	236	80
50	0.8	1.887	207	69
50	0.6	1.521	261	52
50	0.4	1.053	213	38

4.2.5.2. Variation in pressure

The discharge size was found to decrease with increase in nitrogen pressure.

Table 2. Variation of discharge size with pressure preliminary readings.

Nitrogen, 150 μm gap, R = 2.1 MΩ

| Pressure (psia)	Discharge Current I (mA)	Applied Voltage V_{ap} (KV)	Discharge Voltage V_d (V)	Discharge Size (μm)
15	1	2.358	258	90
45	1	2.365	265	59
75	1	2.461	361	42
90	1	2.475	375	31

4.2.6. Inferences

The goal of the research is to generate a microplasma discharge of the smallest possible discharge size which is characterized by the size of the cathode glow. The preliminary experiments indicate that the discharge size decreases with decreasing discharge current and also decreases with increasing pressure. These results are in accordance with the scaling laws in literature [1, 2, 13, 15]. Thus in order to generate microplasmas that are smaller in size the discharge, experiments hence further were carried out at such high pressure, low current settings.

4.2.7. Required modifications to pressure chamber

During the preliminary experiments, it was realized that certain modifications were needed to be incorporated in the pressure chamber to provide enhanced gap control as well as co-axial windows for visualization and spectroscopy.

4.2.7.1. Installation of micrometer

It was realized that with increasing pressure the electrode discharge gap was varying by 15 to 20 µm most likely due to small deformations of the chamber during pressurization. So the ground electrode was mounted on the shaft of a 2 µm resolution micrometer to provide accurate control of the discharge gap. Figure 25 shows the installed micrometer.
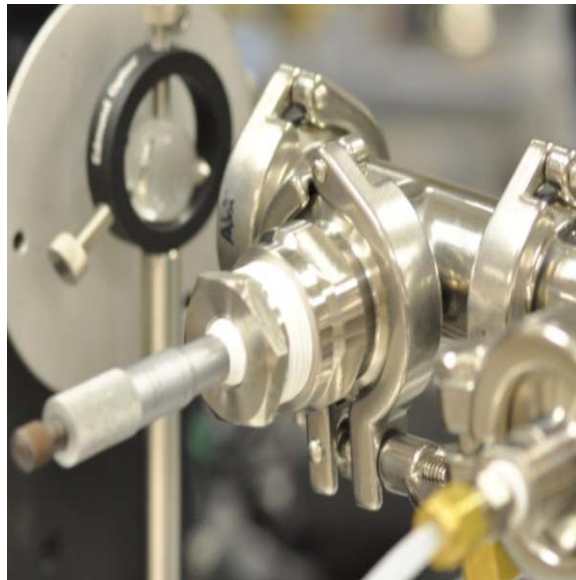
Figure 25. Micrometer installed to control electrode discharge gap

Thus, every time the pressure was increased the discharge gaps needed to be modified by turning the micrometer shaft to not only ensure a stable normal glow discharge but also to try and maintain the gap between the electrodes at a constant value.

4.2.7.2. Window for spectroscopic measurements

Plasma temperature was another important factor that had to be considered. Rotational and vibrational temperatures measurements were required to be made. The temperature measurements also would provide information about the non-equilibrium or equilibrium nature of the plasma.

 The optical emission spectroscopy technique discussed in section 3 was to be used for the plasma temperature measurement. An additional high pressure optical window was hence required to be mounted on to the chamber body to provide a visual for the spectrometer to capture the emitted light. This required the pressure chamber to have an additional port and thus a subsequent modification in the pressure chamber design.

Optical windows were now required to be present such that the microplasma discharge could be simultaneously imaged using microscopic visualization through one window and the temperature measurements could be done by OES through another coaxial window on the opposite port of a cross section sanitary fitting. Additional instrumentation in the form of a focusing lens, spectrometer and the spectrometer readout device in the form a photomultiplier tube (PMT) or the ICCD camera now entered the microplasma experimentation assembly. Figure 26 shows the modified

pressure chamber diagram and the coaxial windows. Figure 27 shows the modified

chamber and instrumentation in place.
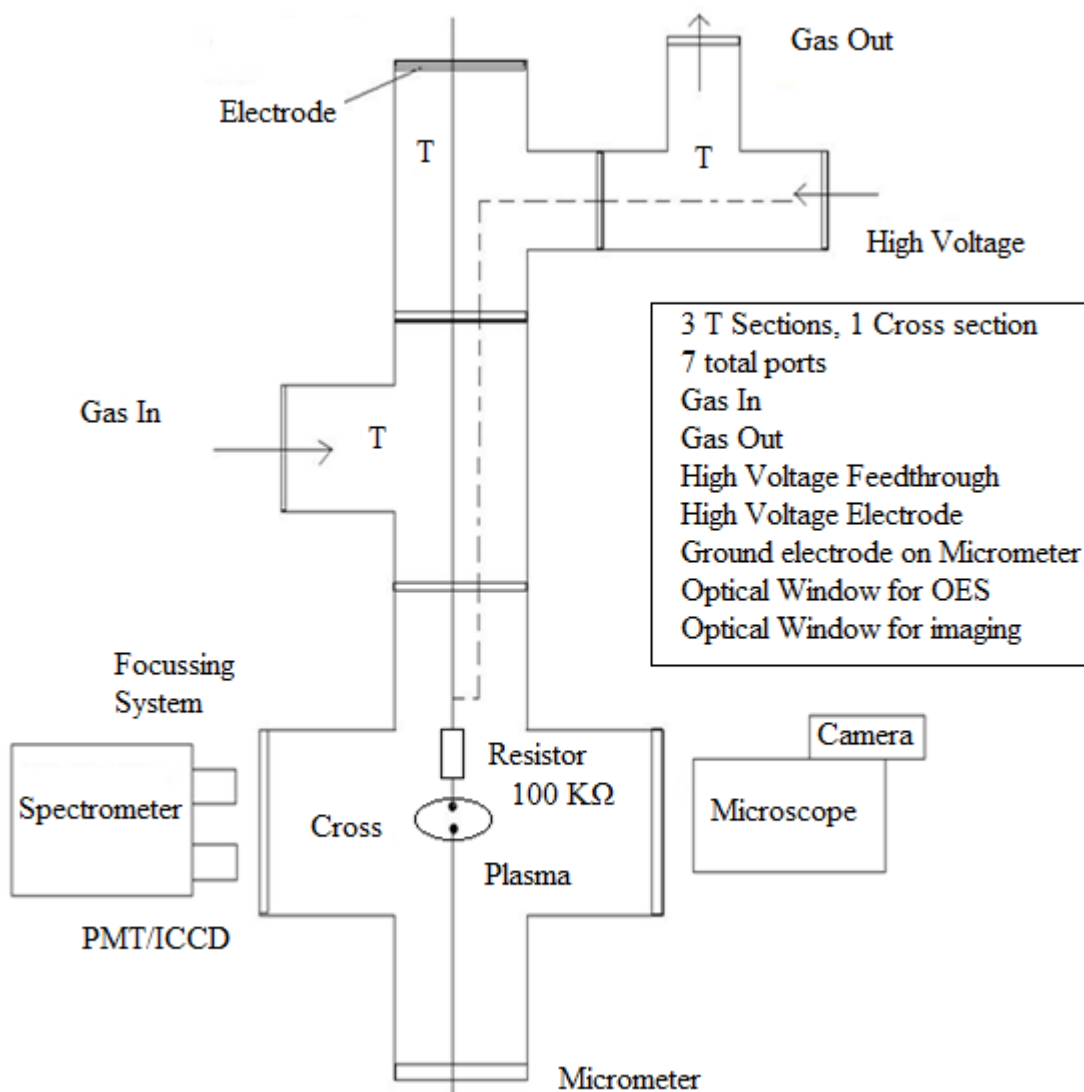
Figure 26. New design of pressure chamber
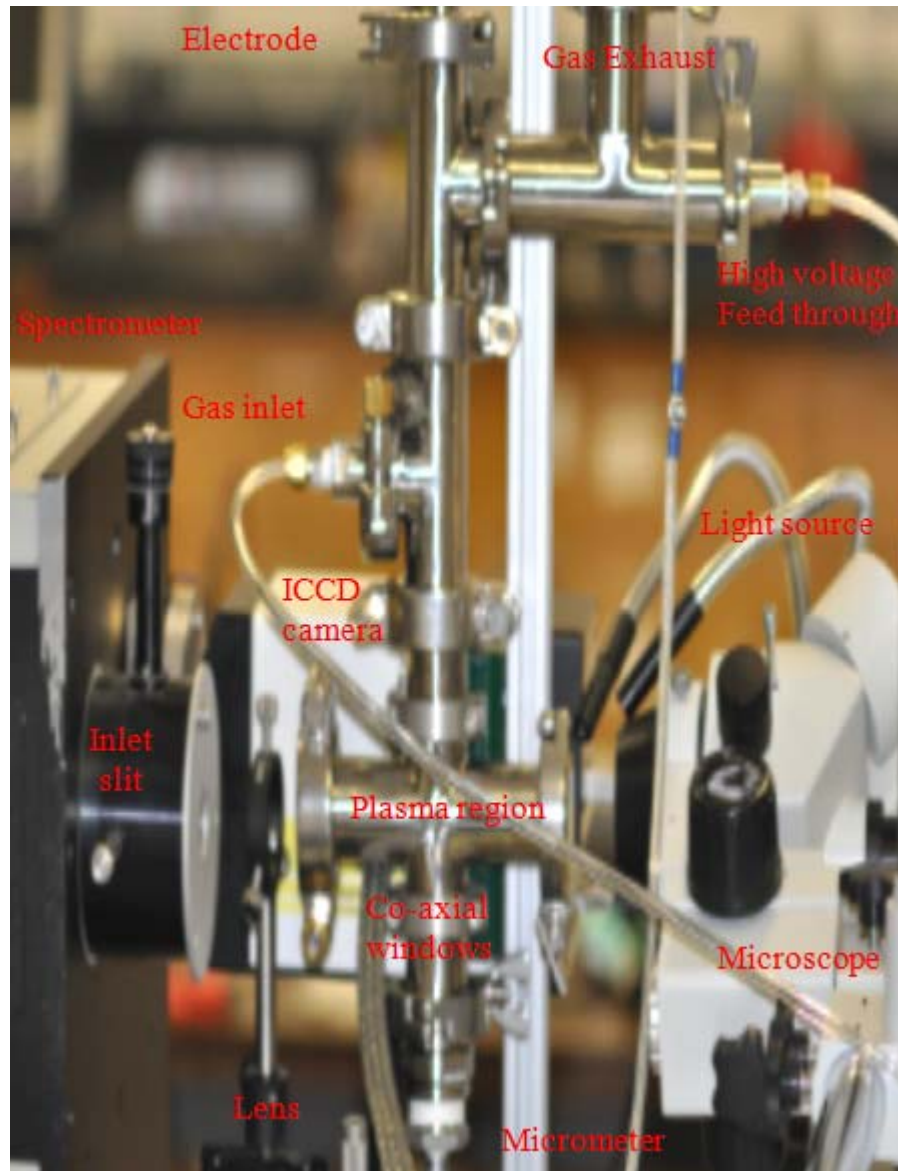
**Figure 27.** OES instrumentation and simultaneous imaging

4.3. Optical emission spectroscopy temperature measurements

Optical emission spectroscopy (OES) was used as the plasma temperature diagnostic tool in experiments described in sections 5.5 and 5.6.

4.3.1. Spectroscopy set-up

Figure 28 shows the OES system which consists of the following instrumentation:

a.   Focusing lens

b.   Spectrometer SPEX 1000M with inlet slit module

c.   Photomultiplier tube or ICCD camera 4 Picos digital
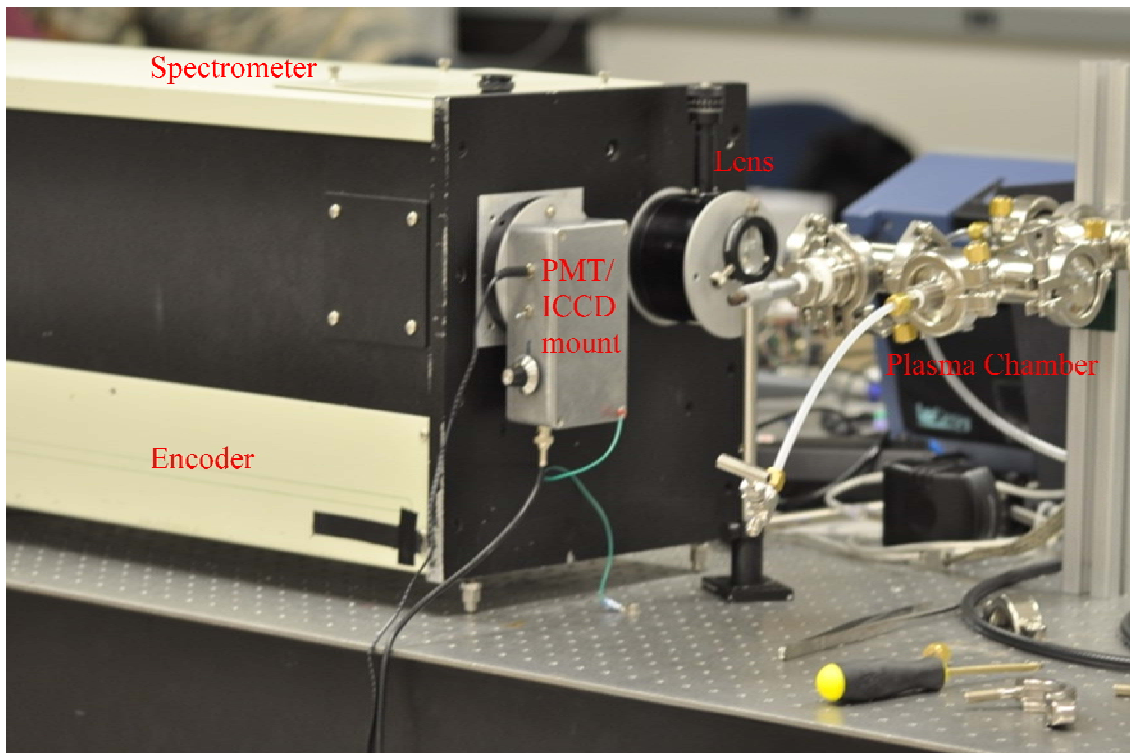
Figure 28. OES set-up for temperature measurement

4.3.1.1. Focusing system

The focusing lens is used to transfer the image of the microplasma discharge inside the pressure chamber onto the inlet slit of the spectrometer. By varying the distance between the lens and the inlet slit the magnification of the image can be varied. The inlet slit is also fit with an extra disc to keep out as much stray light as possible to enhance the signal to noise ratio at the photo detector output.

4.3.1.2. Spectrometer positioning

The diffraction grating in the Spectrometer splits up the light incident through the inlet slit into its constituent wavelengths. The inlet slit is kept open at a constant value of 100 μm which was experimentally verified to acquire enough light intensity from the emission and provide adequate spectral resolution for resolving the rotational energy levels.

The temperature measurements are made using the nitrogen 2nd positive system where large molecular vibrational band heads are expected for a C-B 0-2 transition at 380.38 nm and a 1-3 transition at 375.55 nm along with the rotational levels in between them [56, 61]. Hence the Spectrometer motor is moved to this wavelength zone of 375 nm to 381 nm to capture the spectra.

4.3.1.3. Output detector and system alignment

If the PMT is used as the detector at the Spectrometer exit slit, the exact focus of the lens is adjusted so that the output voltage from the PMT is high as possible to get a high

signal to noise ratio. The spectrometer is focused on the 380.5 nm position to capture the strong signal coming from the C-B 0-2 transition. The gain adjustment knob on the PMT is used to ensure that the voltage does not shoot above the 5 V saturation level for the National Instruments card which picks up the signal from the PMT. This procedure ensures the system alignment.

If the ICCD camera is used to acquire spectra, the position of the lens is adjusted till a molecular transition is acquired on screen around 378 nm. Exposure time is adjusted to around 100 microseconds to prevent saturation of any of the pixels. Excessive exposure time can damage the camera as well as result in saturation of the pixel resulting in loss of data and resolution. To ensure the camera isn't saturated on a single exposure the captured light intensity should not exceed the 12 bit value of 4096. Other important aspects of the OES instrumentation are mentioned in section 3.

4.3.2. Acquired spectra

The spectrum represents the plot of intensity versus wavelength captured by the detector installed at the exit slit of the spectrometer. The spectra were acquired in the region wavelength band between 375 nm and 381 nm so as to capture the 0-2 and 1-3 vibrational transitions and the intermediate rotational levels for the C-B transition of the nitrogen 2nd positive system. The PMT and the ICCD camera were the two detectors used for acquiring the spectra.

4.3.2.1. PMT acquired spectra

The data from the PMT is acquired via the Lab view based National Instruments PCI express card interface.

There are two inputs to the interface in the form of wavelength from the encoder and signal intensity from the PMT. The offset wavelength is set at 375 nm on the Lab view module interfaced with the National Instruments PCI express card [52]. The spectrometer is then scanned from 375 nm to 381 nm at a speed of 4000 steps per second which corresponds to a rate of 0.5 nm per second using the GPIB interface. The optical encoder disk mounted on the shaft of the spectrometer motor sends a pulse for each for each step of the motor's rotations and hence the wavelength reading is transferred to the Lab view module through the National Instruments card using its inbuilt digital counter. The current output signal from the PMT [48] is converted into a proportional 0 to 5 V voltage output and input to an analog channel on the National Instruments card. The two inputs are synchronized to obtain a plot of signal intensity versus wavelength in order to get a spectrum. Figure 29 shows the acquired spectrum.

The signals along with the time at which they were acquired are saved in .csv format which is compatible with the SPECAIR program that is used to fit the spectrum's curve and extract temperature information from it. The spectrum for a stable microplasma discharge at a pressure of 30 psia is shown below. The current and voltage are held constant at 0.5 mA and 1.3 KV. Care is taken to prevent saturation of the PMT output above 5 V to prevent loss of information at the upper limit on the NI card module.
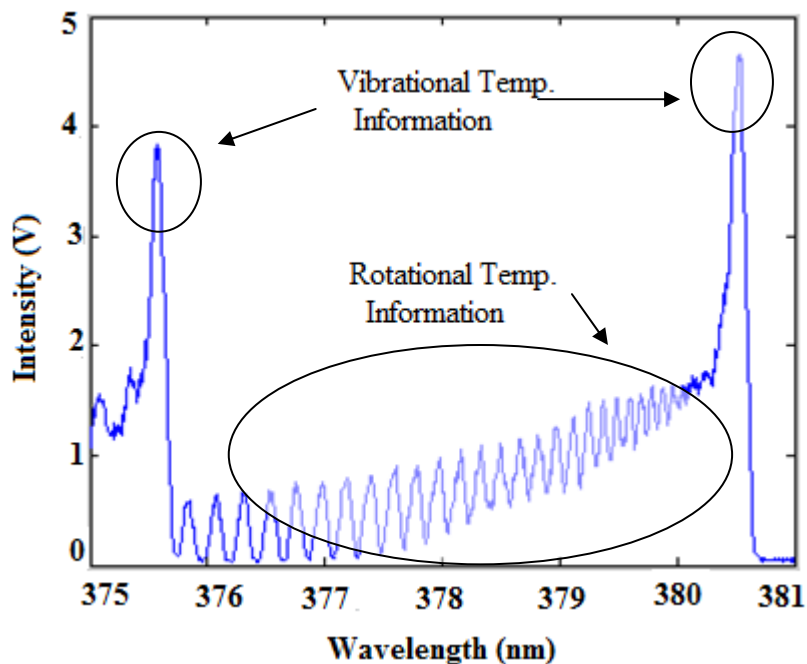
**Figure 29.** Spectrum acquired using photo multiplier tube

4.3.2.2. ICCD camera acquired spectra

The exposure time on the ICCD was set to 100 micro seconds with the MCP gain voltage set to its maximum value of 1000 along maximum digital gain settings.

For the ICCD camera, the spectrometers diffraction grating was set at 378 nm using the Lab view GPIB interface. This enabled to ICCD to capture the span from 375 nm to 381 nm in a single shot at a resolution of 0.004 nm /pixel in this wavelength region. Figure 30 shows the image captured by the ICCD camera. The raw data for every pixel in the 32 bit resolution provided by the camera is stored in binary format. This enables us to reopen the image in the same software or open the file in MATLAB. Figure 31 shows the spectra acquired by the ICCD camera after being processed in MATLAB.
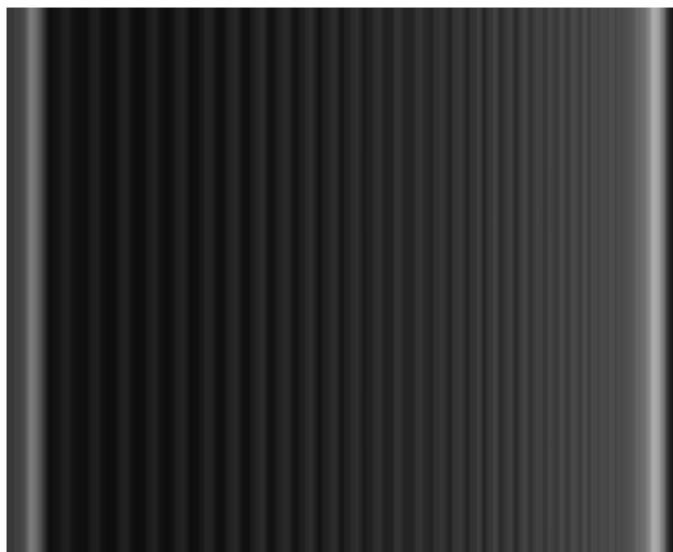
**Figure 30.** ICCD camera acquired spectra at 378.5 nm
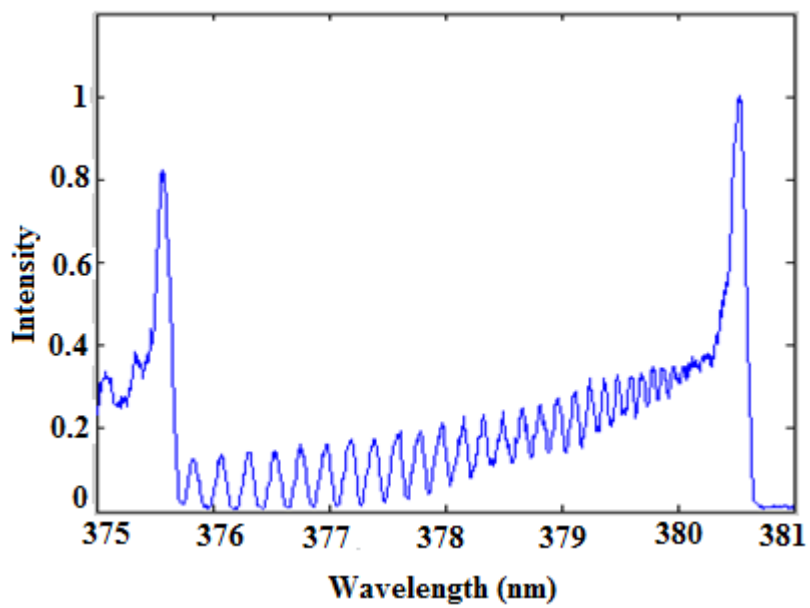
Figure 31. Spectrum captured by the ICCD camera and plotted in MATLAB

The Y-scale is different in the two plots in figures 29 and 31. For the PMT, the y scale has an upper limit of 5 V, while for the ICCD the upper limit would represent the 32 bit resolution of the camera and hence could go up to 2^{32}.

A code is developed in MATLAB using the file functions along with some wavelength calibration data to plot the spectrum from the obtained image and save a .csv file compatible with SPECAIR which fits the obtained spectrum with the temperature measurement model discussed in section 3.

4.3.3. SPECAIR fits

One must point MATLAB to C:\Specair\radiation\results\GUI where the RunSpecair.m file is located. Figure 32 shows the interface SPECAIR as it attempts to fit the data.
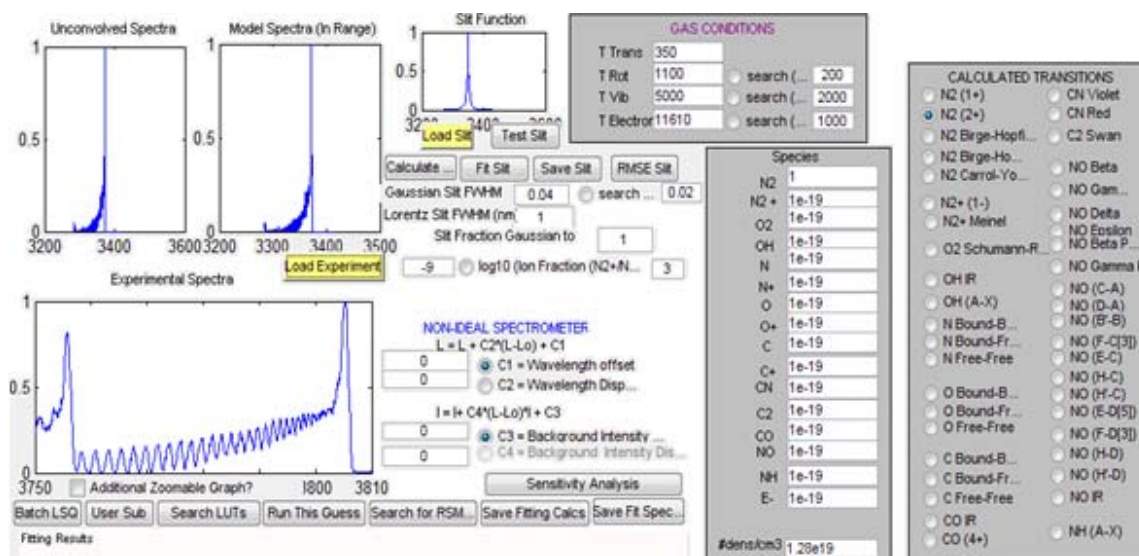
Figure 32. SPECAIR attempts to fit the loaded spectrum

The SPECAIR program is run and the appropriate spectrum file is loaded into it. The program is a 6 parameter fitting function superposed onto the basic SPECAIR model for the nitrogen spectrum in this wavelength region. The details of the fitting are mentioned in section 3. Reference material can be found in literature [56, 61].

The rotational temperature T_{rot}, vibrational temperature T_{vib} and the Full Width half maximum FWHM are the primary parameters of interest to us. All these are adjusted by the MATLAB code through a long series of iterations to minimize the root mean squared error (RMSE).The fitting results for all the parameters are saved again in .csv format. Figure 33 displays the normalized fitting results.
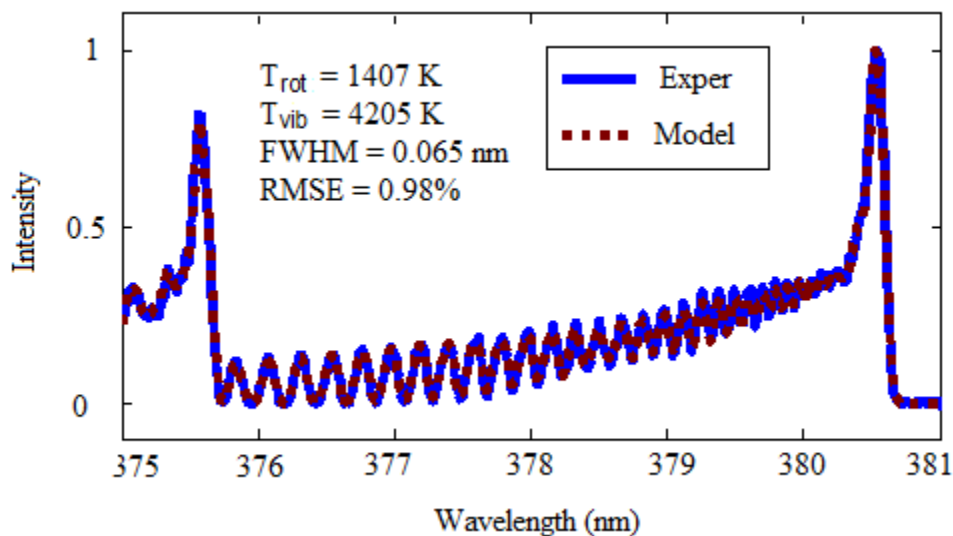
Figure 33. SPECAIR fit results

Thus, taking into account the basic learning's and trends observed in this section, further experiments are carried out as per the procedures mentioned here, and the results are summarized in the next section.

5. FINAL EXPERIMENTS AND RESULTS

5.1.   Experiments with helium

Experiments were initially carried out with helium. The discharge size of the microplasma was measured and its variation with change in discharge current and pressure was studied. Current densities of the microplasma were calculated from the current and discharge area data available. There were some stability issues encountered for the microplasma discharge in helium. These are explained in section 5.2.3.

5.1.1.   Variation of discharge size with current

Figure 34 shows the set-up for the helium experiments. Pressure is set at 50 psia.
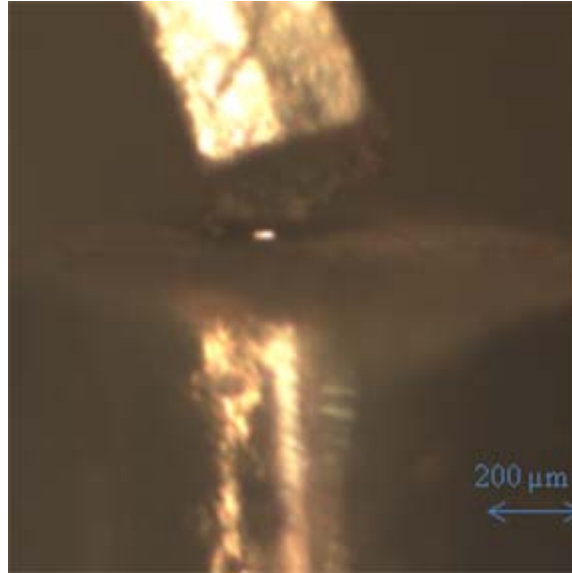
Figure 34. Electrode set-up for helium experiments

The current was varied from 1 mA to 0.1 mA with the gap set at 50 μm. The images were processed using the Analyze Image size code.
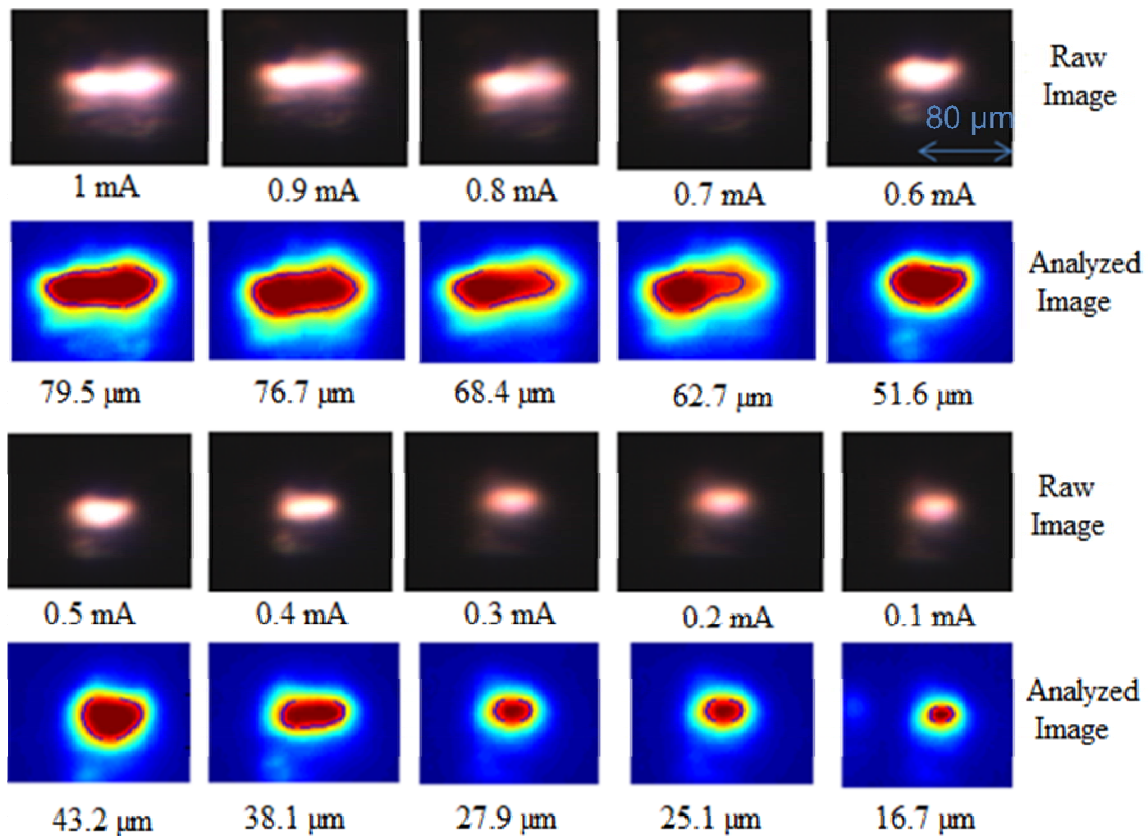
Figure 35. Captured images and discharge size measurements in helium.

Raw and analyzed images, 50 psia; 50 μm gap; R = 2.1 MΩ

Thus as expected from the preliminary experiments in section 4, the discharge size goes on decreasing with decrease in the discharge current. Figure 35 shows the variation in size observed. A microplasma discharge 16.7 μm in size is obtained with the current at 0.1mA for helium at 50 psia and for a 50 μm gap.

5.1.2. Variation of discharge size with pressure

As per the procedures discussed in section 4, the study of the discharge size with variation in pressure had to be carried out such that the discharge current is constant. It was observed that it is extremely difficult to maintain the stability of the microplasma discharge in helium at higher pressure as well as maintain a low discharge current. In fact with a gap of 250 μm between the electrodes, the microplasma could only be stabilized with high discharge currents on the order of 3 mA at conditions of high pressure around 90 to 100 psi.

Thus by setting the discharge current to be constant at 3 mA where the discharge was initially tested to be stable at 100 psi, pressure was increased from 15 psi to 100 psi. Figure 36 the variation in discharge size with change in pressure from 15 to 52.5 psi.
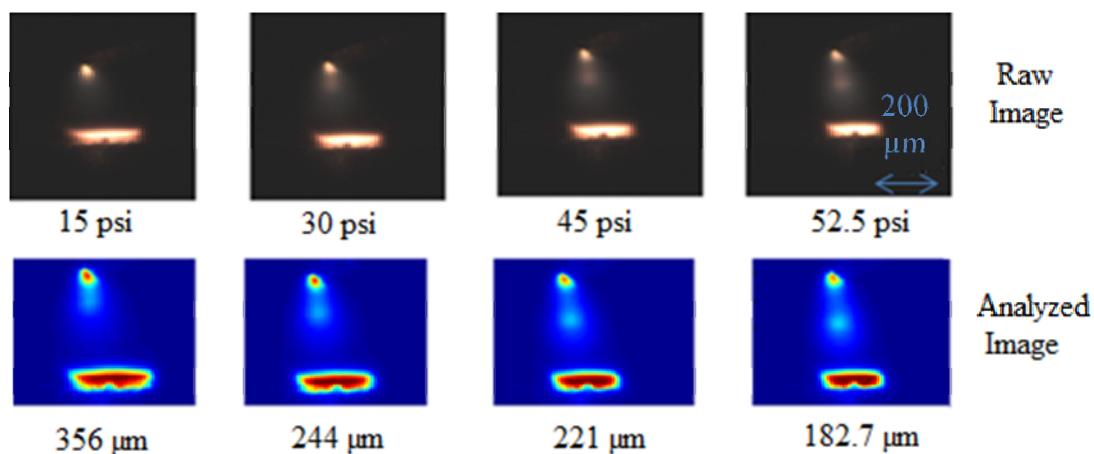
Figure 36. Variation of discharge size with pressure in helium 15 - 52.5 psi.

Raw and analyzed images, Current = 3 mA, 250 μm gap, R = 2.1 MΩ

With further increase in pressure, the microplasma discharge loses its stability. We can clearly observe the decrease in discharge size with increase in pressure. Figure 37 shows the variation from 60 psi to 100 psi. Discharge sizes are larger due to the greater values of discharge current required for sustaining the microplasma at higher pressures.
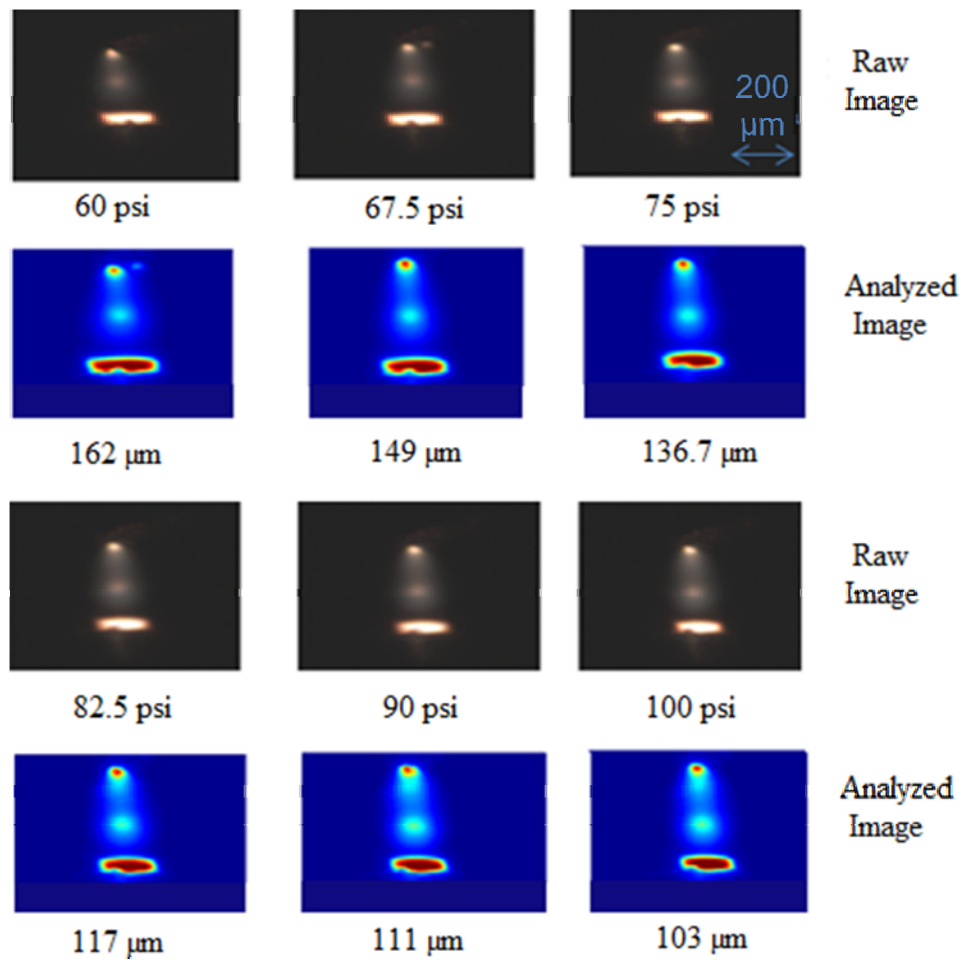
Figure 37. Variation of discharge size with pressure in helium pressure 60 - 100 psi. Raw and analyzed images, Current = 3 mA, 250 μm gap, R = 2.1 MΩ

5.2.   Analysis of helium results

The microplasma is characterized in terms of the variation of its discharge size with discharge current and pressure.

5.2.1.   Variation in discharge current

Table 3 summarizes the experiment for variation in discharge size with current.

Discharge voltage is calculate as $V_d = V_{ap} - IR$ where $R = R_b + R_i$

Table 3. Variation of microplasma size with discharge current in helium.

Current = 3 mA, 250 µm gap, R = 2.1 MΩ

| Pressure (psia)	Discharge Current I (mA)	Applied Voltage V_{ap} (KV)	Discharge Voltage V_d (V)	Discharge Size (µm)
50	1	2.360	260	79.5
50	0.9	2.133	243	76.7
50	0.8	1.897	217	68.4
50	0.7	1.691	221	62.7
50	0.6	1.489	229	51.6
50	0.5	1.271	221	43.2
50	0.4	1.078	238	38.1
50	0.3	0.859	229	27.9
50	0.2	0.615	195	25.1
50	0.1	0.403	193	16.7

The discharge area is approximated to be a circle of the diameter equal to the discharge size measured. Current density is calculated in units of A /cm^2 by dividing the current by the discharge area. The electron density [1, 15] is calculated using the formula specified in equation 2 in section 2 using the drift velocity $V_{drift} = 300$ m/s.

Figure 38 shows the variation in discharge size with current. The discharge size increases with increase in current as expected. Figure 39 shows the current density variation. Figure 40 shows the variation in discharge voltage. Figure 41 shows the electron density variation. The current density, the electron density as well as the discharge voltage remain almost constant with current variation as expected for a normal glow discharge and agree with results in the literature [2, 15] and for later operation.
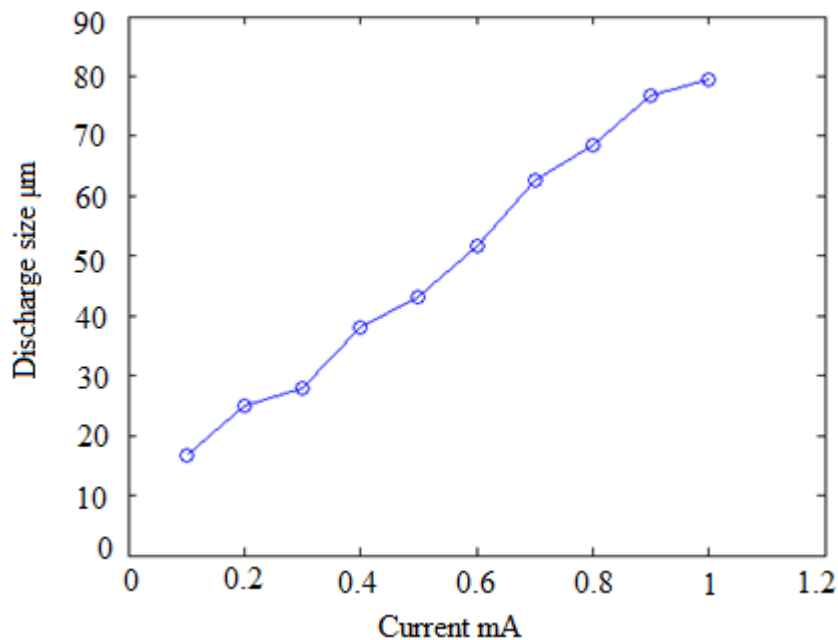
Figure 38. Variation of discharge size with current in helium.

Constant pressure 50 psi; Current = 3 mA, 250 μm gap, R = 2.1 MΩ
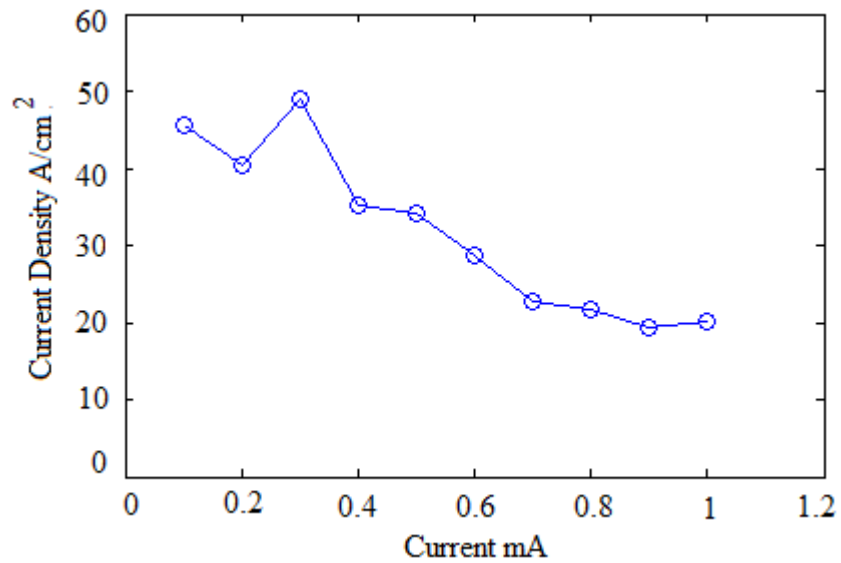
Figure 39. Variation of current density with current in helium.

Constant pressure 50 psi; Current = 3 mA, 250 μm gap, R = 2.1 MΩ
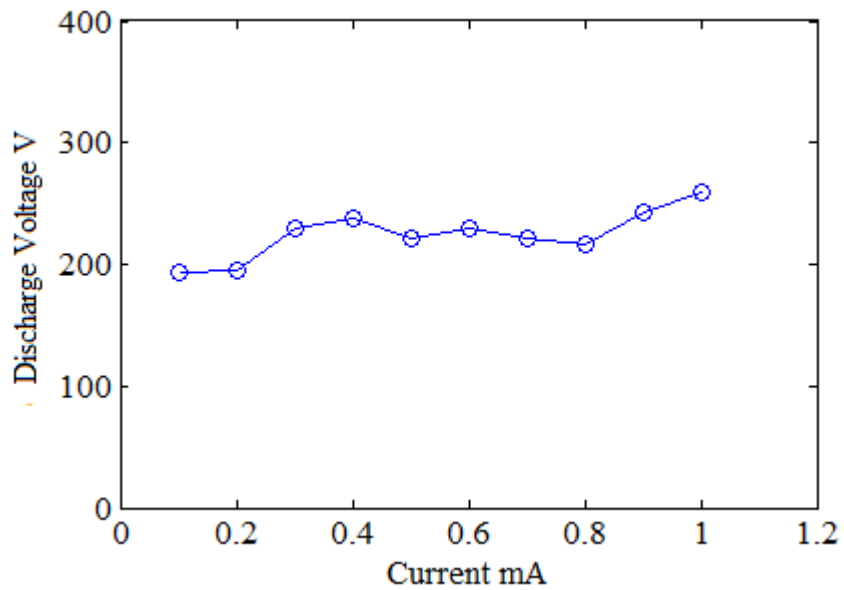

Figure 40. Variation of discharge voltage with current in helium.

Constant pressure 50 psi; Current = 3 mA, 250 μm gap, R = 2.1 MΩ
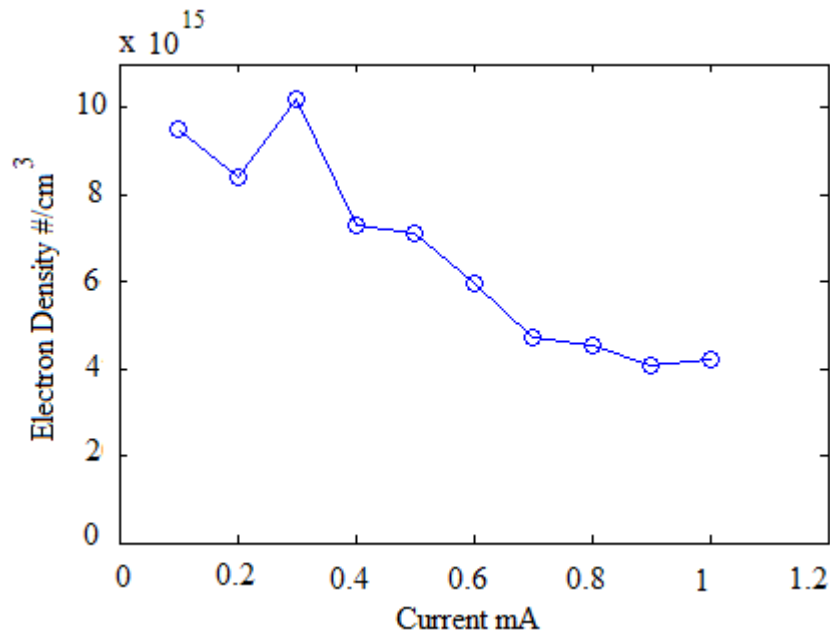
Figure 41. Variation of electron density with current in helium.

Constant pressure 50 psi; Current = 3 mA, 250 μm gap, R = 2.1 MΩ

V_{drift} = 300 m/s

5.2.2. Variation in pressure

There is a stability issue with the microplasma discharges in helium at higher pressures. The microplasma does not remain in a stable normal glow discharge mode at higher pressures and tends to transition towards the arc region.

The pressure is varied from 15 psia to 100 psia. The gap is set at 250 μm. The discharge current is held constant at 3 mA.

Discharge voltage is calculate as $V_d = V_{ap} - IR$ where $R = R_b + R_i$

R_b = 2 MΩ and R_i = 100 KΩ

Table 4 summarizes the experiment for the variation in discharge size with change in pressure for helium.

Table 4. Variation of microplasma size with variation in helium pressure.

3 mA current, 250 µm gap, R = 2.1 MΩ

Pressure (psia)	Discharge Current I (mA)	Applied Voltage V_{ap} (KV)	Discharge Voltage V_d (V)	Discharge Size (µm)
15	3	7.153	853	356.6
30	3	7.153	853	244.6
45	3	7.158	858	220.8
52.5	3	7.154	854	182.7
60	3	7.162	862	161.8
67.5	3	7.165	865	149.2
75	3	7.166	866	136.7
82.5	3	7.172	872	117.1
90	3	7.172	872	111.6
100	3	7.177	877	103.2

The electron density [1, 15] is calculated using the formula specified in equation 2 in section 2 using the drift velocity V_{drift} = 300 m/s. Normalized current density is obtained by dividing the current density by the square of the pressure expressed in Torr. The normalized current density is expressed in units of $\mu A /cm^2 * Torr^2$.

Figure 42 shows the variation of discharge size with pressure in helium. The trend of decrease in discharge size with decrease in current and increase in pressure is validated in Figure 42. The smallest discharge obtained is 16.7 μm in size at 50 psi with 0.1 mA discharge current.

Figure 43 shows the variation of current density with pressure in helium. The current density in A/cm^2 increases with increases in pressure. Figure 44 shows the variation of electron density with pressure in helium. The electron number density shows a proportional trend to the current density. Electron densities of the order of 7.5 x 10^{15} are attained at higher pressures. Figure 45 shows the variation of normalized current density with pressure in helium. The normalized current density is almost constant and close to the reference value of 2 μA /cm^2*Torr^2 given in literature [1]. Figure 46 shows the variation of discharge voltage with pressure in helium.

The current density for helium is however much lower than the corresponding value of 400 μA /cm^2*Torr^2 for nitrogen [1]. Nitrogen also is much cheaper, industrially widely used and easier to break down as compared to helium. Nitrogen is hence a better option as a processing gas from an industrial processing technology standpoint. Further experiments are carried out using nitrogen as the processing gas.
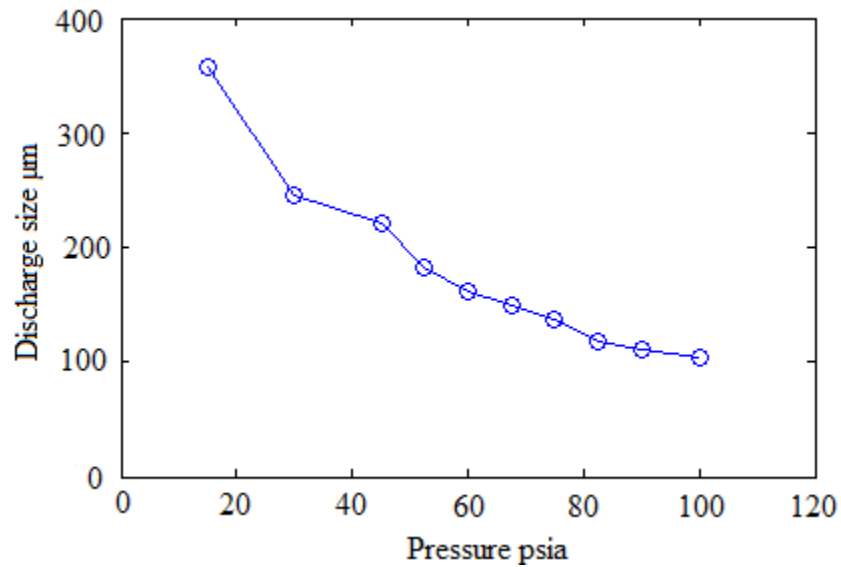
Figure 42. Variation of discharge size with pressure in helium.

3 mA current, 250 μm gap, R = 2.1 MΩ
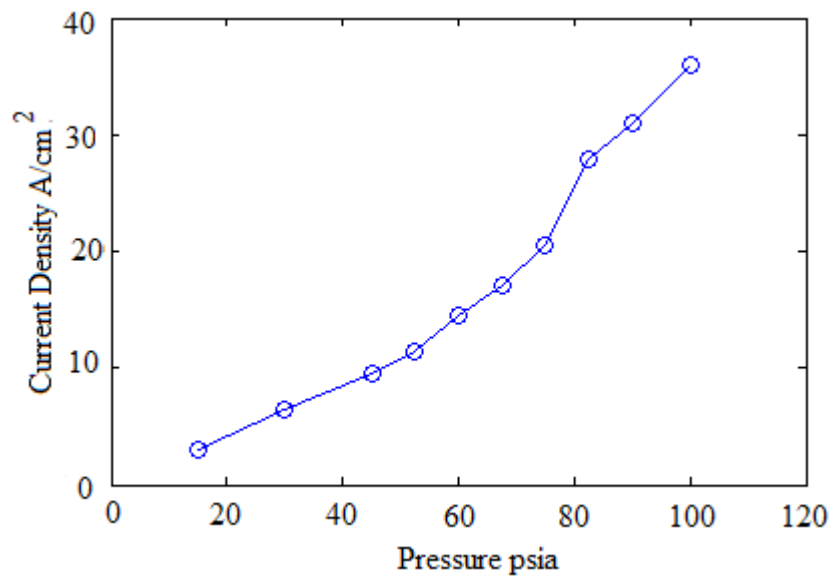
Figure 43. Variation of current density with pressure in helium.

3 mA current, 250 μm gap, R = 2.1 MΩ
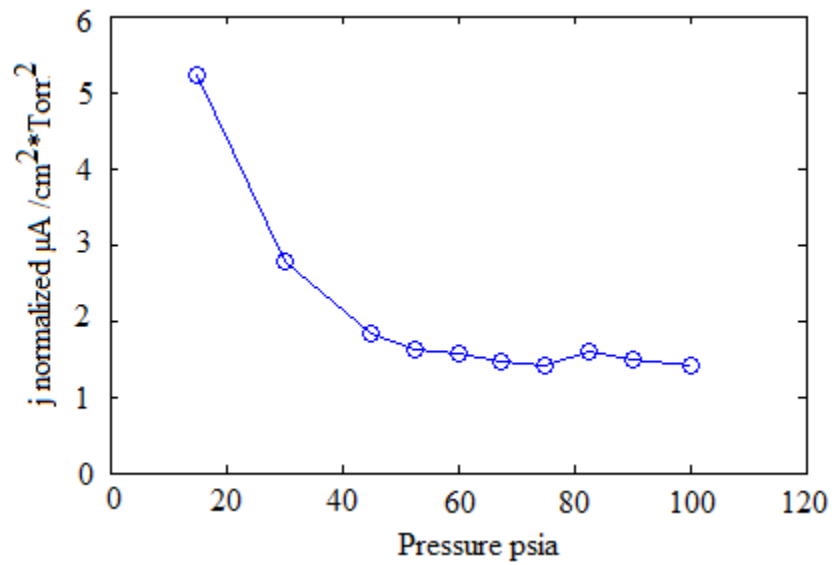
**Figure 44.** Variation of normalized current density with pressure in helium.

3 mA current, 250 μm gap, R = 2.1 MΩ
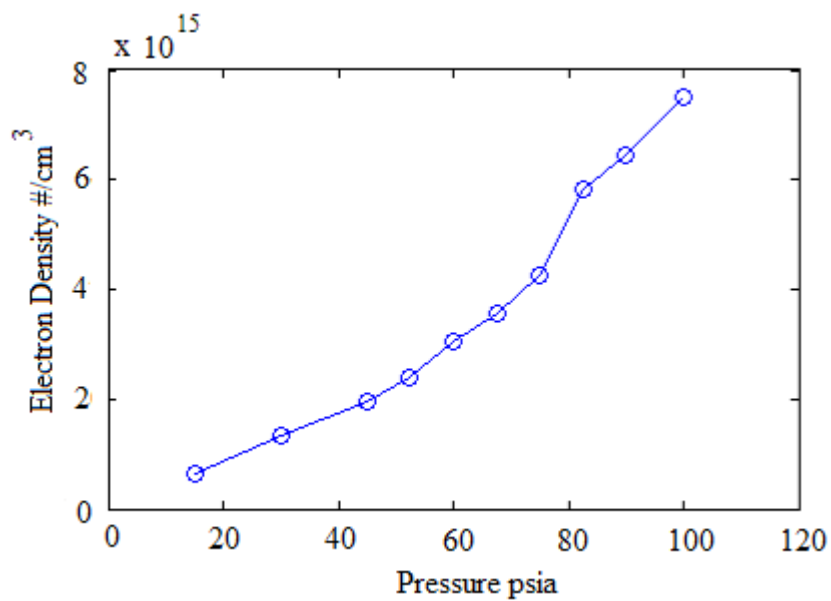
Figure 45. Variation of electron number density with pressure in helium.

3 mA current, 250 μm gap, R = 2.1 MΩ; V_{drift} = 300 m/s
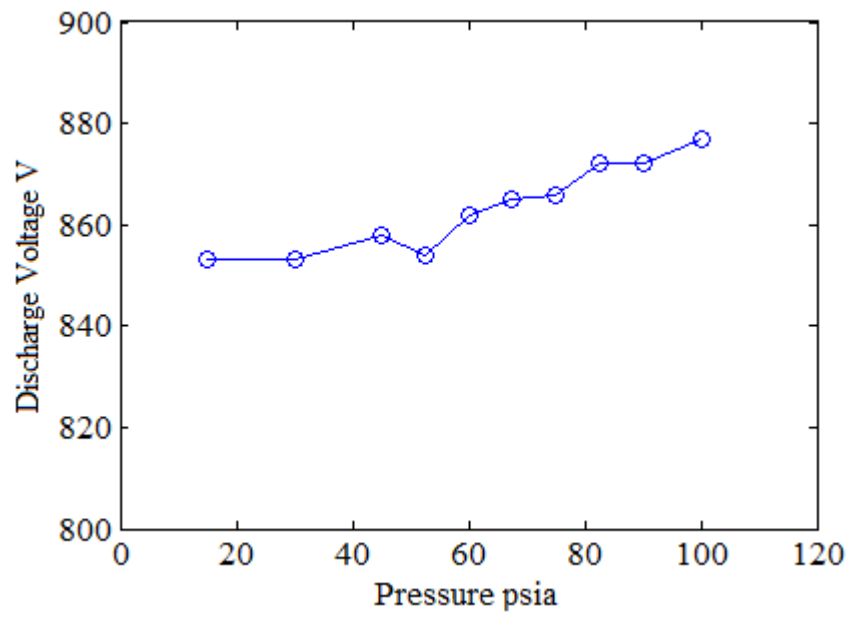
Figure 46. Variation of discharge voltage with pressure in helium.

3 mA current, 250 µm gap, R = 2.1 MΩ

5.3.   Experiments with nitrogen

Several advantages are available when nitrogen is used instead of helium like below.

1.   Enhanced Stability of the microplasma discharge at higher pressures

2.   Higher current densities, higher energy densities and smaller discharge sizes [1].

3.   Ability to make temperature measurements by OES [56, 61].

4.   Reduced power requirements and more energy efficient discharge in nitrogen.

5.   Much less expensive than helium and already widely used in the industry.

With these advantages in mind, experiments hence forth use nitrogen as the processing gas. Experiments are conducted in nitrogen similar to the helium experiments in which the effects of variation in pressure on the discharge size of the microplasma are studied.

It was now already evident that the microplasma discharge size decreases with decrease in discharge current. Hence the discharge current was kept constant and as low as possible while ensuring stability of the discharge at higher operating pressures.

The mass flow controller in the experimental set-up is hence set to loop on pressure with nitrogen selected as the carrier gas. Experiments were started off with validating the stability of the microplasma discharge in nitrogen at higher pressures along with validating the trend of decrease in discharge size with increasing pressure.

Current density calculations were made from the current and discharge size data available from the readings. These were to be compared to the reference value of 400 µA /cm^2*Torr^2 [1] for nitrogen using a stainless steel cathode.

5.3.1. Variation of discharge size with pressure

The experiments were carried out at a constant discharge current of 1 mA. Figure 47 shows the set-up in place. The pressure was varied 15 psia to 75 psi with the gap set to 150 µm. The Analyze Image Sizes code was used to calculate the size of the discharge.
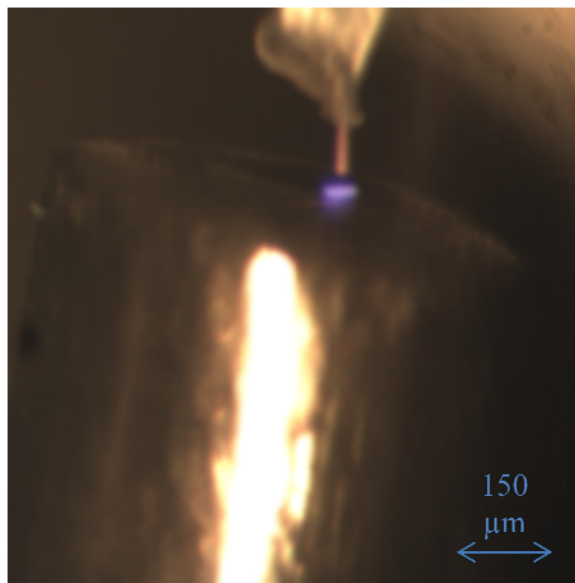
Figure 47. Electrode set-up for experiments in nitrogen
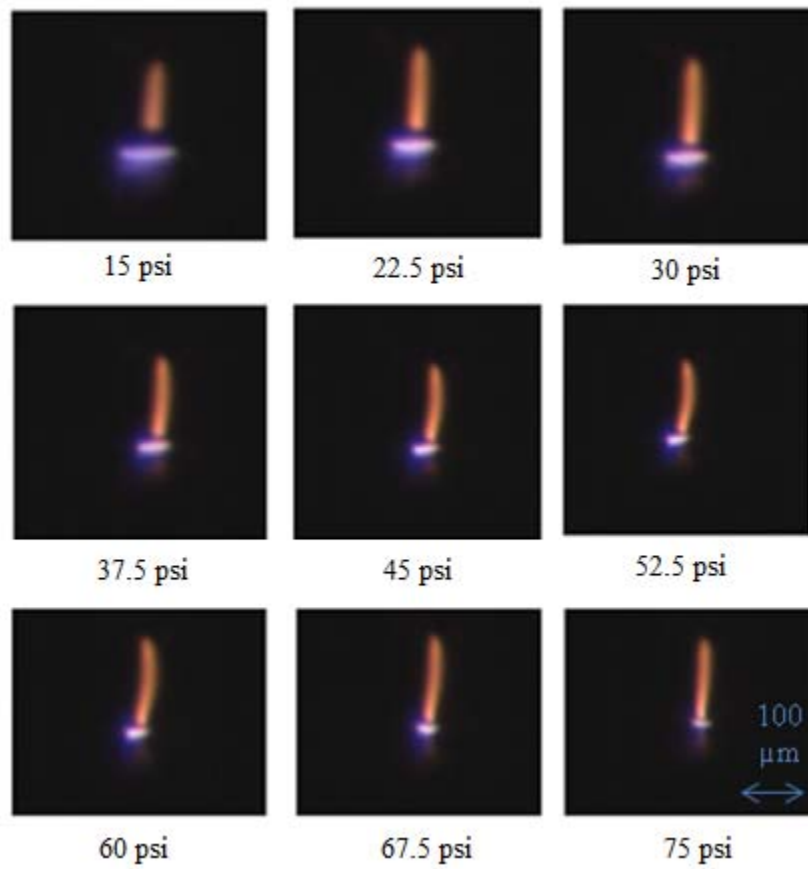
Figure 48. Captured images with variation in helium pressure 15-75 psi.

Raw images, Current = 1 mA, Discharge gap = 150 μm, R = 2.1 MΩ

5.4.   Analysis of nitrogen results

It was found that the microplasma discharge does not encounter the instability problem in nitrogen as in helium. The discharge size decreased with increase in the pressure of the nitrogen gas in the plasma pressure chamber. Figure 48 shows the variation in discharge size with pressure in nitrogen. Table 5 summarizes the experiment results.

Table 5. Variation of microplasma size with pressure variation in nitrogen.

Current = 1 mA, Discharge gap = 150 µm, R= 2.1 MΩ

| Pressure (psia)	Discharge Current I (mA)	Applied Voltage V_{ap} (KV)	Discharge Voltage V_d (V)	Discharge Size (µm)
15	1	2.522	422	86.7
22.5	1	2.526	426	63.6
30	1	2.545	445	62.1
37.5	1	2.602	502	54.9
45	1	2.614	514	43.3
52.5	1	2.615	515	37.6
60	1	2.647	547	31.8
67.5	1	2.657	557	30.3
75	1	2.675	575	26

Current density was calculated by dividing the constant discharge current of 1 mA by the discharge area. The discharge area was approximated to be a circle of the diameter equal to the discharge size measured by the Analyze Image Sizes code. Electron density and normalized current density calculations were done similarly to the helium experiment using equation 2 in section 2 and normalizing the current density with the pressure expressed in Torr. The resulting graphs are analyzed and plotted next.

Figure 49 shows the variation of discharge size with pressure in nitrogen. The discharge width decreased with increase in pressure. A minimum discharge size of 26 μm was obtained for a pressure of 75 psi with the discharge current at 1 mA for a 150 μm gap.

Figure 50 shows the variation of current density with pressure in nitrogen. The current density goes on increasing with increase in pressure as expected. Figure 51 shows the variation of electron density with pressure in nitrogen. The electron densities obtained were extremely dense in the range of 10^{16} /cm^3 or 10^{22} /m^3. Such high electron densities translate into high energy densities for the microplasma discharge. This high energy density microplasma could thus find application in etching micron size features into stainless steel for use in the Semiconductor Industry or some other plasma processing technologies.

Figure 52 shows the variation of normalized current density with pressure in nitrogen. Figure 53 shows the variation of discharge voltage with pressure in nitrogen. The calculations for the normalized current density however yielded values lower than the expected reference value of 400 μA /cm^2*Torr^2 [1] for nitrogen using a stainless steel

cathode. It was surmised that the temperature of the plasma had an effect on the current density and hence the values for the normalized current density were off by a factor of almost 10 for the experimental data giving a lower than expected density. Due to the increase in the temperature of the plasma as it get more and more concentrated in a smaller area with the increasing pressure, the effective pressure in the pressure chamber would be different from the pressure regulated by the mass flow controller. Optical emission spectroscopic studies were pursued for the microplasma in nitrogen to approximate the plasma temperature and hence the effective pressure. The variation with pressure experiments were repeated at minimum discharge current, with simultaneously acquired OES to extract temperature data.
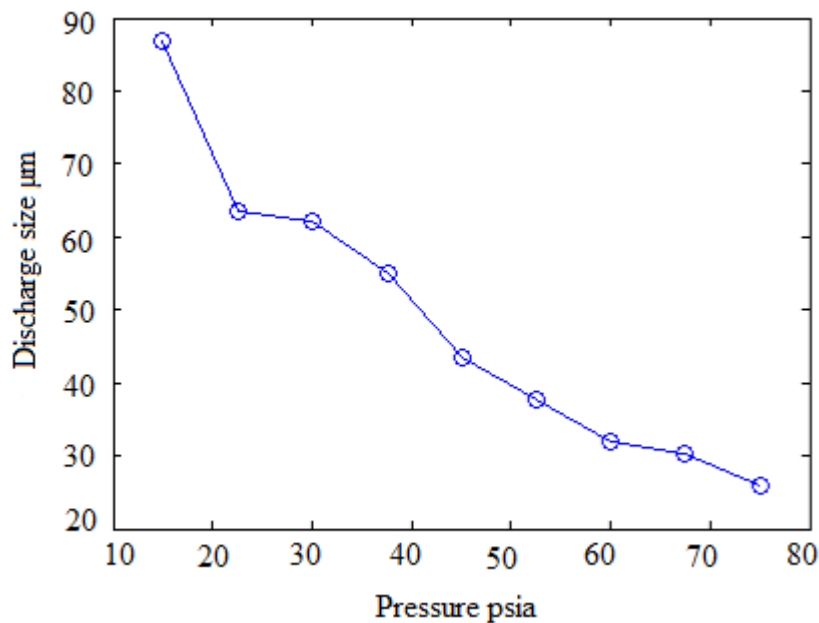
Figure 49. Variation of discharge size with pressure in nitrogen.

Current = 1 mA, Discharge gap = 150 µm, R = 2.1 MΩ
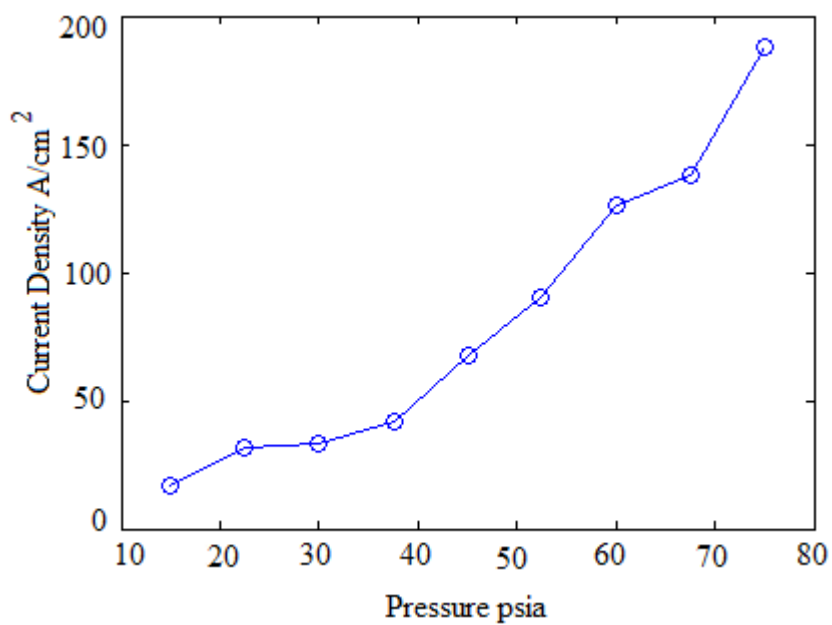
Figure 50. Variation of current density with pressure in nitrogen.

Current = 1 mA, Discharge gap = 150 μm, R = 2.1 MΩ
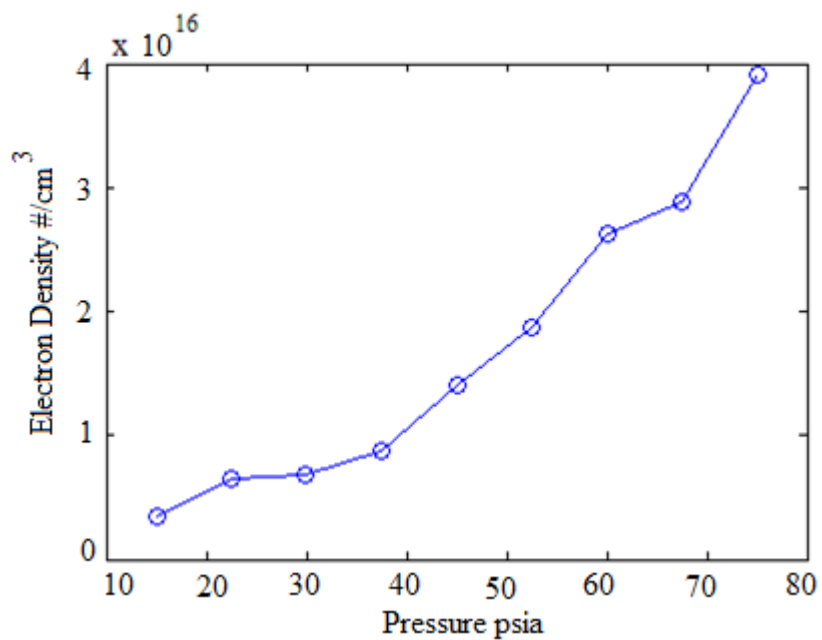
Figure 51. Variation of electron density with pressure in nitrogen.

Current = 1 mA, Discharge gap = 150 μm, R = 2.1 MΩ; V_{drift} = 300 m/s
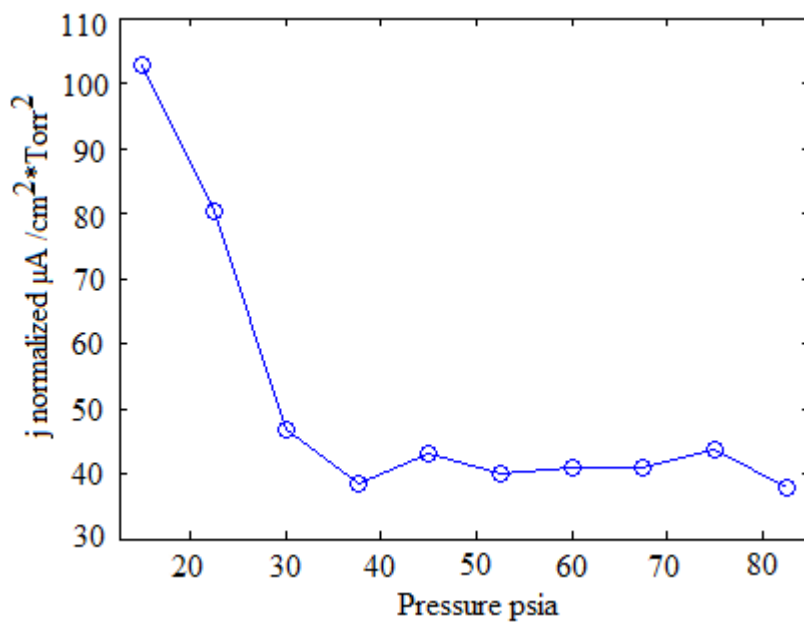
Figure 52. Variation of normalized current density with pressure in nitrogen.

Current = 1 mA, Discharge gap = 150 μm, R = 2.1 MΩ
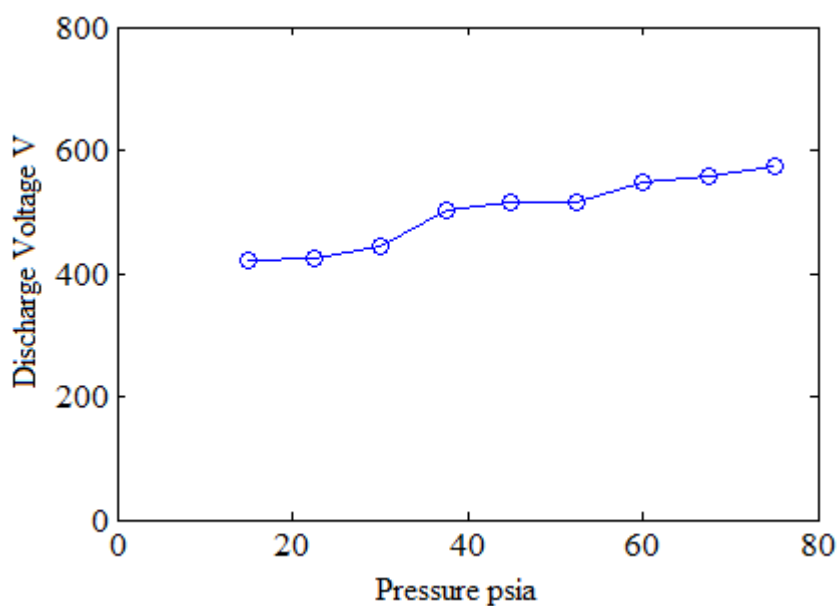
Figure 53. Variation of discharge voltage with pressure in nitrogen.

Current = 1 mA, Discharge gap = 150 μm, R = 2.1 MΩ

**5.5.   Experiments with nitrogen along with simultaneous spectroscopy**

The microplasma discharge was simultaneously imaged by microscopic visualization from one optical window and the light from the discharge was captured by OES through the other coaxial optical window installed in the new set-up of the pressure chamber.

The OES instrumentation set-up as described in section 4 is in place to acquire the spectrum of the microplasma discharge at each step of the pressure variation experiment in the 375 nm to 381 nm wavelength spans.

The experiments were carried out at a constant discharge current of 0.5 mA. Pressure was varied over a range of 15 psi to 240 psi to achieve a discharge size as small as possible. A series of images and spectra were recorded at regular pressure intervals which are processed then in MATLAB. Figure 54 shows the imaged microplasmas and OES spectra fits for 15-30 psi. Figure 55 shows the imaged microplasmas and OES spectra fits for 50 - 90 psi. Figure 56 shows the imaged microplasmas and OES spectra fits for 120-180 psi. Figure 57 shows the imaged microplasmas and OES spectra fits for 200 - 240 psi.

The discharge size and current density information were extracted from the captured images. The spectra taken by the ICCD camera were processed in MATLAB, saved in .csv format and loaded in the modified SPECAIR model for extracting temperature data from the intensity versus wavelength curve.

Taking the rotational temperature approximation put forth by the SPECAIR fit, the effective pressure was calculated. Normalized current densities were then calculated using the effective pressure due to the change in gas temperature.
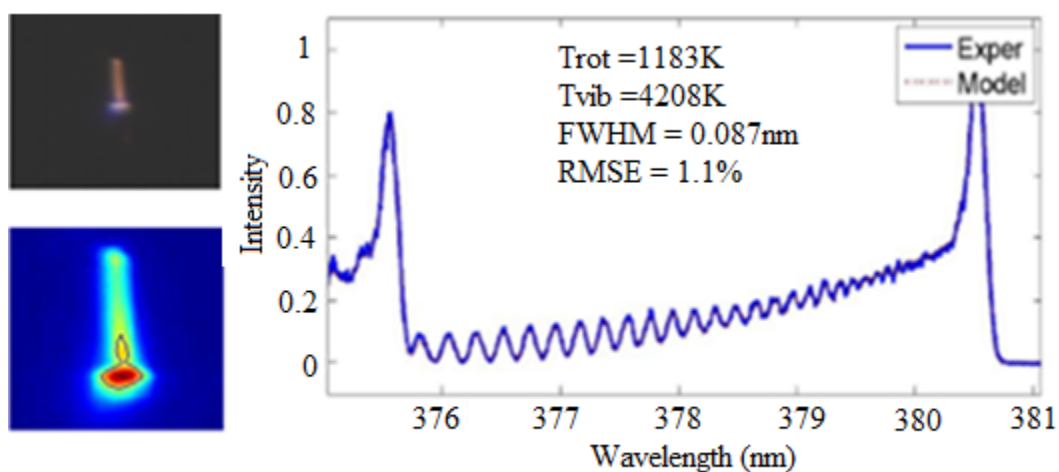
0.5 mA, 15 psi, 40.4 µm, Trot =1183 K, Tvib = 4208 K, RMSE =1.1%
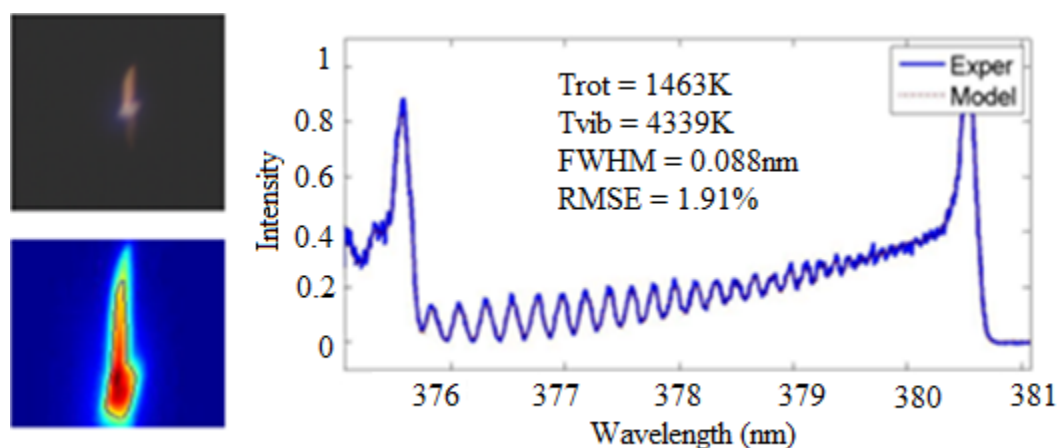
0.5 mA, 30 psi, 34.8 µm, Trot =1463 K, Tvib = 4339 K, RMSE =1.91%

Figure 54. OES and discharge size results, pressure 15-30 psi.

I = 0.5mA, R = 2.1 MΩ, d = 50 µm

0.5 mA, 50 psi, 33.4 μm, Trot =1652 K, Tvib = 4187 K, RMSE =1.03%

0.5 mA, 75 psi, 27.9 μm, Trot =2361 K, Tvib = 4061 K, RMSE =1.38%

0.5 mA, 90 psi, 21.6 μm, Trot =2682 K, Tvib = 3940 K, RMSE =1.47%
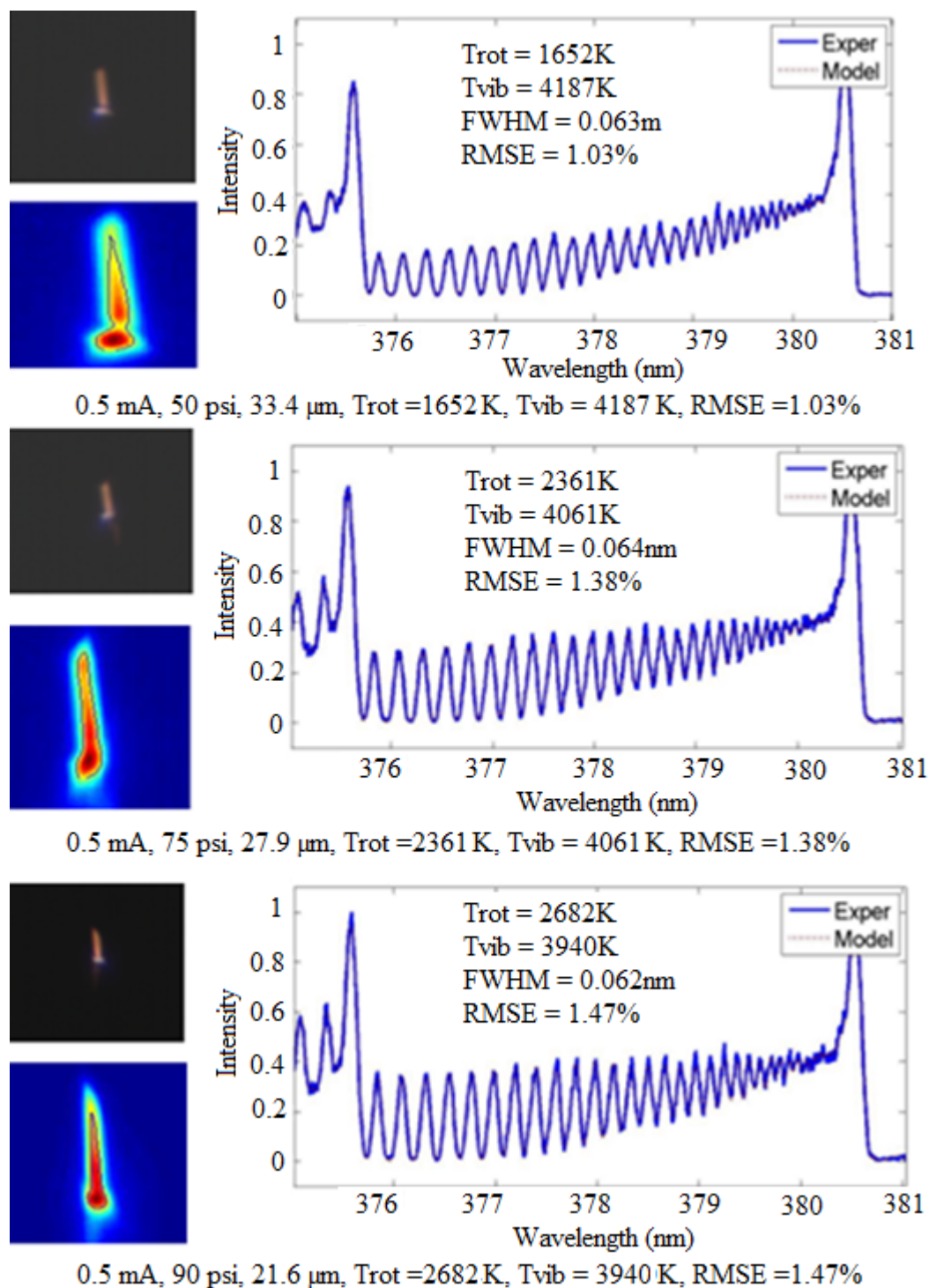
Figure 55. OES and discharge size results, pressure 50-90 psi

0.5 mA, 120 psi, 13 μm, Trot =2666 K, Tvib = 3156 K, RMSE =3.08%

0.5 mA, 150 psi, 11.56 K, Tvib = 3128 K, RMSE =3.48%

0.5 mA, 180 psi, 10.12 μm, Trot =2822 K, Tvib = 3185 K, RMSE =3.31%
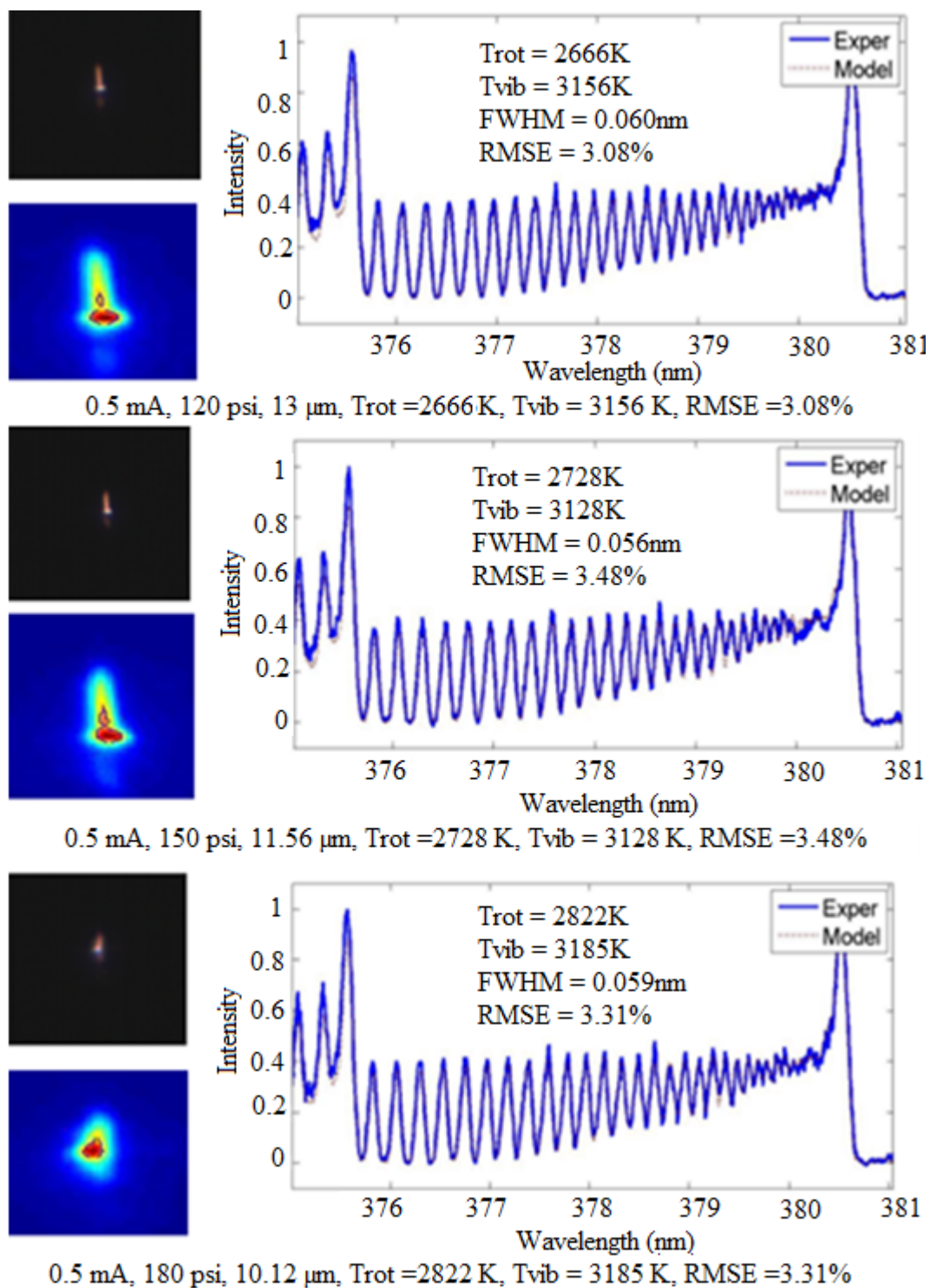
Figure 56. OES and discharge size results, pressure 120-180 psi
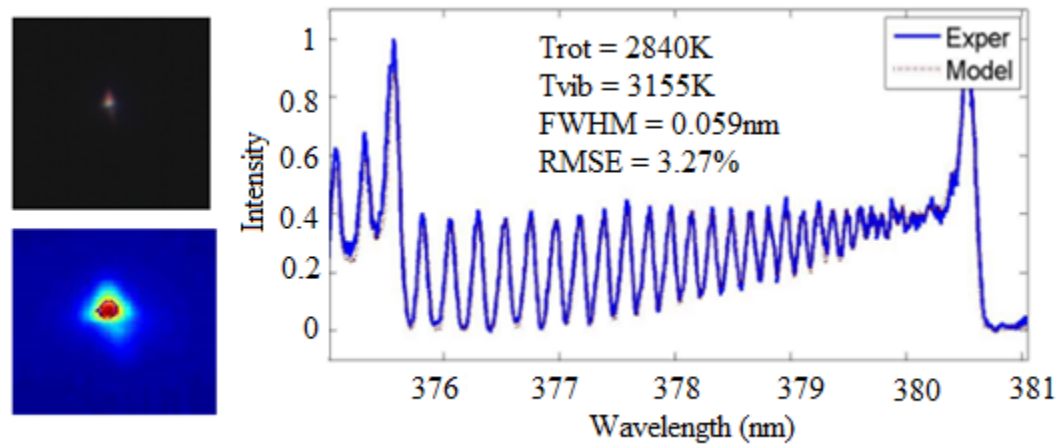
0.5 mA, 200 psi, 8.6 μm, Trot = 2840 K, Tvib = 3155 K, RMSE = 3.27%
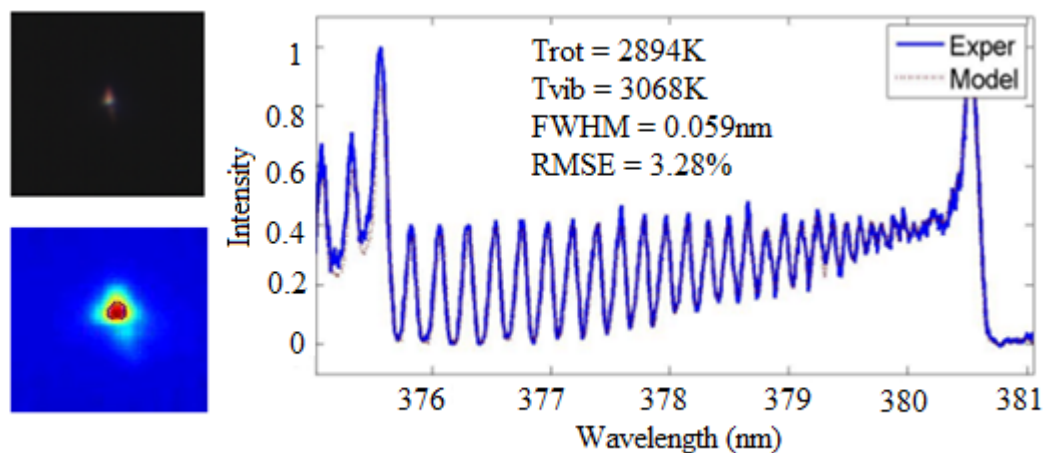
0.5 mA, 240 psi, 7 μm, Trot = 2849 K, Tvib = 3068 K, RMSE = 3.28%

Figure 57. OES and discharge size results, pressure 200-240 psi.

I = 0.5 mA, R = 2.1 MΩ, d = 50 μm

5.6. Optical emission spectroscopy results

The results of simultaneous microscopic visualization and optical emission spectroscopy of the microplasma discharge are presented in this section.

As stated in section 5.5, the pressure was varied over a range of 15 psi to 240 psi with the discharge gap set at 150 μm and the current held constant at 0.5 mA. The resistor ballast is 2 MΩ along with a 100 KΩ resistor inside the chamber. Table 6 summarizes the OES experiment results.

Table 6. Discharge size and temperature variation with nitrogen pressure.

Discharge current = 0.5 mA, R = 2.1 MΩ, d = 150 μm

Pressure (psia)	Discharge Voltage V_d (V)	Discharge Size (μm)	Rotational Temperature K	Vibrational Temperature K
15	312	40.45	1186	4208
30	324	34.87	1463	4339
50	327	33.47	1652	4187
75	332	27.89	2361	4061
90	334	21.86	2682	3940
120	322	13.07	2666	3156
150	323	11.56	2728	3128
180	325	10.12	2822	3185
200	325	8.68	2840	3155
240	324	7.23	2894	3068

Figure 58 shows the discharge size variation in the OES experiments. There was a decrease in the discharge size with increase in pressure with the discharge current kept constant at 0.5 mA as expected in accordance with the scaling laws [2, 15]. The smallest microplasma discharge of 7 μm was measured at 240 psi.

Figure 59 shows the rotational temperature variation in the OES experiments. The rotational temperature of the plasma also increased with increasing in pressure. Figure 60 shows the vibrational temperature variation in the OES experiments. The vibrational temperature on the other hand decreased with increase in pressure. The rotational temperature went from 1186 K to 2894 K over the 15 psi to 240 psi pressure range investigated. Vibrational temperature decreased to 3068K at 240 psi after remaining greater than 4000 K till 90 psi.

The increase in the rotational temperature and the decrease in the vibrational temperature result in a region where they become comparable to each other and within range of uncertainty of ±200 K for T_{rot} and ±500 K for T_{vib} in the fitting results. The increase in rotational temperature goes well with our effective pressure assumption and is discussed next in section 5.7.

Figure 61 shows the variation in the discharge voltage. Discharge voltage calculations are added to study a possible transition of the microplasma from normal glow mode into the arc region. A drop in discharge voltage would correspond to a transition from a glow mode of operation into the thermal arc region. No significant drop is measured in the discharge voltage in figure 61. The error bars are calculated to account for the

uncertainty in measurements of applied voltage and discharge current which are 0.1% and 1 % respectively.

The rotational and vibrational temperatures also converge towards each as seen in figures 59 and 60. A transition from non-equilibrium plasma to equilibrium plasma is thus encountered in the pressure region close to 100 psi where the temperatures become comparable to each other. Figure 62 shows the variation in the electron density with pressure. The electron density was calculated using equation 2 in section 2 assuming the thermal drift velocity at V_{drift} = 300 m/s and at V_{drift} = 1800 m/s thus considering both quasi neutral state as well as the sheath region.
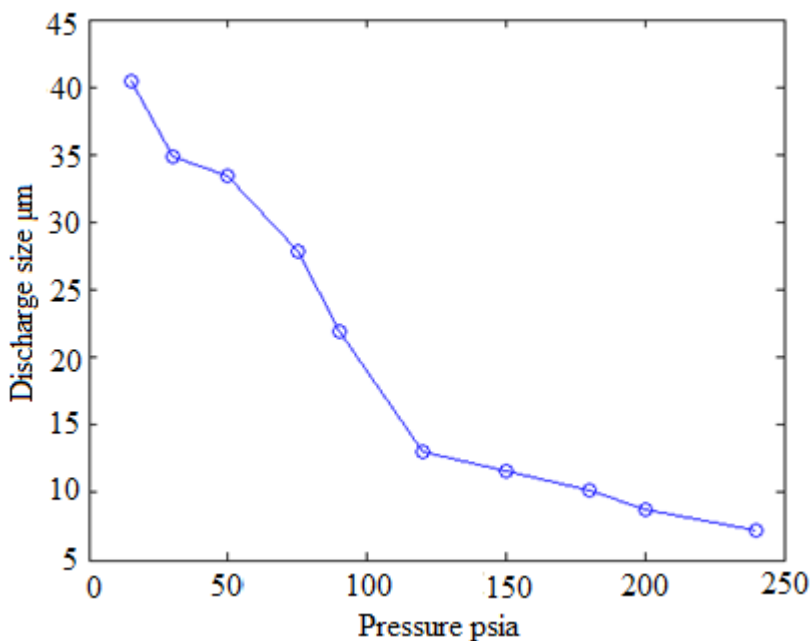
Figure 58. Discharge size variations with pressure in nitrogen.

Current = 0.5 mA, R = 2.1 MΩ, d = 150 μm
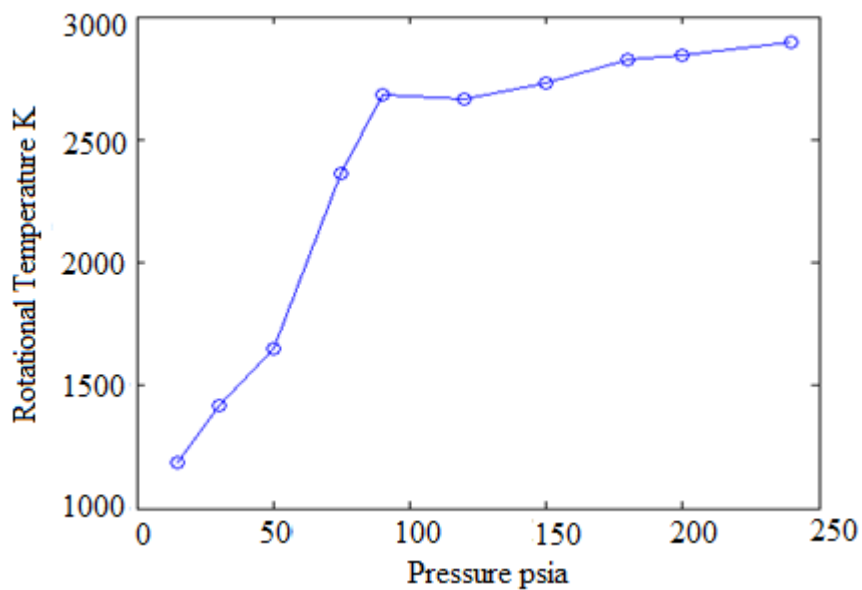
Figure 59. Rotational temperature variations with pressure in nitrogen.

Current = 0.5 mA, R = 2.1 MΩ, d = 150 μm
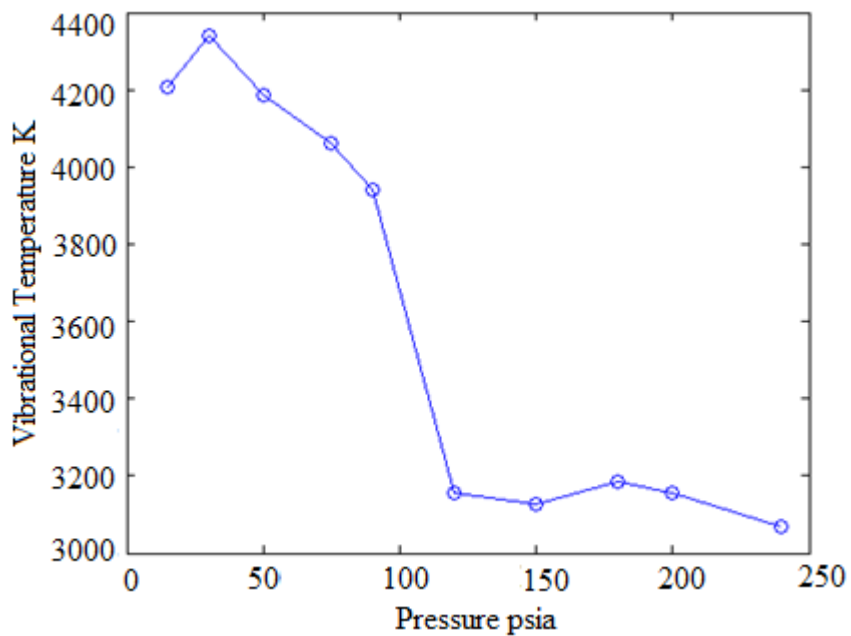
Figure 60. Vibrational temperature variations with pressure in nitrogen.

Current = 0.5 mA, R = 2.1 MΩ, d = 150 μm
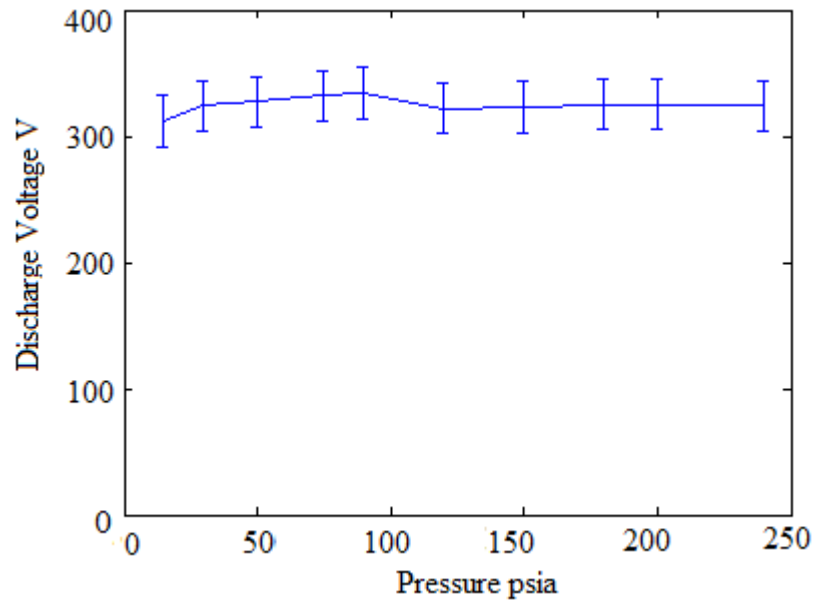
Figure 61. Discharge voltage variations with pressure in nitrogen.

Current = 0.5 mA, R = 2.1 MΩ, d = 150 μm
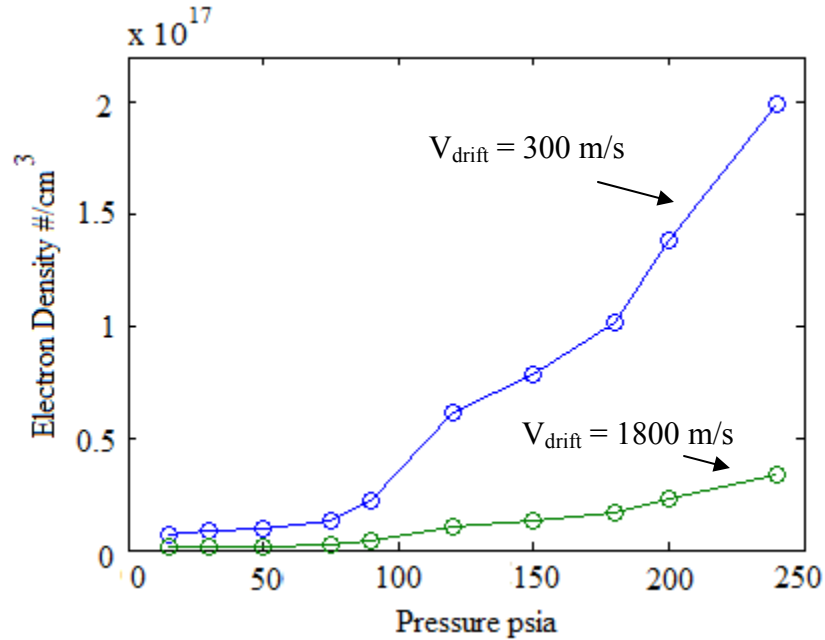
Figure 62. Electron density variations with pressure in nitrogen.

Current = 0.5 mA, R = 2.1 MΩ, d = 150 μm; V_{drift} = 300 m/s

5.7.   Effective pressure calculations and current density corrections

With increase in pressure in figure 58 we observed an increase in the rotational temperature and thus an increase in the temperature of the gas. This increase in gas temperature results in a change in pressure in the plasma region.

Inherently at the root level, collisional processes determine the parameters of the plasma. These collisional processes depend on the mean free path. The mean free path is a function of the number density n.

The plasma parameters are hence dependent on the electron number density n rather than pressure P. The effective pressure calculation takes this into account an effective pressure based on n scaling rather than p scaling.

The effective pressure is calculated based on n scaling using as discussed in section 2.3.2. Equation 9 gives us the reduced equation as per experimental conditions.

$$P \text{ effective} = P \text{experimental} * \frac{T \text{ reference}}{T \text{ experimental}}$$

$$P \text{ effective} = P * \frac{T(300K)}{Trot}$$

(9)

Equation 9. Effective pressure calculation

The effective pressure is thus lower than the pressure regulated in the pressure chamber. The effective pressure P_{eff} being in the denominator for the j/P^2 or the j/P_{eff}^2 scaling law results in increasing the current density.

The current density was normalized using the effective pressure. Figure 63 show the variation in the current density without the effective pressure contribution. Figure 64 shows the current density normalized with effective pressure correction. The normalized current densities after introducing the effective pressure correction were around the reference value of 400 μA /cm^2*Torr^2 [1] for nitrogen using a stainless steel cathode. The error bars are calculated to account for the uncertainties in the values of current, discharge size, pressure and temperature all of which are experimentally measured. The uncertainties are 2% for current, 3.5% for discharge size, 15% for pressure and 10% for temperature at 15 psi. On the other end of the experiment range, the uncertainties are 2% for current, 20% for discharge size, 1% for pressure and 10% for temperature.
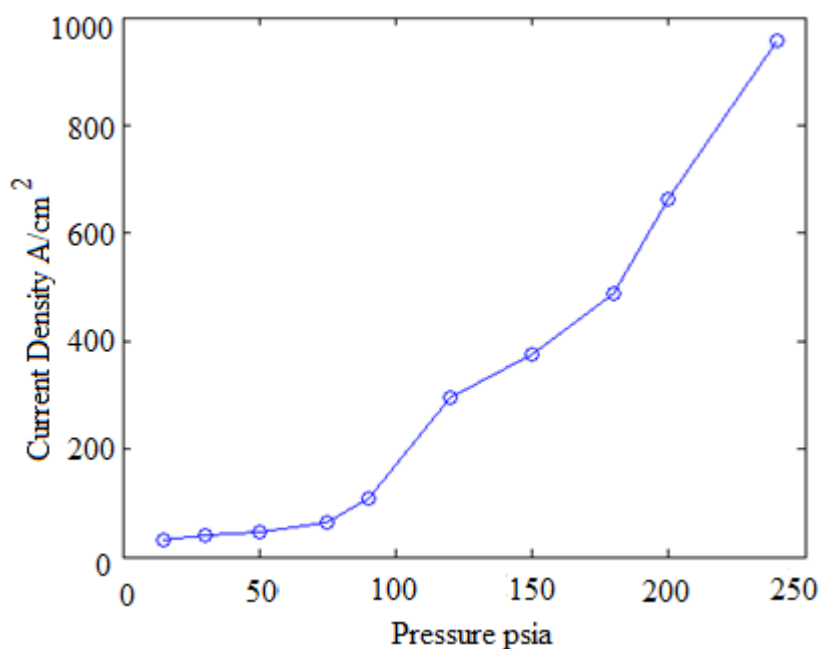
Figure 63. Current density variations in nitrogen without effective pressure.

Current = 0.5 mA, R = 2.1 MΩ, d = 150 μm
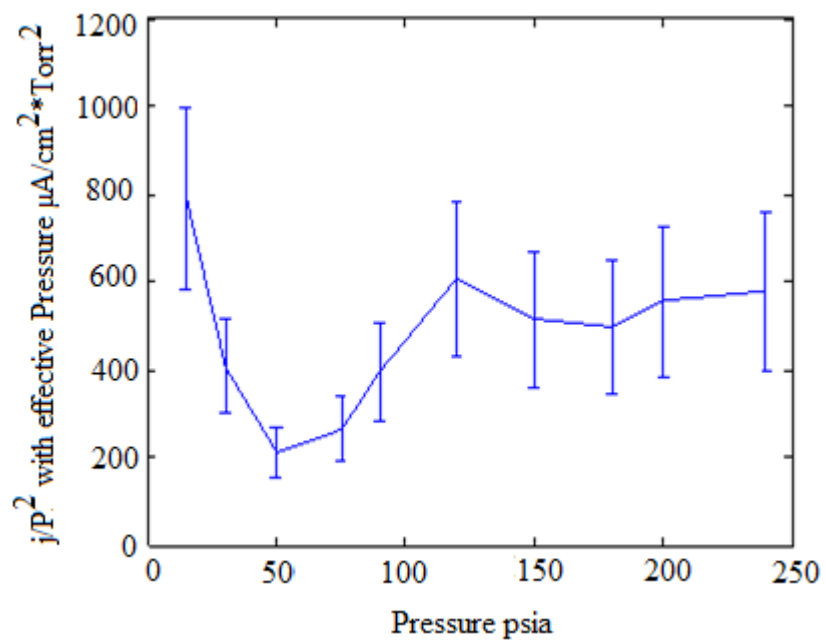
Figure 64. Normalized current density with effective pressure correction.

Current = 0.5 mA, R = 2.1 MΩ, d = 150 μm

6. CONCLUSIONS AND FUTURE WORK

6.1. Research objectives

The research work in this thesis was initiated with the following objectives in mind:

a) The thesis will focus on the parameters of microplasma discharge size and the energy density or particle density of the plasma. These features are important from the perspective of using the microplasma for plasma processing and direct write surface patterning applications. The variation of these parameters with pressure will be studied in depth with the goal of achieving minimum discharge sizes and maximum energy densities.

b) The thesis will also include optical emission spectroscopy (OES) as its plasma temperature diagnostic tool. The rotational and vibrational temperatures of the microplasma discharge will be estimated using a customized temperature model compared with experimentally acquired spectra from the microplasma system.

c) Through these temperature measurements, the thesis will attempt to study the transition of the microplasma from a non-thermal operation mode to a thermal operation regime. The temperature measurement results should provide more clarity with regards to the scaling laws at higher than atmospheric pressures and seek to investigate the limits of the scaling.

These objectives have been achieved as outlined in the following section.

6.2.   Conclusions

6.2.1. Discharge sizes attained

Discharges < 10 μm were achieved. Figure 65 shows the decrease in the discharge size
of the microplasma with increase in pressure. The smallest microplasma discharge size
of 7 μm was measured at 240 psi of nitrogen with the current held constant at 0.5 mA.
At atmospheric pressure the microplasma discharge was measured to be 40 μm in
dimension. With increase in pressure the discharge size continued to decrease.
Discharges after 180 psi were measured to be less than 10 μm in size. These
measurements are however subject to error due to the resolution limit of 1.4 μm /pixel in
the imaging measurements.
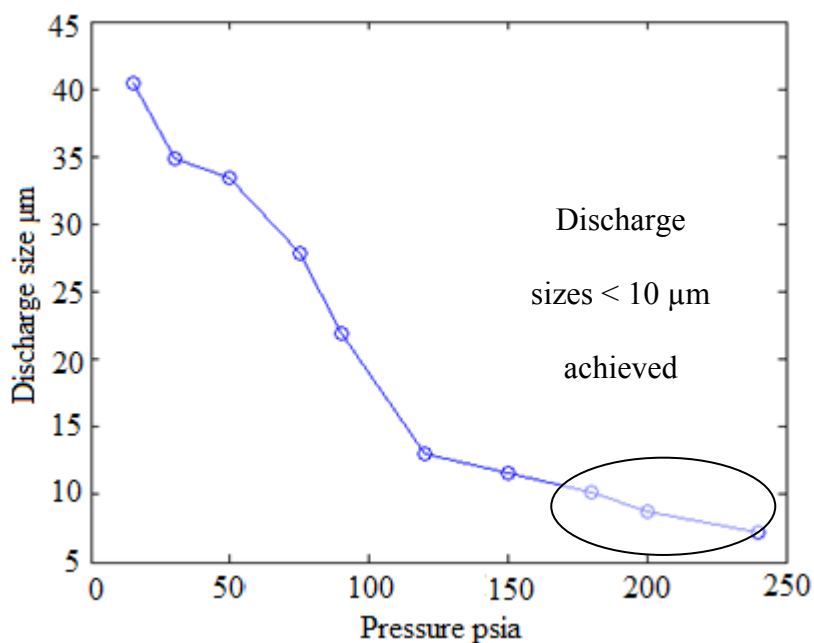
Figure 65. Discharge sizes less than 10 μm observed in nitrogen

6.2.2. OES temperature measurement results

While making the discharge size measurements using the microscopic visualization technique, light emission from the microplasma discharge was captured simultaneously by optical emission spectroscopy.

Rotational and vibrational temperature measurements were made from the emitted spectra by comparing the spectra with the modified SPECAIR model. A transition from a non-equilibrium glow discharge to equilibrium plasma is observed.

Figure 66 shows the variation in the rotational temperature T_{rot} and the vibrational temperature T_{vib}. It was observed that with increase in pressure, there was an increase in T_{rot} of the plasma while T_{vib} went on decreasing. After the initial upward sloping region in T_{rot}, the temperatures converged towards a saturation value almost equal to each other.

At pressure values greater than 100 psi, the rotational temperature and the vibrational temperature are measured to be extremely close to each other within a band of about 500K which is comparable to the uncertainty in the T_{vib} fitting results. This result points towards a transition of the plasma from a non-thermal non-equilibrium plasma to an equilibrium plasma with rotational and vibrational temperatures comparable to each other.
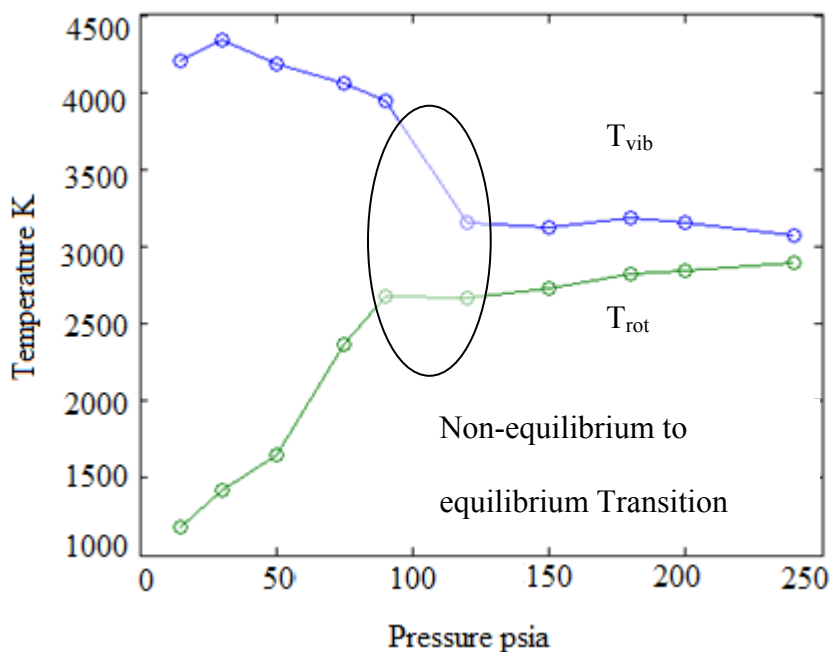
Figure 66. Rotational and vibrational temperatures and transition region

Vibrational excitation and vibrational relaxation are the two processes that determine the vibrational temperature [56]. Vibrational excitation is associated with electron impact (e-V) or the transfer of energy to neutral particles due to their collisions with charged electrons. Vibrational to translational (V-T) relaxation rate is associated with loss of energy due to the transfer of energy from the excited species to the ground state gas surrounding the plasma discharge. Relaxation also occurs due to collisions with the electrode surfaces.

Vibrational temperature measurement and its variation with discharge current and electrode spacing have been studied. The plasma discharge which is the heat source (excitation) has been approximated as a cylindrical control volume in order to perform a

heat balance for the system. Radial cooling over the curved surface area of this cylinder and axial cooling over the electrodes are the two major cooling mechanisms that contribute to the heat removal (relaxation) [56].

The discharge finds it difficult to maintain its non-equilibrium structure at these higher pressures at extremely compressed spatial dimensions. On the basis of these rates of excitation, V-T relaxation and relaxation due to collisions with the electrode the trends in figure 66 can are explained for the transition from a non-equilibrium to an equilibrium plasma discharge.

In the normal glow regime, the current density remains almost constant. The rate of excitation also remains constant. However with increase in gas temperature, the V-T relaxation rate undergoes an exponential rise as explained by the Landau Teller formula [68]. The decrease in T_{vib} hence coincides with an increase in T_{rot} and we see the two temperatures converge towards a saturation value in which the microplasma goes into being categorized as an equilibrium discharge. Figure 67 shows the variation in discharge voltage with pressure. We see that the discharge voltage remains almost constant which proves that the plasma does not transition from the glow mode. The discharge does not transition into an arc upon which a greater drop in voltage would have been observed as the means of electron emission at the cathode in such a transition to an arc goes from secondary electron emission to thermionic emission [12, 15].
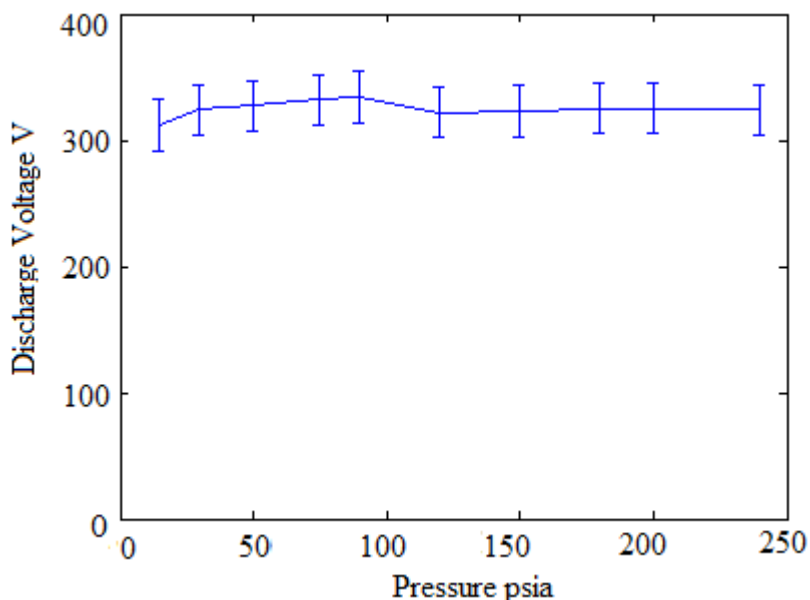
Figure 67. Constant discharge voltage with variation in nitrogen pressure

6.2.3. Effective pressure correction and scaling

The measured rotational or gas temperature values are used to calculate the effective pressure. Introducing the effective pressure correction the current densities are normalized. Figure 68 shows the normalized current density variation with pressure.

The calculated normalized current densities are almost constant and close to the reference value of 400 - 500 µA /cm^2*Torr^2 for a glow discharge with stainless steel electrodes in nitrogen at low pressure normal glow discharge conditions [1]. As per the j/P^2 scaling law [1, 13, 15], the normalized current density thus remains constant with the introduction of the effective pressure.

Figure 69 shows the variation of the electron density with pressure. The measured current densities were also 10 - 20 times greater than atmospheric pressure microplasmas [2, 15]. High electron densities of 2×10^{17} /cm^3 were calculated at the higher pressures making the high pressure microplasma suitable for plasma processing applications.

With the discharge sizes decreasing with the increase in pressure, the scaling is not 'Pd' but rather can be considered to be 'nd' due to the increase in gas temperature and hence dependent on collision processes or the mean free path. The plasma parameters hence are actually number density or 'n' dependent rather than pressure dependent.
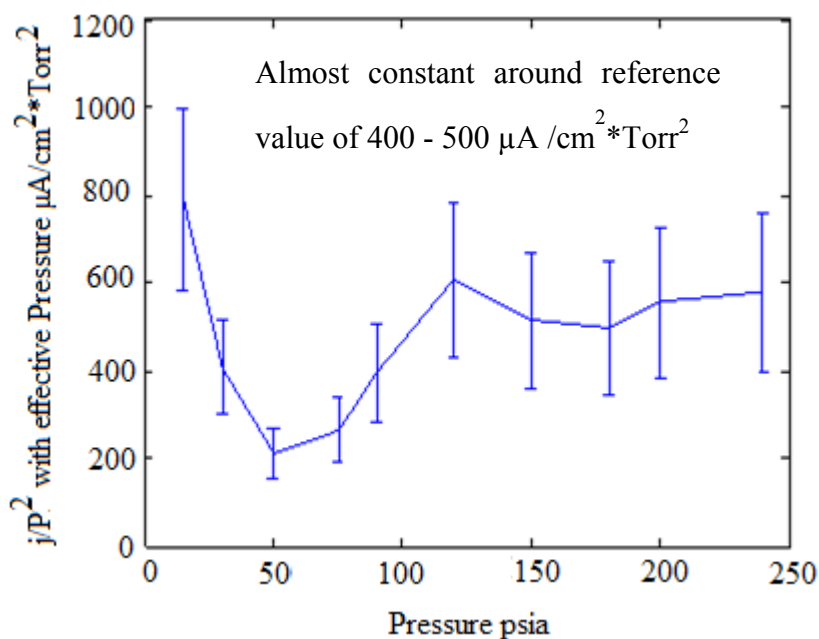
Figure 68. Normalized current density constant around reference value
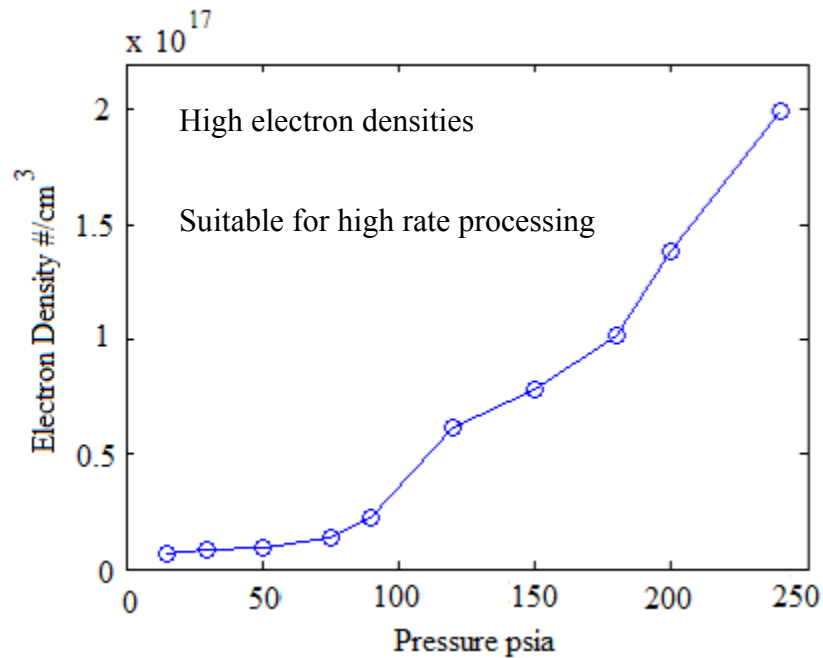
Figure 69. High electron densities at higher pressure in nitrogen

6.2.4. Microplasma: A scaled version of the normal glow discharge

We found that the microplasma discharge size decreases with increase in pressure. The normalized current density also remains fairly constant at the expected reference value for low pressure normal glow discharge plasmas.

Scaling is observed in both discharge size and current density measurements. This thesis work provides further evidence of microplasmas being scaled version of normal glow discharges [2]. The scaling however is 'nd' rather than 'Pd' with the measured increase in gas temperature with increase in pressure. The 'nd' scaling represents the dependence of the plasma parameters on collisional processes and hence the mean free path or the number density rather than pressure.

Table 7 lists the parameters of the smallest measured microplasma discharge.

Table 7. Microplasma parameters at 240 psi with smallest discharge size.

Plasma parameters	Discharge current 0.5mA 240 psia pressure in nitrogen
Electrode spacing	50 μm
Power supply voltage	1374 V
Ballast resistor	2 MΩ
Resistor in chamber	100 KΩ
Discharge voltage	324 V
Discharge power	0.162 W
Negative glow diameter	7 μm
Rotational temperature	2894 K
Vibrational temperature	3068 K
Normalized current density	580 μA /cm^2*Torr^2
Electron density	2 x 10^{17}/cm^3
Power density	7.9 x 10^7 W/cm^3
Surface power density	3.95 x 10^5 W/cm^2

6.3. Recommendations and future work

6.3.1. Direct write surface patterning application

The microplasma discharge can be used in potential direct write surface patterning applications. These applications could range from direct write printers to direct patterning of micron sized features in a wide variety of materials. The high energy density of the microplasma in its cathode glow should enable machining in even hard to machine materials. Arrays of the micron sized features lower than 10 μm in size could be patterned or could be machined as per pre-loaded co-ordinates. This direct write technology capable of generating feature sizes a few μm in size or even submicron in size could find application in the semiconductor manufacturing industry with regards to patterning in silicon. Direct write surface patterning applications using hundreds of microplasmas powered in a parallel configuration can be envisioned. Figure 70 outlines the direct write patterning concept.

The low power consumption advantage offered by the microplasmas could well make this technology extremely beneficial towards reducing manufacturing costs. The microplasma also eliminates the need for complex vacuum systems which are extremely expensive to manufacture and maintain. The microplasma configuration again is extremely simple. This would further reduce manufacturing and maintenance costs for the system. Though a high pressure environment would be required, high pressure costs are significantly lower than vacuum systems.
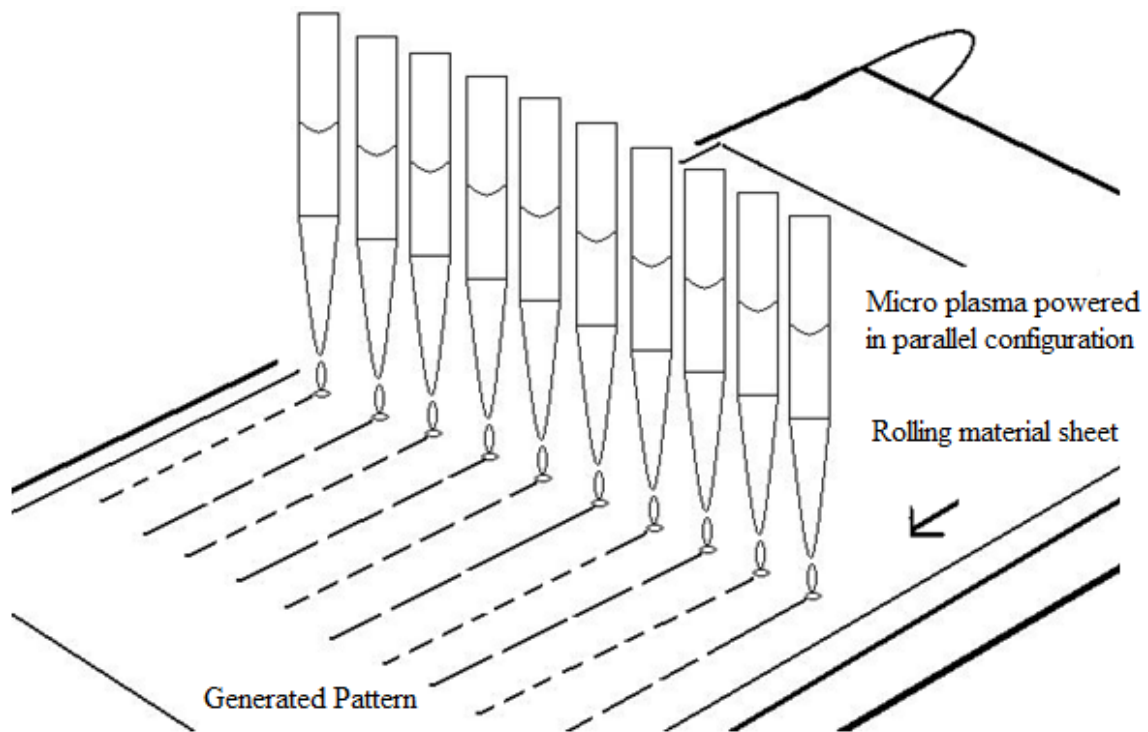
Figure 70. Direct write surface patterning with parallel microplasmas

6.3.2. Future work

Future work in microplasmas with regards to the topics studied in this thesis could be concentrated on two major aspects. The first would be the design of a computer controlled system to generate patterns of 10 μm sized features. A direct write patterning system of this nature could find immediate application in the electronics industry or for manufacturing purposes. Secondly, further research should be pursued to push on towards the submicron regime. Microplasmas venturing towards the nano scale regime could find several applications in medical science as we approach cellular dimensions.

REFERENCES

[1]   Fridman A and Kennedy L 2004 *Plasma Physics & Engineering* (New York: CRC Press)

[2]   Staack D, Farouk B, Gutsol A and Fridman A 2008 DC normal glow discharges in atmospheric pressure atomic and molecular gases *Plasma Sources Science & Technology* **17** 025013 1-13

[3]   Becker K H, Schoenbach K H and Eden J G 2006 Microplasmas and applications *J. Phys. D: Appl. Phys.* **39** R55-R70

[4]   Kogelschatz U 2004 Atmospheric-pressure plasma technology *Plasma Phys. Control. Fusion* **46** B63-B75

[5]   Tanaka Y and Iizuka S 2004 Characteristics of a micro-plasma produced by atmospheric pressure RF impulse discharge using coaxial micro-electrode *Thin Solid Films* **506–507** 436– 439

[6]   Ringeisen B R, Chrisey D B, Piqué A, Krizman D, Brooks M and Spargo B 2001 Direct write technology as a tool to rapidly prototype patterns of biological and electronic systems *Nanotechnology* **1** 414-417

[7]   Sampath S 2005 Novel concepts in direct writing of electronic and sensors *Society of Imaging and Printing* 21-25

[8]   Chrisey D B 2000 The Power of direct writing *Science* **289** 879-881

[9]   Zachariasse J M Frank and Walker J 1997 Direct write patterning of titanium films using focused ion beam implantation and plasma etching *Microelectronics Engineering* **35** 63-66

[10]   Young D, Sampath S, Chichkov B, and Chrisey D B 2005 The future of direct writing in electronics *Circuit Tree* **2** 50-53

[11]   Yokoyama T, Kogoma M, Moriwaki T and Ozaki S 1990 The mechanism of the stabilization of glow plasma at atmospheric pressure *J. Phys. D: Appl. Phys.* **23** 1125-27

[12]   Stark R H and Schoenbach K H 1999 Direct current high pressure glow discharges *J. Appl. Phys.* **85** 2075-2080

[13]   Kushner M J 2005 Modeling of micro discharge devices: Plasma and gas dynamics J. *Phys. D: Appl. Phys.* **38** 1633–1643

[14]   Plasma-Universe.com http://www.plasma-universe.com/Electric_glow_discharge Date last accessed: 09/12/2010

[15]   Staack D, Farouk B, Gutsol A and Fridman A 2005 Characterization of a dc atmospheric pressure normal glow discharge *Plasma Sources Science & Technology* **14** 700-711

[16]   Foest R, Schmidt M and Becker K 2006 Microplasmas, an emerging field of low-temperature plasma science and technology *International Journal of Mass Spectrometry* **248** 87-102

[17]   Schlemm H and Roth D 2001 Atmospheric pressure plasma processing with microstructure electrodes and micro planar reactors *Surface and Coatings Technology* **142** 272-276

[18]   Fujiyama H, Tokitu Y, Uchikawa Y, Kuwahara K and Miyake K 1999 Titanium coating of the inner of a 1 m long narrow tube by double-ended anode coaxial magnetron-pulsed plasma *Surface and Coatings Technology* **112** 185-188

[19]   Kang J G, Kim H S, Ahn S W and Uhm H S 2003 Development of the RF plasma source at atmospheric pressure *Surface and Coatings Technology* **171** 144-148

[20]   Kim Y H, Choi Y H, Park J K, Ju W T, Peak K H and Hwang Y S 2003 Characterizations of atmospheric pressure ejected plasma sources *Surface and Coatings Technology* **174** 535-540

[21]   Sankaran R M and Giapis K P 2002 Hollow cathode sustained plasma micro jets: Characterization and application to diamond deposition *J. Appl. Phys.* **92** 2406-2411

[22]   Sankaran R M and Giapis K P 2003 High-pressure micro discharges in etching and deposition applications *J. Phys. D: Appl. Phys.* **36** 2914-2921

[23]   Sankaran R M and Giapis K P 2001 Maskless etching of silicon using patterned micro discharges *Appl. Phys. Lett.* **79** 593-595

[24]   Penache C 2002 Study of high pressure glow discharges based on MSE arrays *Ph.D. dissertation Johann Wolfgang Goethe University (Frankfurt, Germany)*

[25] Guo Y B and Hong F C N 2003 Radio frequency micro discharge arrays for large area cold atmospheric plasma generation *Appl. Phys. Lett.* 82 337-339

[26] Baars-Hibbe L, Lucas N, Sichler P, Schrader C, Schenk A, , B¨uttgenbach S, and Gericke K H 2005 High frequency glow discharges at atmospheric pressure with micro-structured electrode arrays *J. Appl. Phys.* **38** 510-517

[27] Manz A, Graber N and Widmer H M 1990 Miniaturized total chemical analysis systems: A novel concept for chemical sensing *Sens. Actuators* **B1** 244-248

[28] Eijkel J C T, Stoeri H and Manz A 2000 An atmospheric pressure dc glow discharge on a microchip and its application as a molecular emission detector *J. Anal. At. Spectrom.* **15** 297-300

[29] Manz A and Eijkel J C T 2001 Miniaturization and chip technology *Pure Appl. Chem.* **73** 1555-1561

[30] Evju J K, Howell P B, Locascio L E, Tarlov M J and Hickham J J 2004 Atmospheric pressure microplasmas for modifying sealed micro fluidic devices *Appl. Phys. Lett.* **84** 1668-1670

[31] Sankaran R M 2004 High-pressure micro discharges as micro reactors for materials applications *Ph.D. dissertation California Institute of Technology (Pasadena, CA)*

[32] Baars-Hibbe L, Schrader C, Sichler P, Cordes T, Gericke K H, B¨uttgenbach S and Draeger S 2004 Sharp bursts of high-flux reactive species in sub microsecond atmospheric pressure glow discharges *Vacuum* **73** 327-332

[33] Becker K, Koutsospyros A, Yin S M, Christodoulatos C, Abramzon N, Joaquin J C and Brelles-Marino G 2005 Plasma chemical degradation of VOCs in a capillary discharge plasma reactor plasma *Phys. Control. Fusion* **47** B513-B523

[34] Sichler P, B̈uttgenbach S, Baars-Hibbe L, Schrader C and Gericke K H 2004 Micro-structured electrode arrays: high-frequency discharges at atmospheric pressure characterization and new applications *Chem. Eng. J.* **101** 465-468

[35] Eden J G, S-J Park and Kim K-S 2006 Arrays of non-equilibrium plasmas confined to micro cavities: an emerging frontier in plasma science and its applications *Plasma Sources Sci. Technol.* **15** S67–S73

[36] Eden J G and Park S-J 2005 Micro cavity plasma devices and arrays: a new realm of plasma physics and photonic applications *Plasma Phys. Control. Fusion* **47** B83–B92

[37] Park S-J, Eden J G, Chen J and Liu C 2004 Micro discharge devices with 10 or 30 μm square silicon cathode cavities: 'Pd' scaling and production of the XeO excimers *Appl. Phys. Lett.* **85** 4869–4871

[38] Schoenbach K H, Moselhy M, Shi W, and Bentley R 2003 Micro hollow cathode discharges *J. Vac. Sci. Technol.* **21** 1260-1265

[39] Stark R H and Schoenbach K H 1999 Direct current glow discharges in atmospheric air *Appl. Phys. Lett.* **74** 3770-3772

[40] Schoenbach K H, El-Habachi A, Moselhy M, Shi W, and Stark R H 2000 Micro hollow cathode discharge excimer lamps *Phys. Plasmas* **7** 2186-2191

[41] Tan H, Ideno T and Ichiki T 2005 3 Dimensional silicon micro machining using a scanning microplasma jet source *Journal of Photopolymer Science and Technology* **18** 237-242

[42] Professionalmicroscopes.com http://www.professionalmicroscopes.com/microsc ope_digital_camera_318CU-micrometrics.html Date last accessed: 09/12/2010

[43] Professionalmicroscopes.com http://www.professionalmicroscopes.com/Unitron-MEC2_inverted_microscope.html Date last accessed: 09/12/2010

[44] National Institutes of Health http://rsbweb.nih.gov/ij/index.html Date last accessed: 09/12/2010

[45] Hollas J M 2004 *Modern Spectroscopy* 4th edition (Chichester, UK: John Wiley and Sons Ltd.)

[46] Committee on Computers in Chemical Education Volland W http://www.800ma instreet.com/spect/emission-flame-exp.html Date last accessed: 09/12/2010

[47] Horiba Jobin Yvon Inc. http://www.horiba.com/us/en/scientific/products/optical spectroscopy/spectrometers-monochromators/1000m/1000m-series-ii-high-resolution-research-spectrometer-188//?Ovly=1 Date last accessed: 09/12/2010

[48] Hamamatsu Corporation http://sales.hamamatsu.com/en/products/electrontubedi vision/detectors/photomultiplier-modules.php Date last accessed: 09/12/2010

[49] Stanford Computer Optics, Inc. http://www.stanfordcomputeroptics.com/p-picosecond-iccd.html Date last accessed: 09/12/2010

[50] National Institute of Standards and Technology http://physics.nist.gov/PhysRef Data/ASD/lines_form.html Date last accessed: 09/12/2010

[51]   US   Digital   http://usdigital.com/products/E5/?source=motionnet   Date   last accessed: 09/12/2010

[52]   National Instruments Inc. http://www.ni.com/pciexpress/ Date last accessed: 09/12/2010

[53]   Flyckt S O and Marmonier C 2002 *Photomultiplier Tubes: Principles and Applications* (Brive, France: Philips Photonics)

[54]   Laux C O 2002 Radiation and non equilibrium collision radiative models *VKI Special Course on Physico-Chemical Models for High Enthalpy and Plasma Flows Modeling (Palo Alto, CA, Stanford University)*

[55]   G Herzberg 1950 *Spectra of Diatomic Molecules* (New York: Van Nostrand-Reinhold)

[56]   Staack D, Farouk B, Gutsol A and Fridman A 2006 Spectroscopic studies and rotational and vibrational temperature measurements of atmospheric pressure normal glow plasma discharges in air *Plasma Sources Science & Technology* **15** 818-827

[57]   Kovacs I 1969 *Rotational Structure in the Spectra of Diatomic Molecules* (New York: American Elsevier Publishing Company, Inc.)

[58]   Whiting E E and Nicholls R W 1974 Reinvestigation of rotational line intensity factors in diatomic spectra *Astrophysical Journal Supplement* **27** 1-19

[59]   Gilmore F R, Laher R R and Epsy P J 1992 Franck-Condon factors, r-centroids, electronic transition moments and Einstein coefficients for many nitrogen and oxygen band systems Journal of *Physics* Chemical *Reference data* **21** 1005-1007

[60]   National Optical Astronomy Laboratory Arizona Sharp http://www.noao.edu /image_gallery/text/fwhm.html Date last accessed: 09/12/2010

[61]   Staack D, Farouk B, Gutsol A and Fridman A 2007 Spatially resolved temperature measurements of atmospheric-pressure normal glow microplasmas in air *IEEE Transactions on Plasma Science* **35** 1448-1455

[62]   Nelder J A and Mead R 1965 A simplex method for function minimization *Computer Journal* **7** 308–313

[63]   St. Pat's Inc. http://www.stpats.com/index.htm; Date last accessed: 09/12/2010

[64]   Alicat Scientific Inc. http://www.alicatscientific.com Date last accessed: 09/12/2010

[65]   Honeywell Inc. http://www.mouser.com/Search/ProductDetail.aspx?R=MLH500 PSB01Avirtualkey67810000virtualkey785-MLH500PSB01A Date last accessed: 09/12/2010

[66]   Glassman High Voltage Inc. http://www.glassmanhv.com/ByWattage/eh_series. shtml Date last accessed: 09/12/2010

[67]   LeCroy Inc. http://www.tequipment.net/LeCroy.html Date last accessed: 09/12/2010

[68]   Lifshitz A 1974 Correlation of vibrational de-excitation rate constants (k0 < 1) of diatomic molecules *J. Chem. Phys.* **61**, 2478-2479

APPENDIX A

ANALYZE IMAGE SIZE CODE

```
clear
clc
close all

f = dir('*.bmp');
fn = {f.name};

for ii = 1:length(fn)
file = fn{ii};
    A = imread(file);
ROIx = [600:1100];
ROIy = [600:1100];

As = A(ROIy,ROIx,:);
Gs_As = sum(As,3);
nearsat = find(Gs_As>=254*3);
length(nearsat)
Gs_Asn = Gs_As./max(max(Gs_As));
Threshold = 0.7;
ss = size(Gs_Asn);

forjj = 1:ss(1)
HInt = Gs_Asn(jj,:);
IndsAbove = find(HInt>Threshold);
if ~isempty(IndsAbove)
LfI(jj) = min(IndsAbove);
RtI(jj) = max(IndsAbove);
else
LfI(jj) = NaN;
RtI(jj) = NaN;
end
Wd(jj) = (RtI(jj)-LfI(jj));
end

subplot(1,2,1)
imagesc(Gs_Asn)
figure
hold on
jjinds = [1:ss(1)];
plot(LfI,jjinds)
```

```
plot(RtI,jjinds)
 a = get(gca,'position');
a(4) = .7;
set(gca,'position',a)
subplot(1,2,2)
plot(Wd,jjinds)
set(gca,'ydir','reverse')
ylim([0,ss(1)-1])
Conversion = (1/16)*25400/1138;
DischargeWidth(ii) = max(Wd)*Conversion;
CurrDen(ii) = 1e-3/(pi/4*DischargeWidth(ii)^2)*1e8; %%
A/cm2
Pressure(ii) = str2num(file(1:findstr('Psi',file)-1));
Voltage(ii) =
str2num(file([findstr('mA..',file)+4:findstr('KV',file)-
1])); %kV
Current(ii) = 1; %mA
title([file,'  ',num2str(DischargeWidth(ii))])
a = get(gca,'position')
a(4) = .7;
set(gca,'position',a)
pause(.1)
end

figure
plot(Pressure,DischargeWidth,'x-')
xlabel('Pressure (psi)')
ylabel('Discharge Width (um)')
figure
plot(DischargeWidth,'x-')
xlabel('file')
ylabel('Width unm)')

Current1=3000;
for i=1:10
Pressure1(i)= (Pressure(i)*760)/15;
M(i)=(Current1*10^8/[DischargeWidth(i)^2*Pressure1(i)^2]);
end

plot(Pressure,M,'o-r');
set(gca,'fontsize',14)
xlabel('Pressure psi');
ylabel('Curren Density μA/cm2*Torr2');
```

APPENDIX B

TEMPERATURE ESTIMATION MODEL CODE

```
close all
clc
clear all

h=6.626068*10^-34;
c=2.98*10^10;
kb=1.380650*10^-23;

%Set temperatures%
Tvib=4000;
Trot=700;
Telec=10000;

%Set wavelength range along with resolution and FWHM%
wlim=355;
wlim2=382;

FWHM = 0.1;

res=0.01;

%/Extra parameters-- Dont change/%
rf=1/res;
span=(wlim2-wlim)/res;

%Set No of rotational levels/%
jmax = 50;

%/State C parameters/%
we_c=2035.1;
wexe_c=17.08;
weye_c=-2.15;
T_c=89147;
Be_c=1.8259;
ae_c=0.0197;

%Upper state vibration level/%
v_c=[0,1,2,3];
FCF=[0.3804,0.3754,0.3709,0.3671];
K=1;
```

```
%Upper state energy calculations/%

x1_c=length(v_c);

for g=1:1:x1_c

va= v_c(g)+.5;
G_c(g)=(we_c*va)-(wexe_c*va^2)+(weye_c*va^3);
Bv_c(g)=Be_c-(ae_c*va);
Dv_c(g)=(4*(Bv_c(g)^3))/(G_c(g)^2);


for j=1:1:jmax
F_c(j,g)=Bv_c(g)*j*(j+1)-Dv_c(g)*j^2*((j+1)^2);
C(j,g)=T_c+G_c(g)+F_c(j,g);
total(j,g)=-
h*c*((T_c/(kb*Telec))+(G_c(g)/(kb*Tvib))+(F_c(j,g)/(kb*Trot
)));
Nu1(j,g)=((2*j)+1)*exp(total(j,g));
Nu((3*j)-2,g)=Nu1(j,g);
Nu((3*j)-1,g)=Nu1(j,g);
Nu(3*j,g)=Nu1(j,g);
end

end


%Lower state vibration level/%
v_b=[2,3,4,5];


%/State B parameters/%
we_b=1734.11;
wexe_b=14.47;
T_b=59626;
Be_b=1.638;
ae_b=0.0184;

%Lower state energy calculations/%

for g=1:1:x1_c

va= v_b(g) +.5;
```

```
G_b(g)=(we_b*va)-(wexe_b*va^2);
Bv_b(g)=Be_b-(ae_b*va);
Dv_b(g)=(4*Bv_b(g)^3)/(G_b(g)^2);


for j=1:1:jmax

j_p=j-1;
j_r=j+1;

F_b(j,1,g)=Bv_b(g)*j_p*(j_p+1)-Dv_b(g)*j_p^2*((j_p+1)^2);
F_b(j,2,g)=Bv_b(g)*j*(j+1)-Dv_b(g)*j^2*((j+1)^2);
F_b(j,3,g)=Bv_b(g)*j_r*(j_r+1)-Dv_b(g)*j_r^2*((j_r+1)^2);
B(j,1,g)=T_b+G_b(g)+F_b(j,1,g);
B(j,2,g)=T_b+G_b(g)+F_b(j,2,g);
B(j,3,g)=T_b+G_b(g)+F_b(j,3,g);

end
end


%/Locations of the peaks divided into P,Q,R branches/%

for g=1:1:x1_c
m=1;
for a=1:1:jmax
for b=1:1:3

E2(a,b,g)=10E6/(C(a,g)-B(a,b,g));
 l(m,g)=round(E2(a,b,g)*rf)/(rf);
l(m,g)=l(m,g)*rf;
        m=m+1;

end
end

end


%/Initlilization/%

m=m-1;
w=1;
```

```
%Wavelength array/%
for s=wlim+res:res:wlim2
Intensity(w)=0;
IntensityFCF(w)=0;
IntensityFCF_check(w)=0;
Intensity_p(w)=0;
IntensityFCF_p(w)=0;
Intensity_q(w)=0;
IntensityFCF_q(w)=0;
Intensity_r(w)=0;
IntensityFCF_r(w)=0;
Wave(w)=s;
w=w+1;
end

for j=1:1:jmax
if(rem(j,2)==1)
LAF((3*j)-2)=1/3;
LAF((3*j)-1)=1/3;
LAF(3*j)=1/3;

else
LAF((3*j)-2)=2/3;
LAF((3*j)-1)=2/3;
LAF(3*j)=2/3;
end
 j_=j+1;
HLF((3*j)-2)=(j_^2-K^2)/j_;
HLF((3*j)-1)=((((2*j)+1)*(K^2))/(j*(j+1)));
HLF(3*j)=(j^2-K^2)/j;
end

%/Assigning intensity to wavelength and multiplying by
intensity factor/%
checkctr=0;
for g=1:1:x1_c
x=1;
for x=1:1:m
w=1;
for s=((wlim+res)*rf):(res*rf):(wlim2*rf);
if (s==l(x,g))
Intensity(w)=Nu(x,g)+Intensity(w);
```

```
IntensityFCF_check(w)=(Nu(x,g)*FCF(g)*HLF(x)+IntensityFCF_c
heck(w));
IntensityFCF(w)=((Nu(x,g)*FCF(g)*HLF(x)*LAF(x))+IntensityFC
F(w));
checkctr=checkctr+1;
 w=w+1;

else
w=w+1;

end
end

end
end

xp_ctr=0;
for g=1:1:x1_c

forxp=1:3:m-2
w=1;
for s=((wlim+res)*rf):(res*rf):(wlim2*rf);
if (l(xp,g)==s)
Intensity_p(w)=Nu(xp,g)+Intensity_p(w);
IntensityFCF_p(w)=Nu(xp,g)*FCF(g)*HLF(xp)+IntensityFCF_p(w)
;

HLF_p(xp_ctr+1)=HLF(xp);
xp_ctr=xp_ctr+1;

 w=w+1;

else
 w=w+1;

end
end

end
end

xq_ctr=0;
for g=1:1:x1_c
```

```
forxq=2:3:m-1
 w=1;
for s=((wlim+res)*rf):(res*rf):(wlim2*rf);
if (l(xq,g)==s)
Intensity_q(w)=Nu(xq,g)+Intensity_q(w);
IntensityFCF_q(w)=Nu(xq,g)*FCF(g)*HLF(xq)+IntensityFCF_q(w)
;

HLF_q(xq_ctr+1)=HLF(xq);
xq_ctr=xq_ctr+1;

 w=w+1;

else
 w=w+1;

end
end

end
end

xr_ctr=0;
for g=1:1:x1_c

forxr=3:3:m
w=1;
for s=((wlim+res)*rf):(res*rf):(wlim2*rf);
if (l(xr,g)==s)
Intensity_r(w)=Nu(xr,g)+Intensity_r(w);
IntensityFCF_r(w)=Nu(xr,g)*FCF(g)*HLF(xr)+
IntensityFCF_r(w);

HLF_r(xr_ctr+1)=HLF(xr);
xr_ctr=xr_ctr+1;

 w=w+1;

else
w=w+1;

end
end
```

```
end
end

figure
plot(Wave,Intensity)

%/Convolution/%

W1 = linspace(wlim,wlim2,span);
WS = W1-mean(W1);

sigma = FWHM/2.3548
SL = 1./(sigma.*sqrt(2.*pi)).*exp(-WS.^2./(2.*sigma.^2));


I_conv = conv(SL,Intensity);
I_FCF_conv = conv(SL,IntensityFCF);
I_FCF_p_conv = conv(SL,IntensityFCF_p);
I_FCF_q_conv = conv(SL,IntensityFCF_q);
I_FCF_r_conv = conv(SL,IntensityFCF_r);

pt1=span/2;
pt2=(3*pt1)-1;

ct=1;

for x=pt1:1:pt2
I1(ct)=I_conv(x);
I_FCF(ct)=I_FCF_conv(x)/2.8053E-3;
 % I_FCF_max(ct)=I_FCF_conv(x)/max(I_FCF_conv(x));
I_p(ct)=I_FCF_p_conv(x);
I_q(ct)=I_FCF_q_conv(x);
I_r(ct)=I_FCF_r_conv(x);
ct=ct+1;
end

figure
plot(W1,I1)
xlabel('Wavelength');
ylabel('Total spectrum withot adding FCF, HLF');

figure
plot(W1,I_FCF)
```

```
xlim([364 382]);
ylim([0,1.05]);
xlabel('Wavelength');
ylabel('Total spectrum after adding FCF, HLF, LAF');


figure
plot(W1,I_p);
xlabel('Wavelength');
ylabel('P branches contribution');

figure
plot(W1,I_q);
xlabel('Wavelength');
ylabel('Q branches contribution (smaller order)');

figure
plot(W1,I_r);
xlabel('Wavelength');
ylabel('R branches contribution');

figure
plot(W1,I_p,W1,I_q,W1,I_r);
xlabel('Wavelength');
ylabel('Separated contributions');
```

APPENDIX C

DATA USED IN TEMPERATURE MODEL

All parameters are in units of cm^{-1} which is a unit of wave number. Data is obtained from Herzberg [55].

State C parameters:

w_e = 2035.1
$w_e x_e$ = 17.08
$w_e y_e$ = -2.15
T_c = 89147
B_e = 1.8259
a_e = 0.0197

State B parameters:

we = 1734.11
wexe = 14.47
T_b = 59626
be = 1.638
ae = 0.0184

VITA

Name: Aditya Rajeev Chitre

Address: c/o Dr. David Staack

Texas A&M University,
College of Engineering,
3123 TAMU,
Engineering Physics Building, Room 328
College Station, Texas 77843-3137

Email Address: aditya6891@gmail.com

Education: B.Tech. Instrumentation Engineering, University of Pune, 2008

M.S. Mechanical Engineering, Texas A&M University, 2010